A STUDY OF QUANTUM CUTTING BY SENSITIZATION OF Gd^{3+}

by

YI ZHOU

(Under the Direction of Richard S. Meltzer)

ABSTRACT

Large bandgap materials doped with rare earth ions are currently of great interest as new vacuum UV phosphors for lighting and displays. In this dissertation, we examine several ways to sensitize Gd for application to cross relaxation energy transfer (CRET) and photon cascade emission (PCE). The optical properties of GdF_3 doubly doped with Pr and Eu, $GdLiF_4$ doped with Nd, $ScPO_4$ doped with Gd and $GdZrF_7$ doped with Eu are described. The $5d \rightarrow 4f$ transition of a trivalent rare earth ion is an effective method to sensitize Gd^{3+}. It is still necessary to find a system in which the energy gets to the ^6G states of Gd^{3+} such that quantum cutting with a co-doping of Eu^{3+} or some other lanthanide can be utilized for quantum cutting. The sensitization with the STE is a very effective means of obtaining good coupling of the VUV excitation to Gd^{3+}. To use STE sensitization of the ^6G states of Gd^{3+} for quantum cutting, it will be necessary to identify materials whose STE emission occurs at even shorter wavelengths than is the case for $ScPO_4$ so that a larger fraction of the energy transfer occurs to the ^6G states or even higher-lying states of Gd^{3+}.

INDEX WORDS: Quantum cutting, Sensitization, Gd^{3+}, Cross relaxation energy transfer, Photon cascade emission, Self-trapped exciton

A STUDY OF QUANTUM CUTTING BY SENSITIZATION OF Gd^{3+}

by

YI ZHOU

B. Eng., Jinan University, P. R. CHINA 1991

M. S., Anhui Institute of Optics and Fine Mechanics, Chinese Academy Sciences, P. R. CHINA

2001

M. S., The University of Georgia, 2005

A Dissertation Submitted to the Graduate Faculty of The University of Georgia in Partial

Fulfillment of the Requirements for the Degree

DOCTOR OF PHILOSOPHY

ATHENS, GEORGIA

2008

A STUDY OF QUANTUM CUTTING BY SENSITIZATION OF Gd^{3+}

by

YI ZHOU

Major Professor:	Richard S. Meltzer
Committee:	William M. Dennis Yiping Zhao

Electronic Version Approved:

Maureen Grasso
Dean of the Graduate School
The University of Georgia
December 2008

ACKNOWLEDGEMENTS

I would like to thank Prof. Richard S. Meltzer, my major professor for his patience and advice in directing and implementing the research leading to this dissertation. My thanks also to Dr. S.P. Feofilov for his many helpful discussions and his assistance with the experiment.

Finally, a special thanks to my wife and my parents for their support and encouragement without which this thesis may not have been possible.

TABLE OF CONTENTS

Page

CHAPTER 1

INTRODUCTION

In recent years, a growing interest has arisen in the luminescence spectroscopy of rare earths in the vacuum ultraviolet spectral region (VUV; $E \geq 50000$ cm^{-1}, $\lambda \leq 200$ nm). This is due to the need for new VUV phosphors for mercury-free fluorescent tubes and plasma display panels [1]. Currently, the primary excitation of phosphors in fluorescent lamps is achieved by the ultraviolet (UV) excitation from a Hg discharge. While it generates electromagnetic radiation at about 70% efficiency, over 90% of the radiation occurs in the UV region at 254 nm. Conversion of UV light to visible light is accomplished by phosphors that introduce additional losses, predominantly due to the large energy difference between the exciting photon and the emitted photon; the resulting lamp energy efficiencies are at best 33% [2]. To convert the VUV radiation from noble gas discharges into visible light in mercury-free fluorescent tubes and plasma display panels, phosphors with a higher efficiency and stability are required. A serious problem for the replacement of the mercury discharge by a noble gas discharge is the efficiency, i.e. the number of (VUV) photons emitted per watt. The phosphors used in mercury fluorescent tubes have quantum efficiencies close to 100%. Therefore, to make a noble gas discharge fluorescent tube competitive, quantum efficiencies higher than 100% are required, i.e. more than one visible photon should be obtained per absorbed VUV photon [3]. These VUV-excited materials are called “quantum cutting” or “multiphoton” phosphors.

The goal of our study is to find such multiphoton phosphors for VUV excitation. We want to find an effective way to sensitize the ^{6}G states of Gd^{3+} especially in order to apply the cross relaxation energy transfer (CRET) in Gd-Eu system. This study has the potential to generate great benefits to society by providing the scientific basis for realization of a new, highly efficient and environmentally benign lighting technology. Lamps having improved efficiency would decrease the energy consumption for lighting thereby reducing the costs of lighting and the consumption of fossil fuels that contribute to environmental problems. In addition, the replacement of Hg in a standard fluorescent lamp by a rare-gas (VUV) excitation source would eliminate concerns regarding the disposal of Hg-based lamps.

In this dissertation we have studied GdF_3 doubly doped with Pr and Eu, $GdLiF_4$ doped with Nd, $ScPO_4$ doped with Gd and $GdZrF_7$ doped with Eu.

The layout of this dissertation is as follows:

In Chapter 2, we will introduce the theory of quantum cutting and energy transfer. In Chapter 3 we will describe the equipment used for these experiments and the process of measurement. We will analyze the data and discuss the result in Chapter 4 - 7 and will formulate the conclusion in chapter 8.

CHAPER 2

METHODS OF QUANTUM CUTTING

2.1 Introduction

In this chapter, we introduce the concepts of quantum cutting and cross relaxation. We also illustrate photon cascade emission for the Pr^{3+} ion and the cross relaxation energy transfer for a Gd-Eu pair.

2.2 Quantum cutting

In 1957 Dexter mentioned the idea that getting two visible photons out per ultraviolet photon in is generically possible [4]. Therefore from energy conservation principles it is possible to obtain visible quantum efficiencies higher than 100% for VUV phosphors. In other words, after absorbing a VUV photon, the phosphor can produce two visible photons. This phenomenon is called quantum cutting.

The simplest quantum cutting scheme utilizing a two-step photon emission on a single ion is called photon cascade emission (PCE). For example, the phosphor YF_3: Pr^{3+} yields a room temperature quantum yield of 1.40 ± 0.15 under excitation by 185 nm radiation [5]. The process of quantum cutting in Pr^{3+} activated phosphors is shown in Fig. 2.1. Incident VUV photons are absorbed via an allowed Pr^{3+} $4f \rightarrow 5d$ optical transition. The excitation decays nonradiatively to the $^1S_0$ level which decays radiatively to the $^1I_6$ level resulting in the generation of the first photon. A second transition that connects the ^3P levels with several of the ground state levels yields the second photon [2]. Unfortunately, the photons emitted in the first step due to the

$^1S_0 \rightarrow {}^1I_6$ transition have a wavelength of about 407 nm, to which the human eye is insensitive. So this cascade quantum cutting phosphor is not suitable for lighting applications.

Photon cascade emission has also been demonstrated for the Gd^{3+} ion in $GdLiF_4$ and $ScPO_4$. The process is shown in Fig. 2.2. In this case, Gd^{3+} radiates in a sequential two-step process; the first transition is $^6G \rightarrow {}^6P$ in the red followed by a $^6P \rightarrow {}^8S$ transition in the UV. A second ion can be introduced so that an energy transfer occurs from the ^6P level of Gd^{3+} to this second ion which can emit a visible photon. Thus Gd^{3+} offers a number of opportunities for the development of quantum cutting phosphors. However, the practical use of PCE for Gd^{3+} has been limited by the inability to efficiently excite the ^6G states of Gd^{3+} since transitions to this state from its ground state are parity forbidden ($4f^7 \rightarrow 4f^7$) and the $4f^65d$ state lies at too high an energy to be accessible with a Xenon discharge.

Another scheme to develop an efficient quantum cutting phosphor is to utilize a pair of ions which can share the energy of the initial excitation. The cross relaxation process is one in which the energy of excitation, initially localized on one ion, is partially transferred to a neighboring ion, leaving both ions in excited energy levels that radiate to their respective ground or lower-lying states [6]. In Fig. 2.3 the possibility of quantum cutting by cross relaxation energy transfer is shown. The initially excited ion D undergoes a non-radiative transition of ($3 \rightarrow 2$) to an intermediate excited state (2) while simultaneously the ion A undergoes an upward transition from its ground state (1) to an excited state (2), conserving energy and leaving both ions in excited states from which each can emit a visible photon.

2.3 Förster-Dexter energy transfer theory

The microscopic energy transfer from the sensitizer to the activator in inorganic materials was first considered theoretically by Förster [7] and Dexter [8]. A direct-energy-transfer theory was worked out by Förster for singlet-singlet transfer and by Dexter for triplet-triplet transfer more than 50 years ago. It predicts the following:

(a) The excitation in Fig. 2.3 of a sensitizer or donor ion (*D*) is transferred to an activator or acceptor ion (*A*), which is separated by a distance *R*, by a nonradiative process which is analogous to a simultaneous emission process on *D* and an absorption process on *A*. The interactions which cause energy transfer are electrostatic coupling, magnetic coupling, and/or exchange coupling between ions.

(b) The rate of dipole-induced transfer decreases as R^{-6} whereas the rate of exchange-induced transfer decreases as exp(-*2R/L*), where *R* is the donor-acceptor separation and *L* is an effective average Bohr radius for the excited and unexcited states of the ions *D* and *A*.

(c) The energy transfer rate is proportional to the spectral overlap of the corresponding emission and absorption bandwidths of the *D* and *A* ions, respectively so as to preserve conservation of energy [9].

Initially these two ions are in the state $\left|D_3, A_1\right\rangle$. An interaction H_1 between ions *A* and *D* causes a transition from $\left|D_3, A_1\right\rangle$ to $\left|D_2, A_2\right\rangle$. The transition probability is

$$P_{DA} = \frac{2\pi}{\hbar}\left|\left\langle D_2, A_2\right| H_1 \left| D_3, A_1\right\rangle\right|^2 S \tag{2.1}$$

and the overlap integral *S* reflects the requirement of energy conservation. *S* is defined by

$$S = \int g_D(E) g_A(E) dE \tag{2.2}$$

where *g(E) is* the normalized spectral function for the individual transitions $D_3 \rightarrow D_1$ and $A_1 \rightarrow A_2$.

Since the 4*f* wave functions of these ions are very close to those of the free ions even in crystalline environments, it is convenient to introduce the following operator:

$$D_q^{(k)} = \sum_i r_i^k C_q^{(k)}(\theta_i, \phi_i) \tag{2.3}$$

with

$$C_q^{(k)}(\theta_i,\phi_i)=\sqrt{\frac{4\pi}{2k+1}}Y_q^{(k)}(\theta_i,\phi_i) \tag{2.4}$$

where $Y_q^{(k)}$ is a spherical harmonic and (r_i,θ_i,ϕ_i) the polar coordinates of the *i*-th electron of the ion. The electrostatic interaction between the electrons on ion *D* and on ion *A* can be written as [10]

$$H_1=\frac{1}{4\pi\varepsilon_0\kappa}\sum_{i,j}\frac{e^2}{\left|\vec{r}_i-\vec{r}_j\right|}=\frac{1}{4\pi\varepsilon_0\kappa}\sum_{\substack{kk_2\\q_1q_{21}}}\left(e^2/\vec{R}^{1+k_1+k_2}\right)C_{q_1q}^{k_1k_2}D_{q_1}^{(k_1)}\left(\vec{r}_D\right)D_{q_2}^{(k_2)}\left(\vec{r}_A\right) \tag{2.5}$$

where *R* is the separation between the two ions, the ions *D* and *A*, and $C_{q_1q}^{k_1k_2}$ is a numerical factor that depends on the orientation of the coordinate axes. *κ* is the dielectric constant. When the ions *D* and *A* are located respectively at the origin and (r_i,θ_i,ϕ_i) of the polar coordinates, this factor is given by

$$C_{q_1q_2}^{k_1k_2}(\theta,\phi)=(-1)^{k_1}\left[\frac{(2k_1+2k_2+1)}{(2k_1)!(2k_2)!}\right]^{1/2}\times\begin{pmatrix}k_1 & k_2 & k_1+k_2\\ q_1 & q_2 & -(q_1+q_2)\end{pmatrix}\left[C_{q_1+q_2}^{(k_1+k_2)}(\theta,\phi)\right]^* \tag{2.6}$$

where $\begin{pmatrix}j_1 & j_2 & j_3\\ m_1 & m_2 & m_3\end{pmatrix}$ is the 3-*j* symbol.

As an approximation, we replace the square of the matrix element by its average [11]

$$\left|\langle D_2,A_2|H_1|D_3,A_1\rangle\right|^2=\left(\frac{1}{4\pi\varepsilon_0\kappa}\right)^2\sum_{k_1,k_2}\left(\frac{e^2}{R^{1+k_1+k_2}}\right)^2\times\frac{(2k_1+2k_2)!}{(2k_1+1)!(2k_2+1)!}\left|D_D^{(k_1)}\right|^2\left|D_A^{(k_2)}\right|^2 \tag{2.7}$$

where

$$\left|D_D^{(k_1)}\right|^2=\sum_{q_1}\left|\langle D_2|\mu_{q_1}^{(k_1)}(r_D)|D_3\rangle\right|^2 \tag{2.8}$$

with a similar formula for $\left|D_A^{(k_2)}\right|^2$.

For the dipole-dipole interaction, the transition probability of energy transfer is obtained from the k_1=1, k_2=1 term in Eq. (2.7). We find

$$P_{DA}^{dd} = \frac{4\pi}{3\hbar}\left(\frac{1}{4\pi\varepsilon_0\kappa}\right)^2 \frac{e^4}{R^6}\left|\left\langle D_D^{(1)}\right\rangle\right|^2\left|\left\langle D_A^{(1)}\right\rangle\right|^2 S \tag{2.9}$$

The factor $\left|\left\langle D^{(1)}\right\rangle\right|^2$ is proportional to the oscillator strength $f(ED)$ of the optical transition connecting the initial and final states of the cross relaxation,

$$f(ED) = \frac{2m\omega}{3\hbar}\left|\left\langle D_D^{(1)}\right\rangle\right|^2 \tag{2.10}$$

where ω is the average central frequency of the transition. So we obtain

$$P_{DA}^{dd} = \left(\frac{1}{4\pi\varepsilon_0}\right)^2 \frac{3\pi\hbar e^4}{n^4 m^2\omega^2}\frac{1}{R^6} f_D(ED) f_A(ED) S \tag{2.11}$$

using $\kappa = n^2$, where n is the refractive index. Putting in values for the constants and expressing the transition energy, $\Delta E = \hbar\omega$, in eV, the overlap integral in cm^{-1}, and the ion-ion distance in Angstroms, the transition rate can be calculated as

$$P_{DA}^{dd} = \left(1.4\times10^{24} f_D f_A S\right)/\left(\Delta E^2 R^6\right) \tag{2.12}$$

For the case of a 5d → 4f parity-allowed transition on the donor ion and a 4f → 4f parity-forbidden transition as the acceptor, we assume oscillator strengths of 10^{-2} and 10^{-6} for the 5d → 4f and 4f → 4f transitions, respectively, ΔE = 3 eV, and $S = 10^{-3}$, reflecting the fact that the 5d → 4f downward transition is broad (about 1000 cm^{-1}), then we find for nearest neighbors at a distance of 3.5 Å, a rate of ~10^9 s^{-1} which is ten times greater than the 5d radiative rate of ~10^8 s^{-1}. At more typical phosphor dopant concentrations of 2-5%, the energy transfer rate would be expected to be 10^7-10^8 s^{-1}, still competitive with the radiative rate. Exchange mediated energy transfer can be even much faster, but it will only be important for nearest neighbor distances.

Recently, an effort in quantum cutting phosphors centered on the couple Gd^{3+}-Eu^{3+} has been described in the literature involving 4f-4f transition on both the donor and acceptor. Two-step energy transfer from the ^6G_J level of Gd^{3+} to Eu^{3+} is possible, as is shown in Fig. 2.4. Incident VUV photons are absorbed via the Gd^{3+} $^8S_{7/2} \rightarrow {}^6G_J$ optical transition. The first step (labeled as A in the figure) is a cross relaxation energy transfer between Gd^{3+} in the ^6G_J state and Eu^{3+} in the ^7F_J ground state, resulting in Eu^{3+} in the $^5D_0$ excited state and Gd^{3+} in the ^6P_J state. This occurs with high probability because Gd^{3+} is present at 100% concentration so that exchange dominates and there is a good spectral overlap between the $^6G_J \rightarrow {}^6P_J$ transitions on Gd^{3+} and the $^7F_J \rightarrow {}^5D_0$ transitions on Eu^{3+} [12]. The second step is that the Gd^{3+} ion in the ^6P_J state transfers the remaining excitation energy to a second Eu^{3+} ion, which is followed by efficient radiative decay to the ^7F_J states. Hence two visible red photons may be produced per incident VUV photon.

In this dissertation we examine several ways to sensitize Gd for application to cross relaxation energy transfer (CRET) and photon cascade emission (PCE).

In chapter 4, we study GdF_3 doubly doped with Pr and Eu. In this case, Pr is the donor and Gd is the acceptor. For the application of CRET, we used the 5d→4f transition of Pr to sensitize the Gd-Eu system. In chapter 5, we studied the $GdLiF_4$ doped with Nd. For this sample, Nd is the donor and Gd is the acceptor. For the application of CRET, we used the 5d→4f transition of Nd to sensitize Gd.

In chapter 6, we studied the $ScPO_4$ doped with Gd. In this case we used the self-trapped exciton (STE) of host as donor to sensitize Gd for the application of PCE. We also studied the $GdZrF_7$: Eu in chapter 7. While this is not a quantum cutting phosphor it is a nearly white phosphor with a quantum yield near unity. .

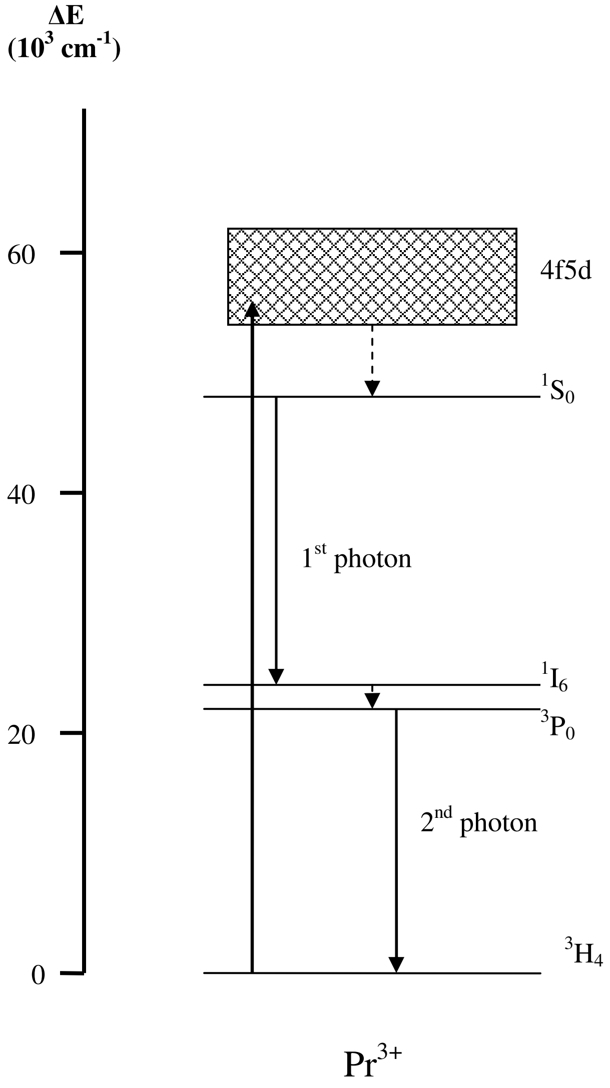

Fig. 2.1 Schematic representation of multiphoton emission via Pr^{3+} ion

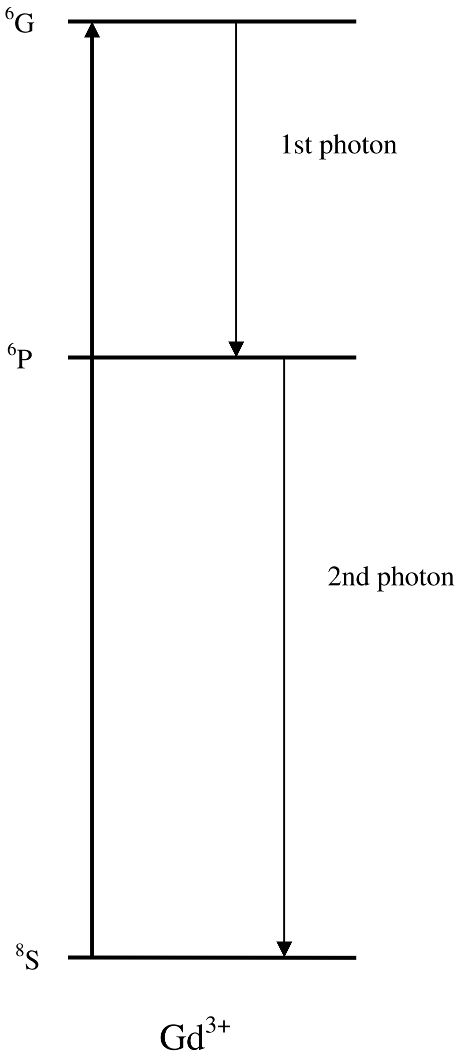

Fig. 2.2 Energy level diagram for PCE of Gd^{3+}

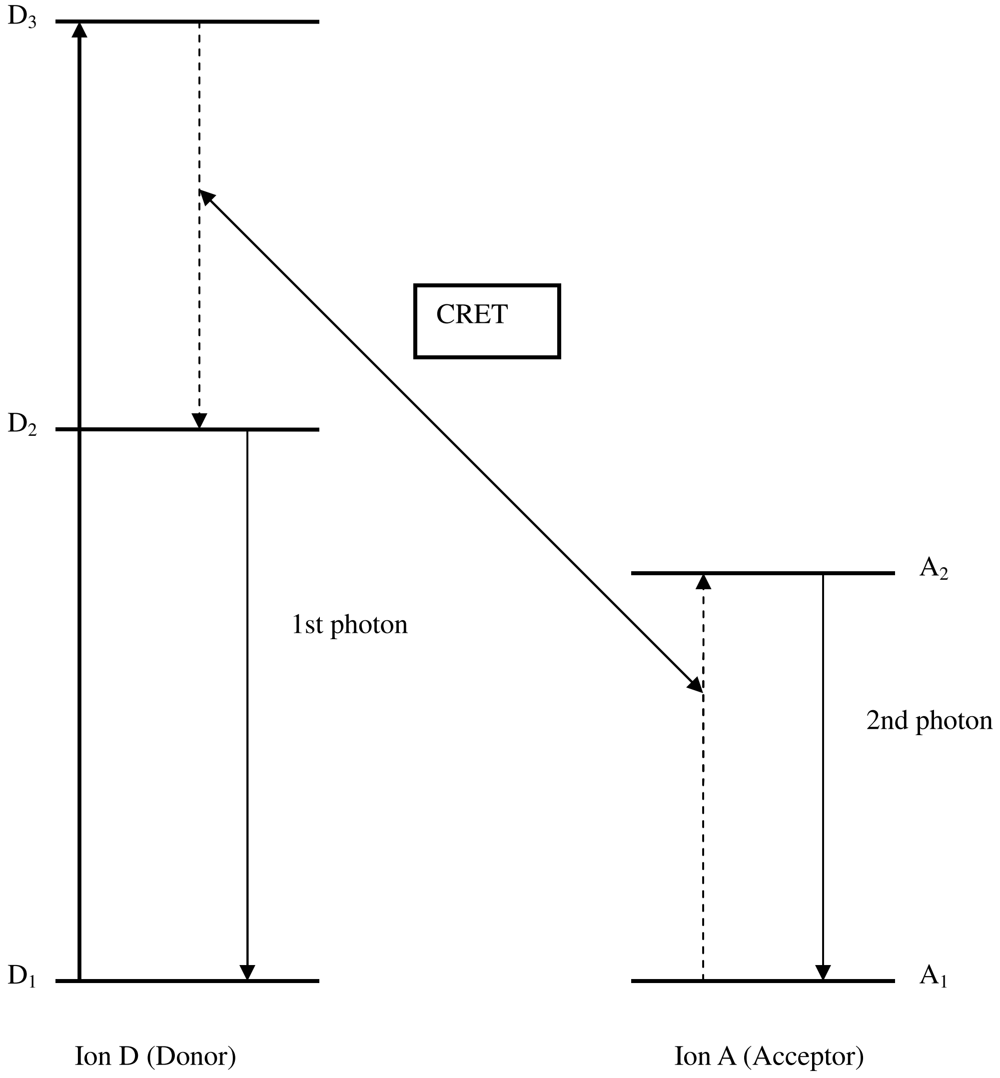

Fig. 2.3 Description of cross relaxation energy transfer (CRET)

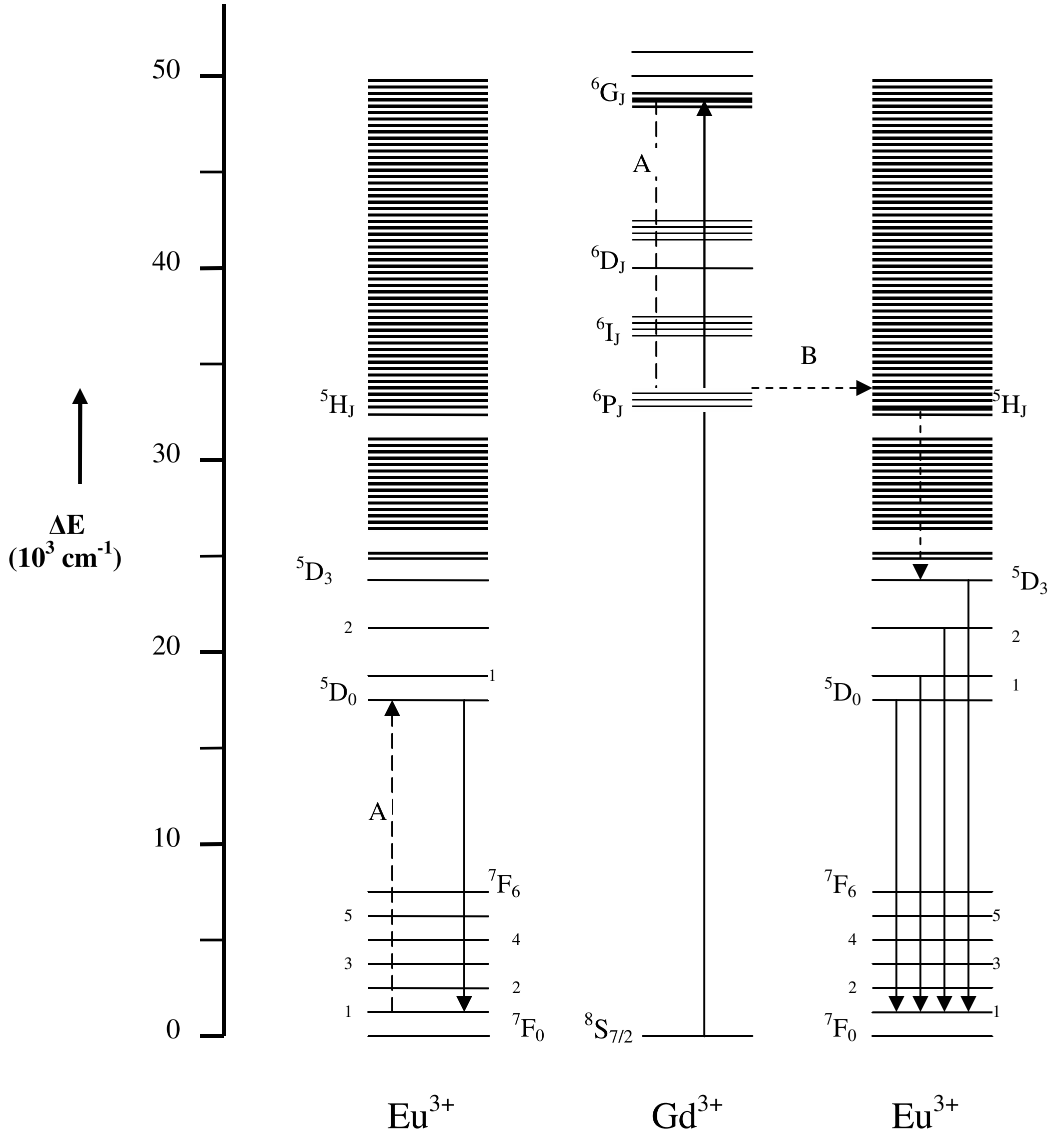

Fig. 2.4 Energy level scheme of the Gd^{3+}- Eu^{3+} system

CHAPTER 3

EXPERIMENT

3.1 Introduction

In order to investigate quantum cutting in samples of GdF_3, $GdLiF_4$, $ScPO_4$ and $GdZrF_7$ doped with trivalent rare earth ions, we first made a measurement of the emission spectra at room temperature and lower temperatures down to 77 K. Emission spectra were recorded with a CCD detector attached at the focal plane of a spectrometer. Emission was excited with monochromatic light from either a deuterium lamp filtered through a monochromator or the output of a F_2 gas discharge excimer laser operating at 157 nm. We also measured the excitation spectra of these samples. Excitation spectra were performed with a deuterium lamp source and VUV monochromator to select and scan the excitation wavelength. The emission was detected by a photomultiplier tube (PMT) and either glass or interference filters to select the emission. The excitation spectra were measured relative to that of sodium salicylate whose absolute quantum efficiency is estimated as nearly constant at 50% over the excitation wavelength range of interest [13]. Time resolved emission spectra were obtained with the F_2 laser which had a temporal pulse width of 10 ns. We measured the time resolved emission spectra at room temperature and lower temperature. All emission and absorption spectra (except as noted) were fully corrected for the wavelength dependent response of the CCD or PMT as described below.

3.2 Experimental Equipment

The apparatus used to performs these measurements consists of an Acton Research Corporation VM502 VUV monochromator, equipped with a deuterium lamp, GAM Laser Inc.

EX5 Excimer Laser, a vacuum system, a Keithley 485 auto ranging pico ammeter, an Acton Research Corporation SpectraPro-150 spectrograph equipped with ST-6B CCD camera from Santa Barbara Instrument Group, three photomultiplier tubes described below, a SR430 Multichannel Scaler, a Keithley 2000 Multimeter and a TDS 460A Digitizing oscilloscope from Tektronix. The setup is shown in Fig. 3.1. For temperature-dependent measurement, we made a cold finger to do the low temperature measurement. It is shown in Fig. 3.2

3.2.1 Light source and Monochromator

Two light sources were used in the experiment, a deuterium lamp and a F_2 gas discharge excimer laser emitting at 157 nm. This deuterium lamp provided a continuous emission spectrum from 115 nm to 370 nm.

As shown in Fig. 3.1, the deuterium lamp is used to measure the emission and excitation spectra. First the light from the deuterium lamp strikes a mirror which focuses the reflected light onto the entrance slit of the VM 502 monochromator. This monochromator was used to select a narrow band of wavelengths for excitation of the sample from the continuous spectral output of the lamp. The monochromator is evacuated and contains a concave diffraction grating to disperse the light on to the exit slit. The light with selected wavelength enters the sample chamber through the exit slit and excites the samples. Then the signal from the samples is focused by the lens 3 and detected by a CCD (emission spectrum) or a PMT (excitation spectrum).

The laser is air cooled. F_2 operation in the VUV is standard with up to 50 mW average output power at a repetition rate of 50 Hz. A new broadband optics set allows operation at 157 nm and 193 nm by simply changing the gas. While the laser is monochromatic in the VUV, light in the range of red and green is also emitted from the discharge. In order to removed this unwanted light, two narrowband interference filters are used for the 157 and 193 nm VUV wavelengths respectively. The laser includes an internal vacuum pump and halogen filter; there is no requirement for an external vacuum system.

3.2.2 Vacuum System

The vacuum system is composed of two pumps, two pumping lines and two valves. One pump is a mechanical pump which initially pumps down the sample chamber and the monochromator chamber; the other is a turbo-pump. One line connects the pump to the sample chamber; the other connects the pump to the monochromator chamber. The exit slit of the monochromator has a butterfly valve which can be closed to maintain the monochromator and lamp/mirror system under vacuum at all times.

3.2.3 Samples

Powder samples of GdF_3, $GdLiF_4$, $ScPO_4$ and $GdZrF_7$ doped with trivalent rare earth ions were prepared by solid state reaction by Professor Douglas Keszler and his group at Oregon State University. The samples were checked by X-ray diffraction analysis and found to be single phase. Samples of $GdLiF_4$: Nd containing 1, 2 and 3 mol% Nd were prepared in powder form. GdF_3 was first synthesized by heating a mixture of 1 Gd_2O_3 (99.99%, Alfa Aesar) and 8 NH_4F (99.99%, Alfa Aesar) at 900 °C for 1.5 hours. The resulting product was then mixed with 1.15 LiF (99.99%, Alfa Aesar), 0.01 Nd_2O_3 (99.99%, Alfa Aesar), and 4 NH_4F (99.99%, Alfa Aesar) and thoroughly ground. The mixture was then fired at 750 °C for 1.5 hours in a Pt crucible; the Pt crucible was covered and positioned inside an alumina crucible filled with activated carbon and NH_4F to limit the exposure of the sample to air. Samples of doped and undoped $ScPO_4$ were prepared in powder form by using Sc_2O_3 (99.999%, Standard Material Corporation), $(NH4)_2HPO_4$ (99.99%, Sigma-Aldrich), and Gd_2O_3 (99.99%, Standard Material Corporation.) The oxides were mixed according to the desired stoichiometric ratios of each sample, including a

10 mol% excess of $(NH4)_2HPO_4$. The mixtures were thoroughly ground and fired in alumina crucibles at 1150 °C for 3 hours. For the $GdZrF_7$ sample, the resulting products were ground a second time with an additional 10 mol% excess of the phosphate reagent. This mixture was then heated at 1350 °C for 3 hours. All samples were synthesized by solid state reaction. GdF_3 (Alfa Aesar, 99.99%), ZrF_4 (Aldrich, 99.99%), NH_4F (Aldrich, 99.99%) and lanthanides of Eu_2O_3 (Stanford Materials Corporation, 99.99%), Pr_6O_{11} (Alfa Aesar, 99.99%), TbF_3 (Alfa Aesar, 99.9%), Tm_2O_3 (Stanford Materials Corporation,99.99%), $Ce(NO_3)_3{\cdot}6H_2O$ (Aldrich,99.9%) depending on the kind of dopant were mixed well in stoichiometric ratio and were charged into carbon crucible capped with another carbon crucible to provide the raw mixture less oxygen atmosphere during heating. The ZrF_4 was added 12mol% in excess than the stoichiometric ratio. The carbon crucibles were put into a bigger aluminium crucible covered with lid and the space between the carbon crucibles and alumina crucible were filled with carbon powder. The heating was carried at 730 °C ~750 °C during 1.5~2 hours.

3.3 Experiment

3.3.1 Measurement of emission spectra

Samples were loaded into the cells of the sample holder. These cells were 0.5 mm deep circular holes of 8 mm diameter which were covered with MgF_2 crystal windows. To reduce the interference from the MgF_2 covers, smaller or larger incident angles other than 45° of the VUV beam to the sample surface can be used. In this way, the reflected VUV beam from the MgF_2 covers does not directly hit the optics. In this series of experiments, we set θ at 35° (refer to Fig. 3.1). When the deuterium lamp was used as a light source, we recorded the spectra from the window with lens 3. When we used the laser to excite the samples, the sample holder was rotated by 180° and we detected the spectra from the window with lens 2. When measuring the emission spectrum in VUV, we rotated the sample holder clockwise 90° from the original position and used the laser to excite the samples.

In the CCD mode we used an Acton Research Corporation SpectraPro-150 spectrograph equipped with ST-6B CCD camera from Santa Barbara Instrument Group. This spectrograph separates the emission light from the sample by wavelength and produces a spectrum from the sample. The emission spectrum is recorded by the CCD camera.

In the PMT mode we used the F_2 laser to excite the sample and the emission was detected by a Solar Blind VUV PMT.

For the low temperature measurement, we loaded the sample in the holder of the cold finger and poured liquid N_2 into the reservoir. A type K thermocouple is attached to the cold finger. We used a Keithley 2000 Multimeter to monitor the temperature of the cold finger during the measurement.

1. Wavelength calibration of the CCD

In order to make precise measurements of the wavelength, we needed to calibrate our equipment. The wavelength calibration of the CCD was done using emission lines, 253.65, 365.02, 435.84, 546.07, and 734.64 nm of a mercury lamp. The wavelengths determined from the manufacturer calibration were off to these wavelengths by 1.027, 1.00, 0.985, 0.951, 0.908nm, respectively. So on average, the wavelength detected is 1nm below the actual wavelength. To obtain the actual wavelength, a 1 nm correction was added to the wavelength defined above for the CCD.

2. Spectral calibration of CCD scan coverage

The detector coverage of this CCD is 85 nm with a 600g/m grating. The wavelength range of the emission spectrum is from about 210-940 nm. We could not get the whole spectrum at one time. We therefore divided the spectrum into 9 parts, labeled by the values 1-9 in Table 3.1, and measured them respectively. They were fit together to construct the whole emission spectrum. The spectral dispersion of the instrument ($d\lambda/dl$) was found to be slightly wavelength dependent. It decreases with wavelength almost linearly. The dispersion can be fit by the following equation:

$$d\lambda / dl = C_i = 0.34648 - 0.0000831 \times (\lambda_{i0} - 220) \tag{3.1}$$

Here λ_{i0} is the central wavelength of each detector coverage and dl is the distance between pixels. So, if given the wavelength (for example, the central wavelength to be defined for each detector coverage), the spectral position of each pixel near that wavelength can be evaluated. The wavelength range of the each detector coverage can then be calculated:

$$\lambda = \lambda_{i0} + C_i \times (I - 125), \quad I \text{ from 1 to 250} \tag{3.2}$$

The scan groups we used in the measurement are shown in Table 3.1.

Part	λ_{i0} (nm)	C_i	Range (nm/pixel)
1	260	0.3432	217.4-302.9
2	345	0.3361	303.3-387.0
3	428	0.3292	387.2-469.2
4	510	0.3224	470.0-550.3
5	590	0.3157	550.9-629.5
6	668	0.3093	629.7-706.7
7	745	0.3029	707.4-782.9
8	820	0.2966	783.2-857.1
9	894	0.2905	858.0-930.3

Table 3.1

3. Spectral response of the Acton CCD

a. Scattered light

In practice, the measured radiation spectrum from the calibration lamp is always mixed with stray light originating from light of the input lamp beam which is scattered inside of the spectrometer. The stray light becomes more serious for a spectrograph in a short wavelength region and for a CCD detector. It is especially serious in the UV region. The UV emission of a tungsten lamp is three orders of magnitude weaker than its visible light and this visible emission could add to the measured emission spectrum at each pixel of the CCC. Below we describe how we minimize errors resulting from the scattered light.

Some of the light from the calibrated sources at wavelengths other than the detection wavelength which enters the monochromator gets scattered by optical surfaces in the monochromator and reaches the CCD along random paths. In order to reduce the influence of this stray light, a series of interference filters were specifically selected to transmit only the spectrum with wavelength range of that scan. However the filter does not have 100% transmission in the wavelength range covered by one CCD scan. Even with the filter there is still some scattered light. The actual spectrum $S(\lambda)$ of the lamp in the spectral range is obtained by dividing the measured signal $S_{meas}(\lambda)$at each λ by the transmission of the filter $T(\lambda)$ at that wavelength.

$$S(\lambda) = \frac{S_{meas}(\lambda)}{T_{filter}(\lambda)} \tag{3.3}$$

b. Spectral response

The diffraction efficiency of a grating and sensitivity of a CCD detector are both a function of wavelength. Therefore, the spectral response of a CCD system needs to be measured in order to obtain a true spectrum. In general, the spectral response of a CCD can be determined by measuring the radiation spectrum of a calibrated lamp (tungsten lamp).

In order to remove other diffraction orders of grating, we used a series of interference filter before the lamp and measured the spectra. Because the spectrum of this lamp and the transmission of these filters are known, we could use Eq. (3.4) to calculate the spectral response (relative quantum yield) of the CCD system.

$$R(\lambda) = \frac{S(\lambda)}{\lambda I(\lambda)} = \text{Relative quantum yield} \tag{3.4}$$

$S(\lambda)$ is the measured photocurrent as a function of λ converted for the transmission of the filter as in Eq. (3.3) and $I(\lambda)$ is the known lamp output in mW/m^{2}nm at 50 cm from the lamp.

The corrected emission spectrum of samples can be obtained if the spectral response of the CCD is known:

$$E_0(\lambda) = C\, E(\lambda)/R(\lambda) \tag{3.5}$$

$E(\lambda)$ is the emission (counts) recorded by the CCD. C is an arbitrary constant which will be cancelled in the calculation of relative quantum efficiency introduced in Sec. 3.3.2.

3.3.2 Measurement of excitation spectra

An excitation spectrum is obtained by observing changes in the emitted light intensity at a set wavelength while varying the excitation energy. When the excitation source is a lamp, single-frequency light produced by a monochromator impinges on the sample and the emitted light intensity is recorded as the excitation wavelength is varied.

As shown in Fig. 3.1, we used the deuterium lamp as source light in the experiment. The light from the lamp strikes a focusing mirror which focuses the reflected light onto the entrance slit of the VM 502 monochromator. This monochromator was used to select a narrow band of wavelengths for excitation of the sample from the continuous spectral output of the lamp. The output of the monochromator is focused onto the sample. The emission was detected with an Oriel photomultiplier tube (PMT).

The excitation spectra are measured relative to that of sodium salicylate whose absolute quantum efficiency is estimated as nearly constant at 50% over the wavelength range of interest.[25] Therefore the excitation spectrum of sodium salicylate has a similar profile to that of the deuterium lamp. The relative excitation efficiency curve of the sample can be similar to its absorption spectrum if its quantum efficiency was constant but this is generally not the case.

In this dissertation, the relative excitation spectrum of a sample is defined as:

$$\begin{aligned} R(\lambda_{excit}) &= \frac{I_{sample}(\lambda_{excit})}{P(\lambda_{sample})}\left[\frac{I_{ref}(\lambda_{excit})}{P(\lambda_{ref})}\right]^{-1} \\ &= \frac{I_{sample}(\lambda_{excit})}{I_{ref}(\lambda_{excit})}\frac{P(\lambda_{ref})}{P(\lambda_{sample})} \end{aligned} \tag{3.6}$$

where $I_{sample}(\lambda_{excit})$ and $I_{ref}(\lambda_{excit})$ are the emission intensities measured by the PMT. $P(\lambda)$ is the spectral response of the PMT. The calculation of the $P(\lambda)$ is shown in Appendix.

In a practical measurement, the result can be complicated by many factors. These include (1) the effect of scattered and background radiation; (2) correcting for the presence of multiple emission wavelengths where the quantum efficiency of the PMT has different values and (3) the consequence of the emission spectrum changing as a function of excitation wavelength. How to minimize the effects of these factors are described in Appendix.

3.3.3 Measurement of lifetime

As shown in Fig. 3.1, we used the laser to excite the sample. The laser beam was focused by the lens of focal length 2 inches onto the sample. The emission from the sample was detected by a Hamamatsu R943 PMT from the window with lens 2. A TDS 460A Digitizing oscilloscope from Tektronix was connected to the PMT to record the time resolved spectrum. We also used a SR430 Multichannel Scaler to record time resolved spectrum. We measured the time resolved spectrum at room temperature and low temperature.

When we used the oscilloscope to measure the lifetime of the sample, we need different time resolution. In our measuring circuit, the product of resistor R and capacitance C is a constant τ. The capacitance is fixed for this oscilloscope. So we selected different resistors correspondingly.

In general, we used the smallest resistance that provided an adequate voltage response. A series of time resolution spectra were averaged on the oscilloscope for 100 - 10000 laser shots depending on the emission intensity.

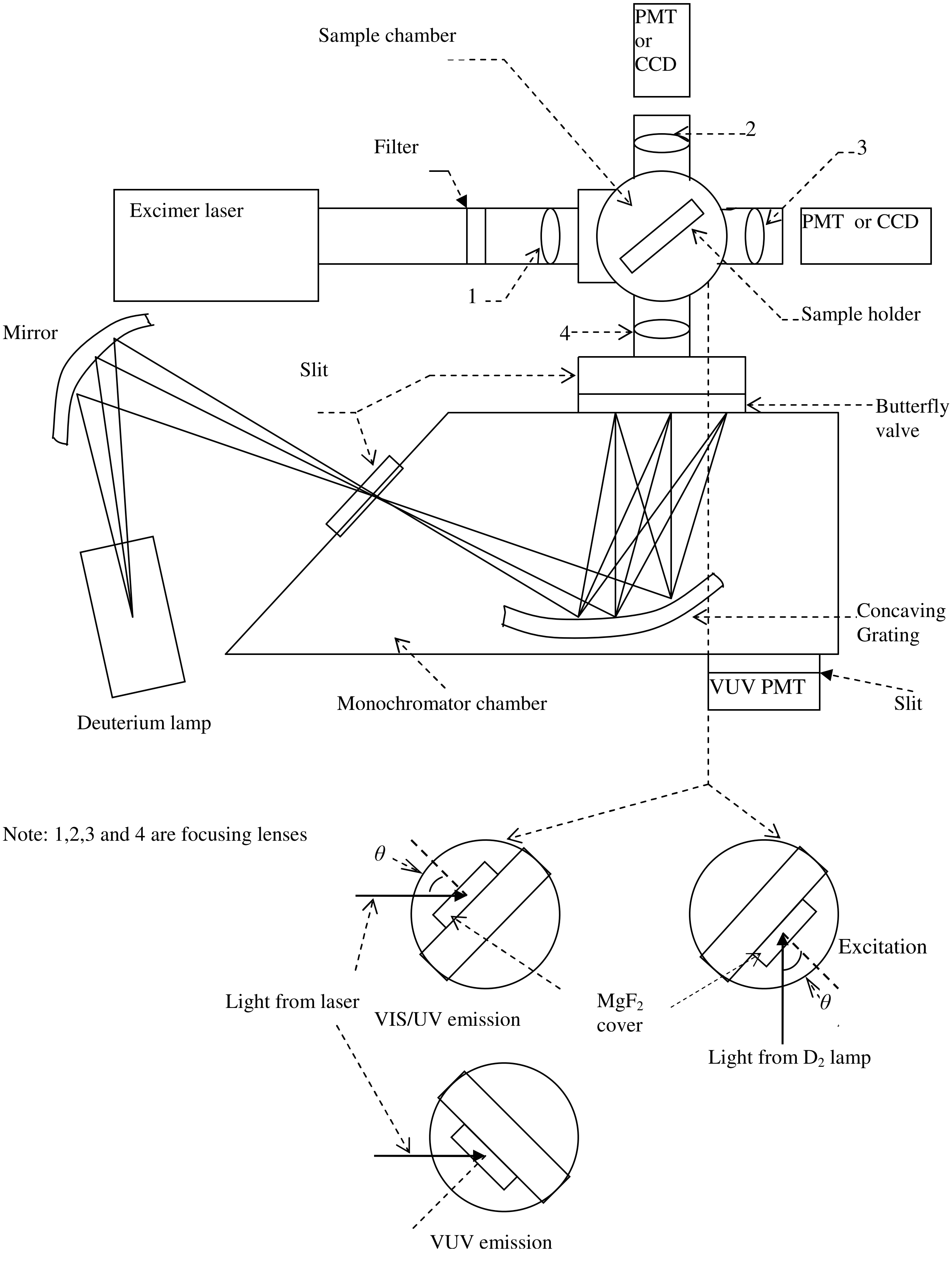

Note: 1,2,3 and 4 are focusing lenses

Fig. 3.1 Schematic setup for measurement

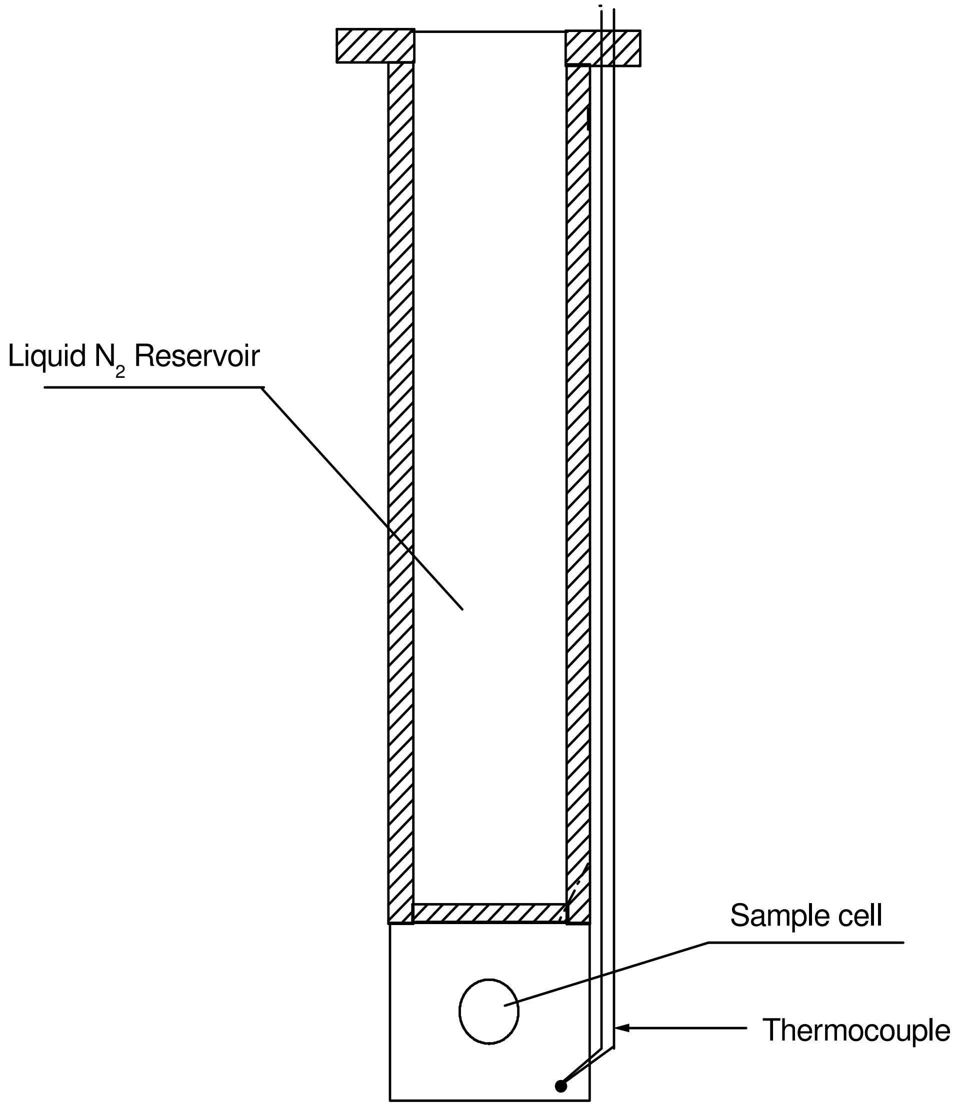

Fig. 3.2 Cutaway view of cold finger

CHAPER 4

Sensitization with Pr 5d→4f as donor

4.1 Introduction

As we mentioned in chapter 2, Gd-Eu quantum cutting has been found in a number of solid lattices [14–17], with reported internal quantum efficiencies up to 190% [14]. But there is a problem for the application of this kind of phosphor. Because the absorption of Gd^{3+} in the VUV is a parity-forbidden 4f-4f transition, the visible quantum cutting is not very effective at connecting the incident VUV light to visible photons even though the internal quantum efficiency is 190%.

A possible way to solve this problem is the incorporation of a good VUV absorbing ion which subsequently transfers its energy to Gd^{3+}, populating the Gd^{3+} ^6G_J levels. Such a species is generally known as a sensitizer. We use the 5d→4f transition of Pr as a sensitizer for Gd-Eu quantum cutting. A necessary condition for Gd^{3+} sensitization is that the sensitizer ion should have a strong absorption which leaves it in a metastable excited state above the ^6G states of Gd^{3+}. For Pr^{3+} this requires a host with a very small crystal field to minimize the crystal field depression of the 4f5d configuration. GdF_3 satisfies this requirement and is the subject of this study. It is shown that while the ^6G states of Gd^{3+} exhibit strong quantum cutting in GdF_3, excitation of the 4f5d state of Pr^{3+} does not result in efficient quantum cutting. Through studies of the emission, excitation and time-resolved dynamical studies, we examine the reasons for the ineffective generation of quantum cutting.

The energy level diagram along with the relevant energy transfer processes are shown in Fig. 4.1. When the Gd^{3+} is excited to its ^6G states, a cross relaxation energy transfer with Eu^{3+} occurs, shown by the dashed arrow labeled e, whereby the Gd^{3+} ion undergoes a transition $^6G \rightarrow {}^6P$ while a nearby Eu^{3+} ion undergoes a resonant an upward transition $^7F_1 \rightarrow {}^5D_0$. The excited Eu^{3+} ion emits the first photon. The Gd^{3+} ion in the $^6P_{7/2}$ excited state then transfers its energy to Eu^{3+} as shown by the arrow labeled j. This is followed by non-radiative relaxation among the ^5D_J levels, all of which emit producing the second photon in the quantum cutting.

4.2 Emission spectrum

The emission spectrum of GdF_3: 0.3% Pr, 0.2% Eu is shown in Fig. 4.2 for excitation at two wavelengths. For 275 nm excitation with an Ar^+ laser, Gd^{3+} is excited directly to the ^6I states from which quantum cutting cannot occur because it lies below the ^6G levels. Energy transfer to Eu^{3+} still occurs and one sees emission from all the ^5D_J levels. Pr^{3+} cannot be excited for 275 nm excitation. Upon excitation at 160 nm with a deuterium lamp one excites the 4f5d state of Pr^{3+}. One again sees emission from all the ^5D_J states of Eu^{3+}. However, the $^5D_0$ is greatly enhanced and emission from $^6P_{7/2}$ of Gd^{3+} is now observed. In GdF_3 samples containing only Eu^{3+}, no $^6P_{7/2}$ Gd^{3+} emission is observed whereas the Eu^{3+} $^5D_0$ emission is still increased. As discussed in Sec. 4 .3, this indicates that Pr^{3+} does sensitize Gd^{3+} but it is not responsible for the increased $^5D_0$ emission.

4.3 Excitation spectra

Excitation spectra, detecting all emission $\lambda > 320$ nm, of GdF_3: 0.3% Pr, 0.2% Eu and several other samples with different dopant concentrations are shown in Fig. 4.3. At 275 nm one sees excitation feature of the ^6I states of Gd^{3+}. At 202 nm and 195 nm the sharp features indicate the ^6G levels of Gd^{3+}. Below 190 nm, the 4f5d bands of Pr^{3+} are observed. The band between 150 and 160 nm is the charge transfer (CT) band of Eu^{3+}; therefore, at 160 nm both Pr^{3+} and Eu^{3+} are excited. These excitation spectra are obtained relative to that of sodium salicylate whose excitation spectrum is nearly independent of wavelength with an absolute quantum yield of about 0.6. Based on this, the maximum quantum yield for total emission occurs for the 0.3% Pr, 0.2% Eu sample and has a disappointing value of only about 0.2 at about 160 nm. Thus it appears that GdF_3: Eu sensitized by Pr^{3+} is not a useful quantum cutting phosphor. While excitation of the 4f5d states of Pr^{3+} does sensitize excitation of Gd^{3+} it does not lead to high quantum yields. Nonetheless, it will be useful to study the dynamics and examine the possible causes for its limited performance.

Evidence for strong quantum cutting from the ^6G levels of Gd^{3+} is shown in Fig. 4. 4 for a sample of GdF_3: 0.3% Pr, 0.03% Eu. Here the excitation spectra are obtained by selecting different emission wavelength regions. The spectra are approximately normalized to the Gd^{3+} ^6I excitation peak. When only $^5D_0$ emission is detected, the ^6G excitation peaks are enhanced by more than a factor of 5 relative to the ^6I peak when compared to detection wavelengths between 400-560 nm where only the $^5D_{J>0}$ emission is detected. A very large enhancement is still found for $\lambda_{det} > 320$ nm where all emission is monitored. This preferential generation of population in $^5D_0$ results from the cross relaxation energy transfer shown by the dashed arrow labeled e in Fig. 4.1. Under ideal conditions of quantum cutting, the enhancement should be no more than a factor of 2. The observation of a much larger enhancement results from (1) the fact that a large fraction of the Eu^{3+} emission occurs from states other than $^5D_0$ and (2) the possibility that the $Gd^{3+}(^6P_{7/2})\rightarrow Eu^{3+}$ energy transfer may be much less than 100% efficient.

The question of sensitization of Gd^{3+} is now considered with the aid of Fig. 4.1. There exist a number of possible routes by which Pr^{3+} can transfer energy to Gd^{3+}. These are shown by the solid arrows labeled a through d. Förster-Dexter energy transfer requires overlap of the emission of the donor and absorption of the acceptor. A number of emissive transitions from Pr^{3+} can occur which are nearly resonant with absorptions of Gd^{3+}. The Pr^{3+} emission has been shifted to lower energy relative to the bottom of the 4f5d band by half the Stoke's shift or about 2500 cm^{-1}, reflecting the effect of the large known Stoke's shift of 5d emission in the isostructural LaF_3 [18]. One sees that in view of the broad band characteristics of 5d→5f emission (~2000 cm^{-1}) near resonances occur for all the processes a through d. Unfortunately, only one of these, a, will generate the desired ^6G population. Thus, unless this dominates the energy transfer, the quantum cutting will not be highly efficient.

4. 4. Dynamics of Relaxation

The relative contribution of the different $Pr^{3+} \rightarrow Gd^{3+}$ energy transfer processes can be obtained by studies of the dynamics of the Gd^{3+} emission. In Fig. 4. 5 the dynamics of emission from ^6I (279 nm) and $^6P_{7/2}$ (312 nm) are compared for three samples of different Eu^{3+} concentrations. The $^6P_{7/2}$ emission of the sample with 0.3% Pr and only a trace amount (<0.01%) of Eu shows that >80% of the $^6P_{7/2}$ population arises from relaxation from ^6I since the component of $^6P_{7/2}$ that shows a measurable rise has a rise time equal to the decay time of ^6I. The fast rise time component of the ^6P emission results either from energy transfer (process a) followed by a CRET (process e) or some other rapid feeding of ^6P. The mechanism of the relaxation process $^6I \rightarrow {}^6P$ in Gd^{3+} is either multi-phonon relaxation or a possible second cross relaxation energy transfer labeled f in Fig. 4.1. It is clear that process f is important since the relaxation time depends on Eu^{3+} concentration as seen in Fig. 4. 6. However, even in the sample with a trace Eu^{3+} concentration, multi-phonon relaxation in a low phonon frequency material such as GdF_3 is unlikely to explain the ~2-5 μs decay time for an energy gap of ~3000 cm^{-1}. The decay rate of the $^6P_{7/2}$ emission of Gd^{3+} increases with Eu^{3+} concentration indicating that it results from energy transfer to Eu^{3+} (process j in Fig. 4.1).

4. 5. Conclusion

Efficient quantum cutting occurs when ^6G of Gd^{3+} is excited. Pr^{3+} rapidly and effectively sensitizes Gd^{3+} in GdF_3: Pr, Eu. However, the energy transfer predominantly feeds ^6I rather than ^6G of Gd^{3+} severely limiting possible quantum splitting. The relaxation of ^6I proceeds to ^6P probably by a cross relaxation energy transfer with Eu^{3+}.

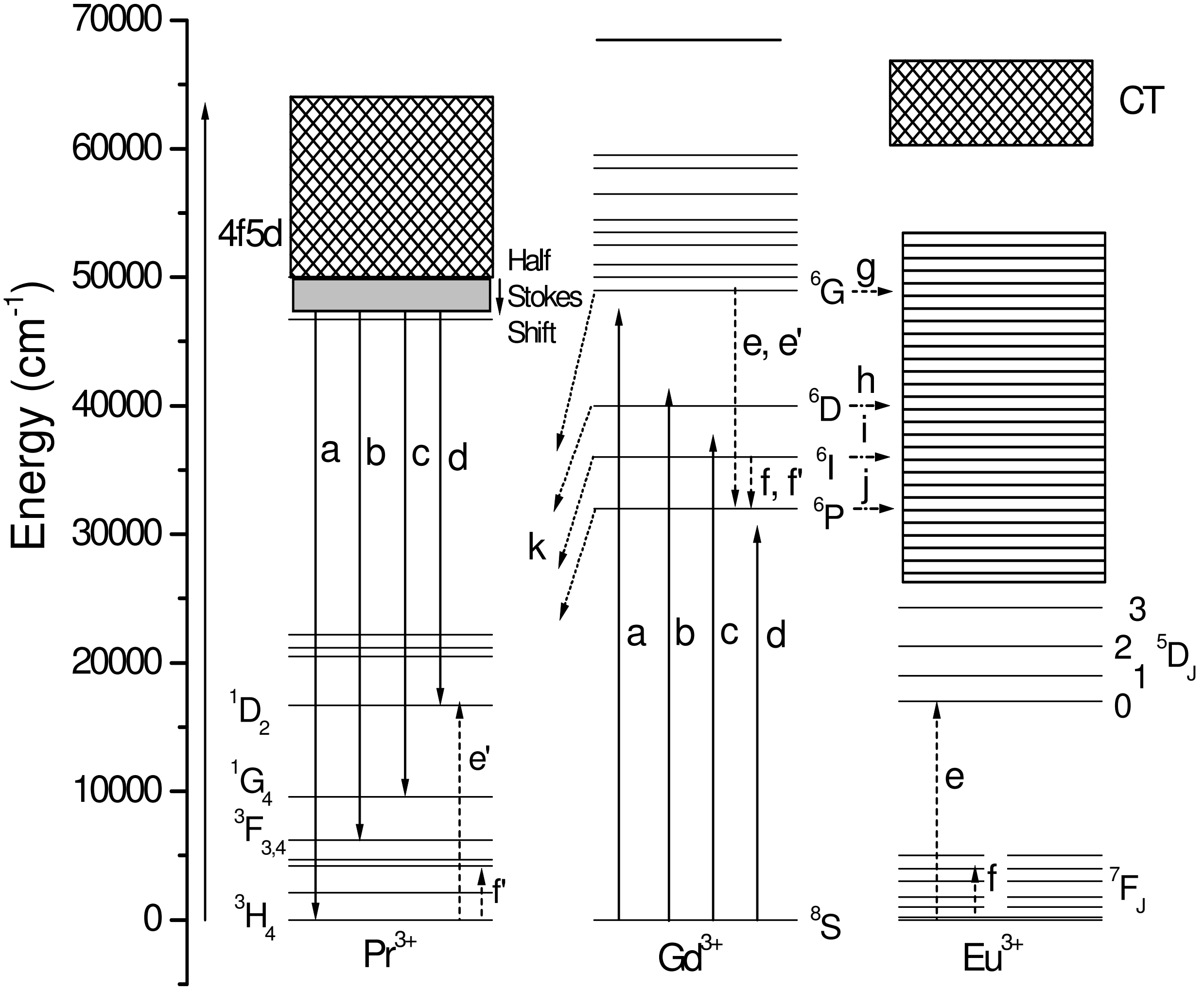

Fig. 4.1 Energy level diagrams for Pr^{3+}, Gd^{3+}, and Eu^{3+}

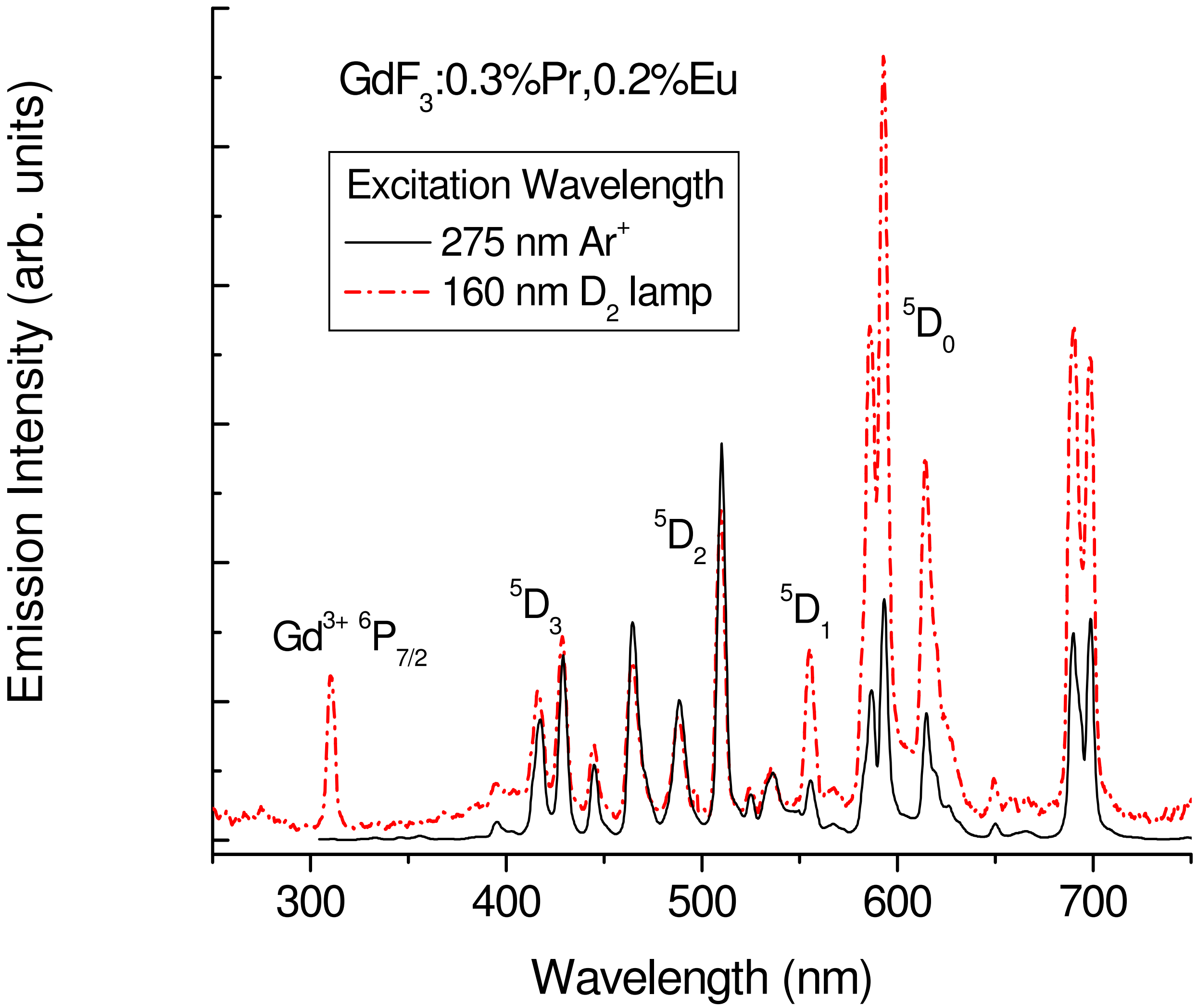

Fig. 4.2 Emission spectra excited at 275 nm (^{6}I state of Gd^{3+}) and 160 nm (4f5d state of Pr^{3+})

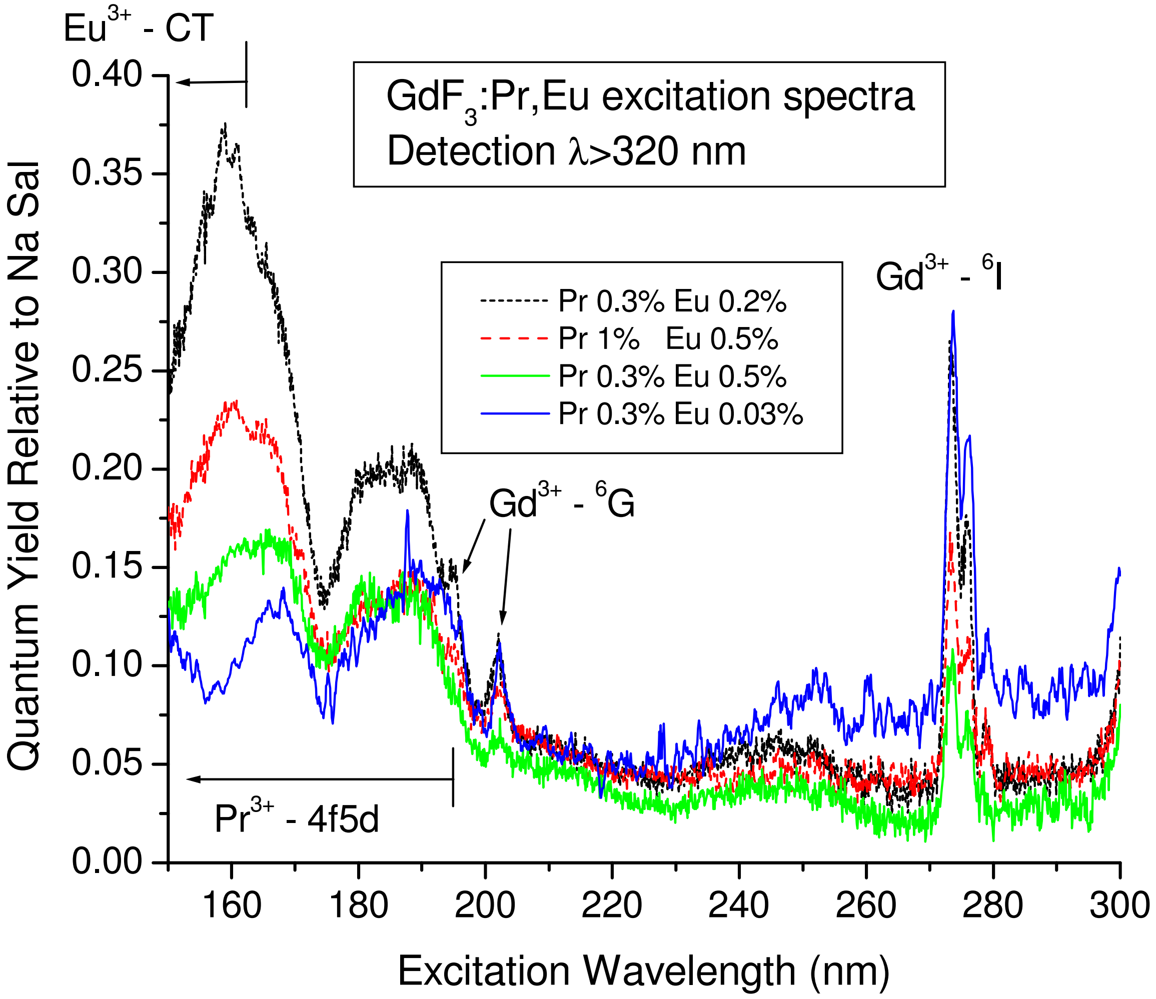

Fig. 4.3 Excitation spectra of four samples of GdF$_3$:Pr,Eu

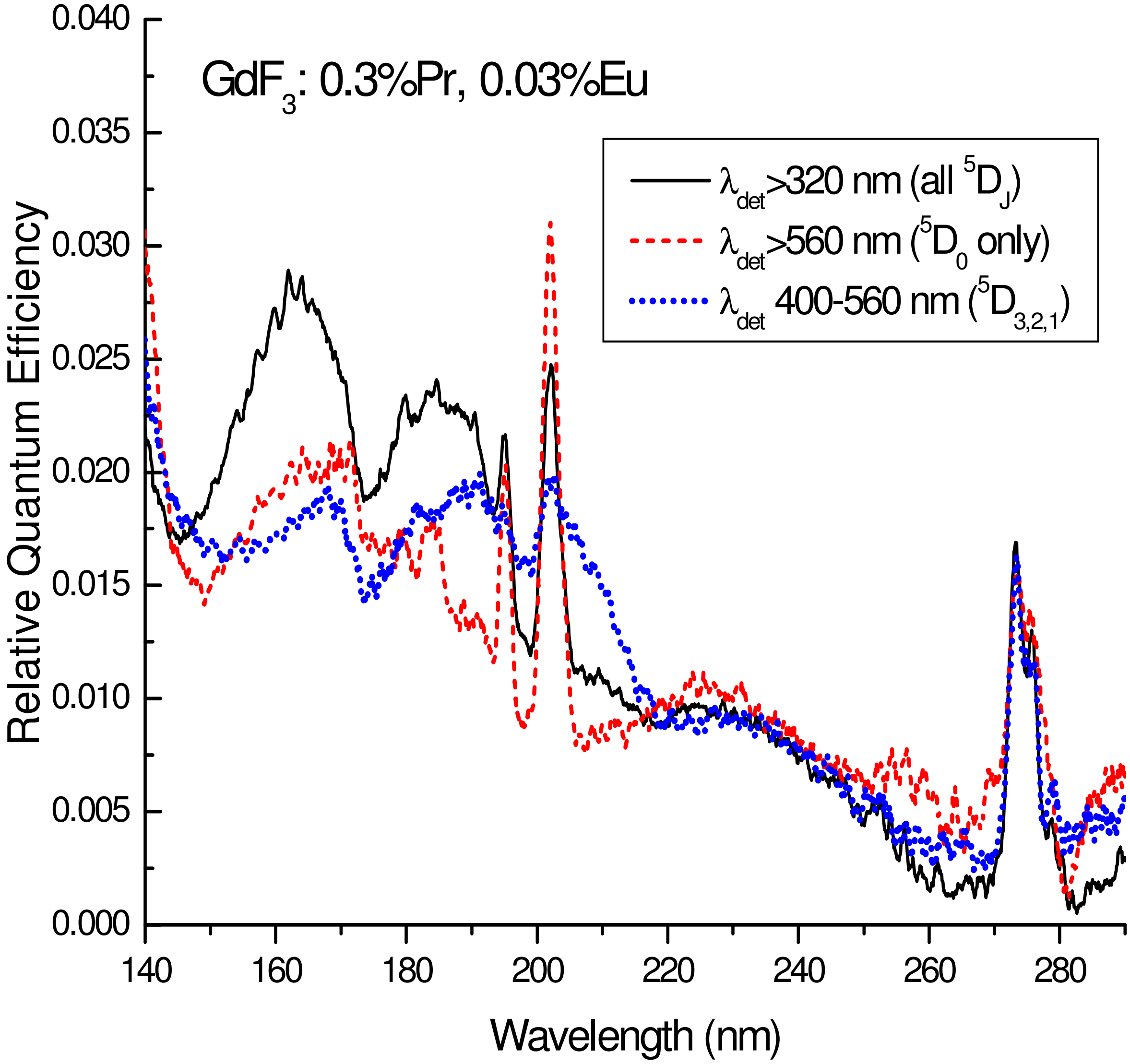

Fig. 4.4 Excitation spectra of GdF$_3$:Pr,Eu

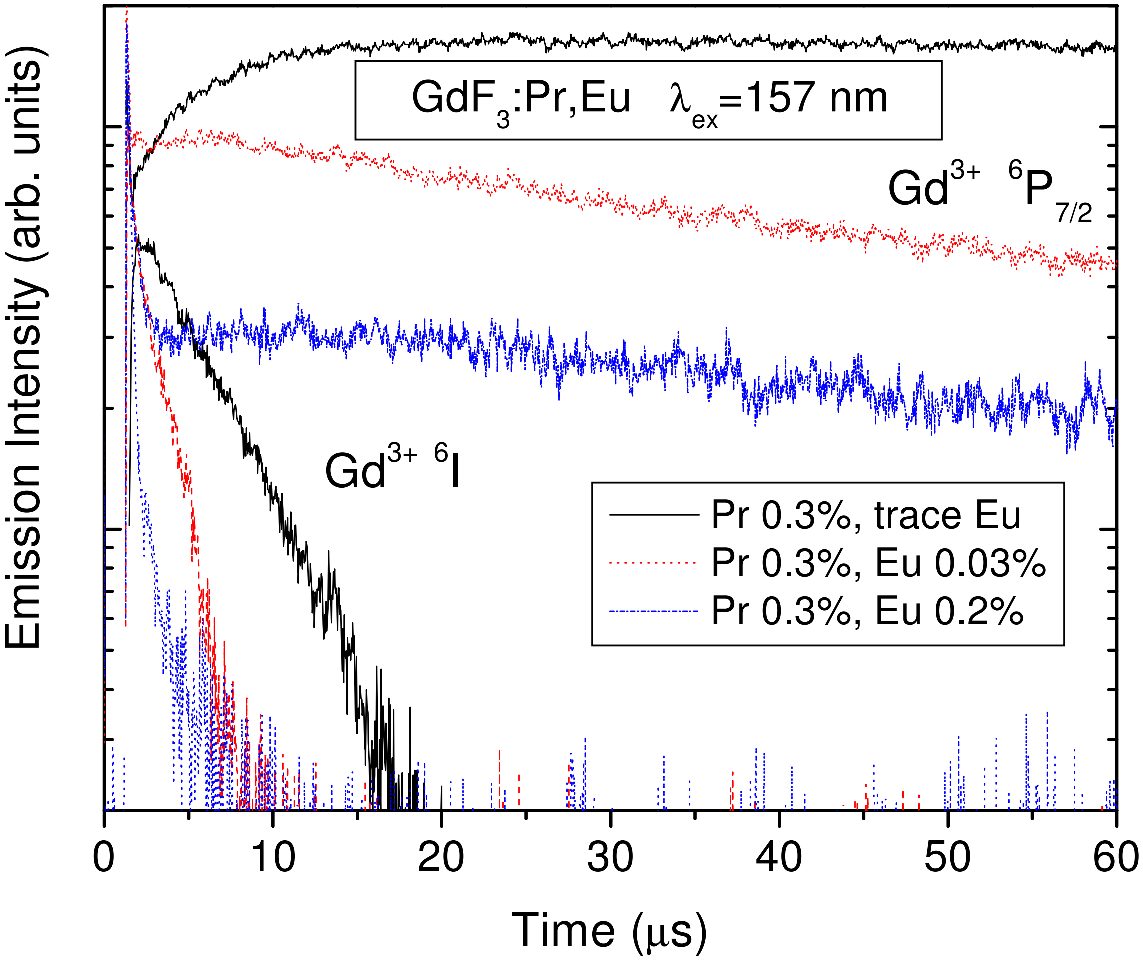

Fig. 4.5 Time-resolved emission for ^{6}I and ^{6}P$_{7/2}$ of Gd^{3+}

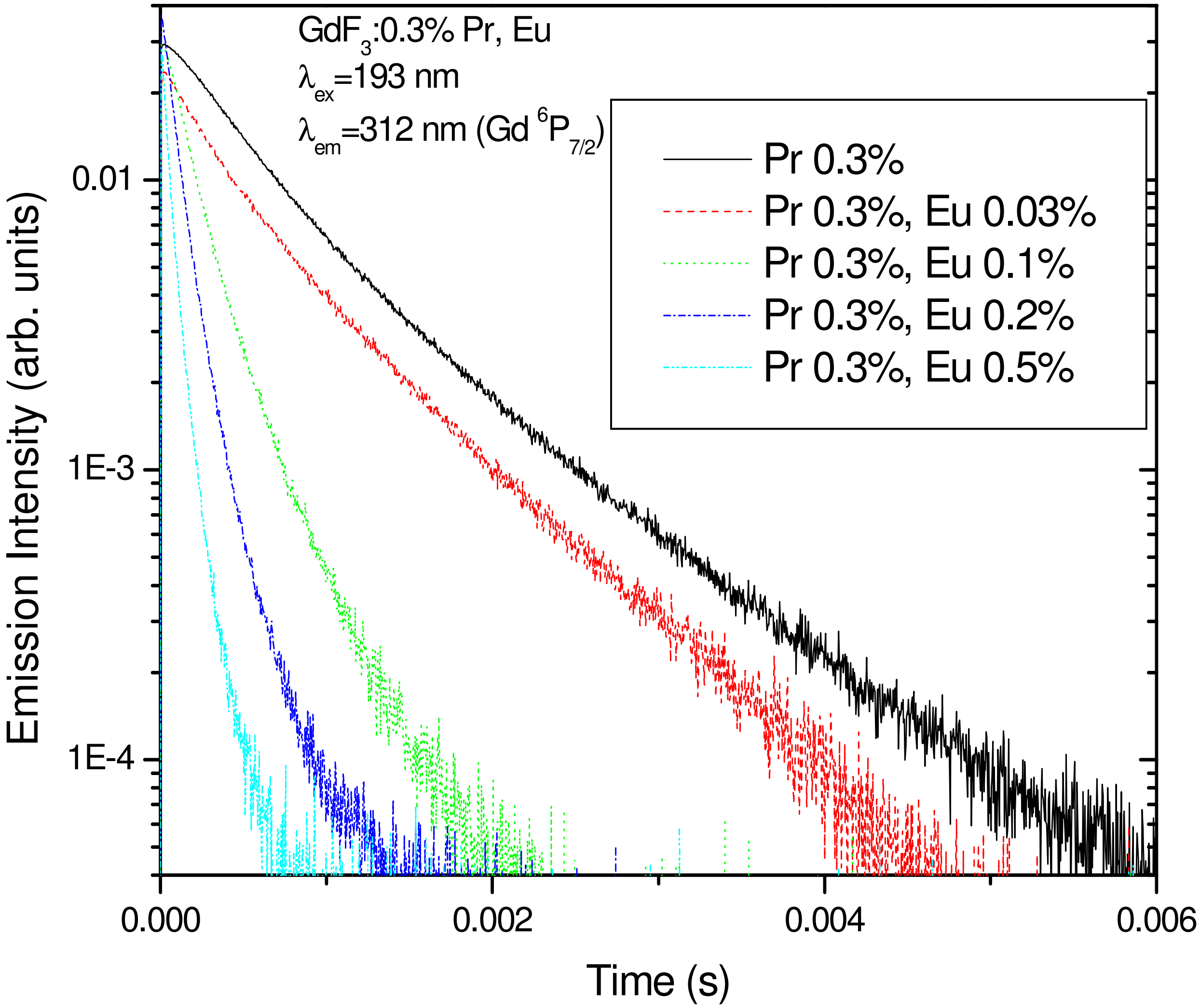

Fig. 4.6 The relaxation time depends on Eu^{3+} concentration

CHAPTER 5

Sensitization with Nd 5d→4f as donor

5.1 Introduction

Cross relaxation induced quantum cutting has been described for $GdLiF_4$: Eu with an internal quantum efficiency of 190% [3]. For the cross relaxation scheme in $GdLiF_4$: Eu, the absorption of the VUV photon is too weak to produce a phosphor with high brightness [19]. We attempted to sensitize the absorption by adding Nd^{3+} to $GdLiF_4$: Eu^{3+}. We found that Nd^{3+} does effectively sensitize the excitation of Gd^{3+}. However, in addition, Nd^{3+} undergoes its own very strong cross relaxation with the Gd^{3+} system producing efficient quantum cutting. A similar effect has recently been reported for $GdLiF_4$: Tm^{3+} [20].

In this chapter, we studied the quantum cutting process for the singly-doped system, $GdLiF_4$: Nd. The result of exciting Nd^{3+} into the $4f^2 5d$ state in the VUV is the appearance of two infrared photons. While this material will not be a commercially viable quantum cutting phosphor since the photons are in the infrared and because of the large energy loss even if two photons were produced per input photon, its study provides important insights into the dynamics and mechanisms of the quantum cutting process. This process seems to depend strongly on rapid energy migration among the Gd^{3+} ions and the presence of very closely coupled pairs. In order to gain a further insight into the mechanism of the CRET process, the emission and excitation spectra, along with the dynamics of the emission, as a function of Gd^{3+} concentration are studied in the mixed crystal system $Gd_xY_{1-x}LiF_4$: Nd.

5.2 Emission Spectrum

In Fig. 5.1 the emission spectrum is presented for two different excitation wavelengths, 351 and 160 nm. The emission from 200 nm to 950 nm is dominated by the $^4F_{3/2} \rightarrow {}^4I_{9/2}$ transition. However emission from the $^4D_{3/2}$ and $^2P_{3/2}$ states of Nd^{3+} is also observed. Weak emission from the $^6P_{7/2}$ state of Gd^{3+} is observed at 313 nm. Though it is not evident in this time-averaged spectrum, emission at 281 nm from the ^6I state of Gd^{3+} also does occur. Emission from the $4f^25d$ state of Nd^{3+} in the wavelength range of 180 nm to 270 nm, which dominates the spectrum of $YLiF_4$: Nd [21], is not observed in $GdLiF_4$: Nd suggesting efficient energy transfer from Nd^{3+} to Gd^{3+}.

When we compare the spectra excited at the two different wavelengths, by normalizing them to the $^4D_{3/2}$ and $^2P_{3/2}$ emission, it is seen that under 160 nm excitation, the relative intensity of the $^4F_{3/2}$ emission is more than double that observed for 351 nm excitation. This suggests a process which enhances the excitation of $^4F_{3/2}$ in a manner which was used to identify quantum cutting for $GdLiF_4$: Eu [3]. This is just the cross relaxation process responsible for quantum cutting.

The processes are illustrated in Fig. 5.2. The diagram shows the relevant $4f^3$ and $4f^7$ energy levels of Nd^{3+} and Gd^{3+}, respectively. Boxed regions with horizontal lines indicate a high density of states of the two $4f^n$ configurations for which rapid multiphonon relaxation occurs. The open box represents the $4f^25d$ band of Nd^{3+}. The $4f^65d$ band of Gd^{3+} is off the energy scale and is not relevant here. The long vertical arrow represents the VUV excitation of Nd^{3+} into the $4f^25d$ band. Rapid energy transfer to a nearly resonant $4f^7$ state of Gd^{3+}, labeled by ET 1, followed by rapid non-radiative relaxation, populates the ^6G_J states of Gd^{3+}. Cross relaxation energy transfer from the $^6G_{7/2}$ state of Gd^{3+} can occur via two paths. The first one, indicated by the dashed arrows labeled A on the energy level diagrams of Gd^{3+} and Nd^{3+}, results in a transition $^6G_{7/2} \rightarrow {}^6P_J$ on

Gd^{3+}, as has been previously observed in the Gd-Eu couple, with a simultaneous $^4I_{9/2} \rightarrow {}^4G_{5/2}$ excitation on Nd^{3+}. These two transitions have considerable overlap as shown in the room temperature spectra of Fig. 5.3 where the $^6G_J \rightarrow {}^6P_J$ emission of Gd^{3+} observed in $YLiF_4$: Gd is compared to the $^4I_{9/2} \rightarrow {}^4G_{5/2}$ absorption of $YLiF_4$: Nd [22]. Subsequently, rapid multiphonon relaxation leads to feeding of the $^4F_{3/2}$ metastable state from which strong IR emission occurs.

The second pathway involves a transition $^6G_{7/2} \rightarrow {}^6I_J$ on Gd^{3+} coupled with a $^4I_{9/2} \rightarrow {}^4F_{5/2}$, $^2H_{9/2}$ or $^4F_{7/2}$ transition on Nd^{3+} as indicated by the dashed arrows labeled B in Fig. 5.2. Although the spectra are not available for comparison, the transition energies for Nd^{3+} in absorption [23] and Gd^{3+} predicted for emission [20] are likely to have good resonances. In addition, Peijzel *et al.* [20] have shown that the reduced matrix elements for this second pathway are about an order of magnitude greater than for the first, making this process about two orders of magnitude faster under the similar resonance conditions. Indeed, as will be shown from studies of the dynamics, the pathway involving the ^6I_J levels does dominate the cross relaxation from $^6G_{7/2}$. However, ^6I_J can further relax to ^6P_J via another cross relaxation process, shown by the dashed arrows labeled C in Fig. 5.2, that excites the $^4I_{13/2}$ state of Nd^{3+}. Evidence for this also exists from the dynamical studies discussed below.

The ^6P_J states of Gd^{3+} then transfer their energy to the nearly resonant $4f^3$ states of Nd^{3+}, as shown by the arrow labeled ET 2. Above the $^4D_{3/2}$ state of Nd^{3+} there is a very dense, almost continuous forest of energy levels from the $4f^3$ configuration among which the $^2L_{17/2}$ at ~32,000 cm^{-1} is in closest resonance with the $^6P_{7/2}$ states of Gd^{3+} [23]. Once excited, these will relax almost immediately to the $^4D_{3/2}$ level which lives long enough to produce observable emission. Its decay, whose lifetime is about 1 μs, is dominated by non-radiative relaxation to the $^2P_{3/2}$ level which lives much longer with a lifetime of ~20 μs. These and subsequent multiphonon relaxations ultimately feed the ${}^4F_{3/2}$ level leading to the emission of a second IR photon. On the other hand, when the ${}^4D_{3/2}$ state is excited directly at 351 nm, the cross relaxation step is eliminated so that the relative intensity of ${}^4F_{3/2}$ emission is less than half of that obtained under 157 nm excitation. As described by Wegh *et al.* [3] for $GdLiF_4$: Eu, this is strong evidence for quantum cutting. The dynamics of the system described below will provide further supporting evidence.

Finally, it should be noted that the assumption that the initial $Nd^{3+} \rightarrow Gd^{3+}$ energy transfer (ET1 in Fig. 5.2) occurs to Gd^{3+} states resonant with the $4f^2 5d$ state of Nd^{3+} may not be a good one. Many possible cross relaxation energy transfer processes are equally possible. These could excite many of the lower-lying states of Gd^{3+} below the energy of the $4f^2 5d$ state of Nd^{3+} (~56,000 cm^{-1}), shown on the Gd^{3+} energy level diagram as the boxed area with many horizontal lines in Fig. 5.2. For example, cross relaxation processes could leave Nd^{3+} in the ${}^4I_J$ levels J=11/2, 13/2, 15/2 and Gd^{3+} in states above ${}^6G_J$ that conserve the total energy. Note that rapid multiphonon relaxation would still lead to a build up in the population of the ${}^6G_J$ levels of Gd^{3+} as had been assumed. Cross relaxation processes are also possible in which the energy transfer would result in Gd^{3+} being excited to ${}^6D_J$, ${}^6I_J$, or ${}^6P_J$ by leaving Nd^{3+} in its ${}^4F_{9/2}$ (14,800 cm^{-1}), ${}^4G_{7/2}$ (19,000 $cm^{-1)}$, or ${}^4G_{11/2}$ (21,400 cm^{-1}) states, respectively. However, these processes would also still all lead to quantum cutting since multiphonon relaxation would populate ${}^4F_{3/2}$ and the excited Gd^{3+} ion would still be capable of transferring its energy to Nd^{3+} for producing the second photon. These processes would supplement the energy transfer processes labeled as A and B that were previously discussed.

We also measured the emission spectrum of the mixed crystal system $Gd_xY_{1-x}LiF_4$: Nd. It is presented in Fig. 5.4. Note that the 5d emission of Nd^{3+} is now observed. Three changes are noticed as the Gd^{3+} concentration increases: (1) the $4f^2 5d$ emission decreases, (2) the time integrated emission from the $^6P_{7/2}$ state of Gd^{3+}, seen at 313nm, decreases, and (3) the $^4F_{3/2}$ emission in the IR becomes relatively enhanced. Thus the presence of Gd^{3+} promotes the conversion of energy initially excited to the $4f^2 5d$ configuration into $^4F_{3/2}$ emission. After the initial CRET process B in which the Gd^{3+} ion undergoes a transition first from its ^6G_J to ^6I_J followed by a second CRET C leaving it in $^6P_{7/2}$, efficient energy transfer back to Nd^{3+}, in the step described as ET2 in Fig. 5. 2, occurs more rapidly with an increase in Gd^{3+} concentration. This occurs because the excitation can move more effectively on the Gd^{3+} sublattice, thereby more easily finding a nearest neighbor Nd^{3+} ion with which to transfer its energy. As discussed below, the reason for the decrease in time-integrated ^6P emission with Gd^{3+} concentration is more complicated than might at first appear. CRET with Gd^{3+} provides an additional channel for the population the Nd^{3+} $^4F_{3/2}$ state, in addition to population feeding from relaxation directly within a single Nd^{3+} ion. It should also be recognized that in the more dilute Gd^{3+} samples where $4f^2 5d$ emission is observed, cascade emission can also contribute to the rapid population of $^4F_{3/2}$. All $4f^2 5d$ emission at wavelengths longer than 220nm (see Fig. 5.2) populate either $^4F_{3/2}$ or states above it which relax quickly to $^4F_{3/2}$. Since this process diminishes as the Gd^{3+} concentration is increased, the increase of $^4F_{3/2}$ emission points even more strongly to some additional feeding, which we assign to the CRET with Gd^{3+}.

5.3 Excitation Spectrum

The excitation spectrum, detecting the $^4F_{3/2} \rightarrow {}^4I_{9/2}$ emission of Nd^{3+} at 780–910 nm, is shown in Fig. 5.5 for the 1%, 2% and 3% Nd samples. It contains features associated both with Gd^{3+} and Nd^{3+} as indicated on the figure. One clearly sees the states of the $4f^7$ configuration of Gd^{3+}, namely ^6G_J, ^6D_J and ^6I_J, indicating that energy transfer between Gd^{3+} and Nd^{3+} occurs, as expected. The $4f^25d$ bands of Nd^{3+} are also clearly observed.

The quantum yield relative to that of the reference, sodium salicylate, achieves a maximum of 1.8 in the 2% Nd sample for excitation into the $4f\rightarrow5d$ bands of Nd^{3+} at 175 nm. This value is obtained by applying a number of corrections to the raw data. First, the raw data are corrected for the fact that the relative quantum efficiency of the PMT for the $^4F_{3/2}\rightarrow{}^4I_{9/2}$ emission wavelength of Nd^{3+} between 860 and 910 nm is much less than that at the 380–460 nm emission wavelength range of sodium salicylate. A correction factor for the relative response of the PMT is obtained by convoluting the corrected emission of the sample and sodium salicylate reference, each with the quantum efficiency of the PMT, and calculating the ratio of these products yielding a correction factor of 20±6. A great deal of effort was made to accurately obtain the relative quantum efficiency of the PMT which, because of the rapid decrease in response in the region above 860 nm, leaves this considerable uncertainty of about ±30%. Second, it is estimated that only 33% of the $^4F_{3/2}$ emitted photons occur on the $^4F_{3/2}\rightarrow{}^4I_{9/2}$ transition, based on reported [24] emission spectra of $YLiF_4$: Nd and calculations of the branching ratios determined by a Judd-Ofelt analysis [25], implying a further correction of about 3. An actual measurement of the branching ratios obtained from the IR emission spectrum was performed by Rufus Cone using an Applied Detector Corp. 403L Ge detector at the exit slit of a Spex 1000M spectrometer. All spectra were referenced against a tungsten halogen lamp operating at 2800 K. The measurement yielded a value of 31.1% for the fraction of the emission occurring to $^4I_{9/2}$, very close to the value calculated. The result was a correction factor of 3.22±0.3. Finally, there is an uncertainty concerning the relative reflectivities of the samples and sodium salicylate reference. Although these may be somewhat different, they are probably both less than 20% in the strongly absorbing regions of the spectrum of interest. Thus, this should add not more than a ±10% error. Using an estimate that the absolute quantum yield of sodium salicylate as 0.5 [13], implies an absolute quantum yield for the $^4F_{3/2}$ emission of about 1.05±0.35. The estimated uncertainty is based on the accumulated errors discussed above. This value for the quantum yield is about three times the value of 0.32 [19] obtained for $GdLiF_4$: Eu. However, it is still well below the theoretical maximum quantum yield of 2 based on the quantum splitting scheme described above. This highlights the fact that even in a system that exhibits highly efficient quantum cutting, other losses can limit the absolute quantum yield. Indeed, measurements of the quantum efficiency of the $GdLiF_4$: Eu quantum cutting phosphor [19] show that a broad defect absorption reduces the quantum efficiency considerably. A study of the dynamics will allow for an examination of some of the reasons for the reduced quantum yield for $GdLiF_4$: Nd.

The excitation spectra for detection above and below 780 nm are compared in Fig. 5.6. The spectra are normalized to the Gd^{3+} ^6I transition. Detection for $\lambda > 780$ nm (dotted curve in Fig. 5.6) yields the excitation spectrum of the IR emission from $^4F_{3/2}$ only. The excitation spectrum for $\lambda < 780$ nm (solid curve) is dominated by Nd^{3+} emission from $^4D_{3/2}$ which is not enhanced by the quantum cutting. Both the ^6G excitation features of Gd^{3+} and the $4f^25d$ bands of Nd^{3+} are enhanced when detecting the $^4F_{3/2}$ emission supporting the conclusion that quantum cutting plays an important role in the emission. For detection with $\lambda < 780$ nm, there is evidence for an impurity or defect absorption band near 200 nm.

5.4 Dynamics of quantum cutting

Despite the fact that a great deal of work has been done on quantum cutting due to cross relaxation energy transfer (CRET), there have been, to our knowledge, only two studies [16,17], of the dynamics of this process. The studies considered the Gd^{3+}–Eu^{3+} couple in $GdNaF_4$: Eu^{3+}

and in $GdLiF_4$: Eu^{3+}. Both the cross relaxation and direct transfer were observed with rates about two orders of magnitude slower than for the Gd^{3+}–Nd^{3+} couple studied here. As pointed out in Wegh *et al*. [3], the process achieves its efficiency because of energy migration among the Gd^{3+} ions which are stoichiometric in all known successful cross relaxation energy transfer quantum splitters. Dipole-dipole energy transfer or exchange is just too slow except for ions that are near neighbors. The fact that energy migrates within the Gd^{3+} ions ensures that the excitation in the ^6G_J levels of Gd^{3+} gets to spend a portion of its time as a near neighbor of Nd^{3+}. Thus the dynamics within the Gd^{3+} system is expected to play an important role in the process.

When a sample of $GdLiF_4$ containing 2% Nd^{3+} is excited at 157 nm with a molecular F_2 laser, one sees a buildup of the $^6P_{7/2}$ transition of Gd^{3+} at 313 nm as shown in Fig. 5.7 by the dark solid curve. This buildup has two components. One is very fast, at a rate which exceeds the time resolution of these experiments (<50ns, limited by some background scattered light from the laser discharge and defect luminescence), which represents about 20% of the population feeding. The second is a slower buildup over several microseconds, representing about 80% of the feeding. The cause of these two components becomes clear from the dynamics of the ^6I emission of Gd^{3+} at 281 nm, also shown in Fig. 5.7. Its decay rate coincides with the slower $^6P_{7/2}$ population buildup rate. Also shown in Fig. 5.7 is the dynamics of the emission at 866 nm from the $^4F_{3/2}$ state of Nd^{3+} which also builds up within the temporal resolution of the experiment. Thus we conclude, as suggested based on an earlier discussion of the reduced matrix elements, that cross relaxation process B from Fig. 5.2 is the dominant one in the quantum cutting. However, the fact that the $^6P_{7/2}$ population does have a very fast component indicates that there may also be a contribution from the cross relaxation energy transfer process labeled as A in Fig. 5.2. The relaxation of Gd^{3+} from ^6I to ^6P in a few microseconds is unlikely to occur due to multiphonon relaxation because of the large energy gap (~3000 cm^{-1}) and low phonon energies of the $GdLiF_4$ host, but rather most likely occurs through the cross relaxation energy transfer process labeled C in Fig. 5.2. Consistent with this suggestion is the fact that the relaxation is dependent on Nd^{3+} concentration as discussed below. In this process a Nd^{3+} ion is excited from the $^4I_{9/2}$ ground manifold to $^4I_{13/2}$, for which there is a good resonance match with the $^6I \rightarrow {}^6P$ transitions on Gd^{3+}.

The behavior of the dynamics of process C and its concentration dependence provides important information on the role of donor-donor energy transfer among the Gd^{3+} ions. The dynamics of the ^6I and ^6P emissions are shown as a function of concentration in Fig. 5.8. The relaxation process is nearly exponential as seen by the dashed lines plotted over the ^6I time-resolved emission which are fits to the data assuming an exponential decay of ^6I. The values for the fit are shown on the figure and are summarized in Table 1. The relaxation rate scales nearly linearly with concentration as expected. Also shown are the dynamics of the $^6P_{7/2}$ emission along with fits to the data using the ^6I decay time as the feeding term in the $^6P_{7/2}$ population. Indeed, the same times describe both the ^6I and $^6P_{7/2}$ emissions. The decay of $^6P_{7/2}$ is also nearly exponential with a rate that depends on Nd^{3+} concentration. These rates are also summarized in Table 1. The nearly exponential relaxation processes for all three concentrations suggests that energy migration among the Gd^{3+} ions is fast compared to these CRET relaxation rates. In that case the Gd^{3+} excitation samples all sites thereby spending a fraction of its time nearby a Nd^{3+} ion with which it can under CRET. If, after energy transfer from the $4f^25d$ state of Nd^{3+} to Gd^{3+}, the energy remained localized on that Gd^{3+} ion, the CRET rates would be highly non-exponential. In addition, without energy migration, CRET process C would be hindered as all of the energy resonances that we have discussed assume that the Nd^{3+} ions are in their ground state. However, processes A and B leave the Nd^{3+} ion in an excited state for a time roughly equal to the lifetime of the $^4F_{3/2}$ state of about 400 μs. Also, in the absence of rapid Gd^{3+}-Gd^{3+} energy transfer, some of the possible processes providing the initial $Nd^{3+} \rightarrow Gd^{3+}$ energy transfer could also leave Nd^{3+} in an excited state, as discussed earlier, compromising the CRET processes A and B which also assume that the Nd^{3+} ions are in their ground states.

The excited Gd^{3+} ions in the $^6P_{7/2}$ state then undergo energy transfer to the nearly resonant $4f^3$ states of Nd^{3+} at a rate described by the decay of the Gd^{3+} $^6P_{7/2}$ emission. Proof of this second step is seen by monitoring the $^4D_{3/2}$ emission under 157 nm excitation, also shown in Fig. 5.7. It is observed that this emission closely follows the Gd^{3+} $^6P_{7/2}$ population with a small delay and that it has zero population immediately after the laser excitation. This occurs because the intrinsic $^4D_{3/2}$ lifetime is much shorter than the $^6P_{7/2}$ lifetime (~1 μs due to multiphonon relaxation to $^2P_{3/2}$), as seen from its decay under direct 355 nm excitation into the $4f^3$ states just above $^4D_{3/2}$, as shown in Fig. 5.9. The fact that the $^4D_{3/2}$ population closely follows the excited Gd^{3+} population demonstrates that energy transfer from Gd^{3+} to Nd^{3+} does occur, a process which is necessary for the second step of the quantum cutting process. The observation that the $^4D_{3/2}$ emission (spectrally integrated) is more than an order of magnitude greater than the Gd^{3+} $^6P_{7/2}$ emission (see Fig. 5.1) in $GdLiF_4$: Nd indicates that a significant fraction of the Gd^{3+} ions transfer their energy to Nd^{3+} since the two populations follow one another because of the short inherent lifetime of $^4D_{3/2}$. Its greater time integrated intensity results from its faster radiative rate than that of $^6P_{7/2}$ which is spin forbidden. Since we do not know the relative radiative rates, it is not possible to estimate from these relative intensities the efficiency of this $Gd^{3+} \rightarrow Nd^{3+}$ energy transfer.

The $^4D_{3/2}$ state decays non-radiatively to $^2P_{3/2}$ whose population dynamics is also shown in Fig. 5.9 for both 355 nm and 157 nm excitation. Under 355 nm excitation, $^2P_{3/2}$ builds up at the $^4D_{3/2}$ decay rate and decays in 20 μs, its intrinsic non-radiative lifetime. Under 157 nm excitation it has a slower buildup resulting from the population feeding from $^4D_{3/2}$ whose population is controlled by energy transfer from $^6P_{7/2}$ of Gd^{3+}. The $^2P_{3/2}$ decay ultimately feeds $^4F_{3/2}$ through multiphonon relaxation down the ladder of states of Nd^{3+} from whose radiative decay provides the second photon in the quantum cutting arises. Thus the feeding of $^4F_{3/2}$ for the second step in the quantum cutting continues for ~100 μs.

The temporal behavior of the $^4F_{3/2}$ emission further supports the presence of quantum cutting. As shown in Fig. 5.10, when the $4f^3$ Nd^{3+}states just above $^4D_{3/2}$ are excited directly at 355 nm, such that there is no quantum splitting, the $^4F_{3/2}$ emission builds up with a rise time that is close to the value of the decay time of the $^2P_{3/2}$ Nd^{3+} emission (20 μs), also shown. The $^4F_{3/2}$ emission under 157 nm excitation, which is the solid line in Fig. 5.10, shows a much more rapid buildup as expected due to the first step in the quantum cutting, namely the cross relaxation step. However, note that the $^4F_{3/2}$ emission does not immediately begin an exponential decay. Rather its population remains high due to feeding from the second step in the quantum cutting which maintains a feeding term for about ~100 μs as $^2P_{3/2}$ decays.

Attempts to fit the dynamics presented in Fig. 5.10 (dotted curves) with an exponential rise and decay indicate that, under 355 nm excitation, the $^4F_{3/2}$ emission has both a fast (immediate with respect to the experimental time resolution) followed by an exponential rise with a 12 μs rise time. The latter represents only 33% of the total contribution to the feeding of the $^4F_{3/2}$ population. The source of the fast component is unknown but it suggests the existence of some other channel of relaxation for 355 nm excitation. Under 157 nm excitation there is again a fast component, resulting from the first CRET step due to processes A and B, followed by an additional feeding through $^2P_{3/2}$ for about 100 μs (see Fig. 5.9). Here the additional feeding contributes only 9% to the $^4F_{3/2}$ population. Under ideal conditions of quantum cutting, this should represent 50% of the contribution to the $^4F_{3/2}$ population through the process labeled ET 2 in Fig. 5.2. Because of the observation that even under 355 nm excitation there exists an unexplained very fast component to the $^4F_{3/2}$ population, it may be that a somewhat lower value than 50% should be expected. However, the fact that it is only 9% seems to explain, in part, the less than ideal quantum yield of 2.

There are a number of potential sources for this reduced contribution including radiative transitions from $^4D_{3/2}$ and $^2P_{3/2}$ that are observed in Fig. 5.1, radiative transitions from $^6P_{7/2}$ of Gd^{3+} prior to energy transfer to Nd^{3+}, transfer of energy from $^6P_{7/2}$ of Gd^{3+} to impurities or defects, and cross relaxation among Nd^{3+} ions. In addition, non-radiative processes involving $^4F_{3/2}$ are possible. Indeed, the observed lifetimes of the $^4F_{3/2}$ emission are below the low concentration limit of 535 μs in $GdLiF_4$: Nd [24], and, in agreement with the results of Zhang et al. [25] the 2% and 3% samples exhibit significant non-exponential behavior indicative of Nd^{3+}-Nd^{3+} cross relaxation (not shown). However, while this would contribute to the reduced quantum yield in the second step of the quantum cutting, it would not explain the lower than expected contribution to the feeding of $^4F_{3/2}$.

When the $4f^25d$ configuration of Nd^{3+} in $YLiF_4$: Nd is excited, strong parity allowed emission is observed in the VUV and UV [21]. This $4f^25d$ emission, excited at 157 nm with a molecular F_2 laser, is also observed in $Gd_xY_{1-x}F_4$: Nd for $x < 0.5$ as shown in Fig. 5.11. However, as the Gd^{3+} concentration is increased, the 5d emission rapidly decreases. No 5d emission is observed in pure $GdLiF_4$: Nd. The intensity as a function of concentration is compared with the probability of finding a Nd^{3+} ion with no Gd^{3+} ions in the nearest neighbor (NN) position in the inset of Fig. 5.11 (solid curve). In $GdLiF_4$ the Nd substitutes for Gd. Each Gd has four equivalent NNs at a distance of 3.73 Å. The next NNs consist of four equivalent ions at 5.17 Å. The probability of finding a Nd^{3+} ion with only Y^{3+} ions is $(1-x)^4$. A comparison of the concentration dependence of the ratio of 5d emission intensity, with this probability shows that it roughly follows this probability for each of the three main bands of Fig. 5. 11. This suggests that the energy transfer occurs effectively to Gd^{3+} ions in the NN position, but not efficiently to the next NNs. The radiative lifetime of the $4f^25d$ state of Nd^{3+} in $YLiF_4$ is 35 ns [27]. Thus NN energy transfer occurs at a rate > 10^8 s^{-1} whereas the rate of transfer to the second NNs is much slower. These results indicate that Nd^{3+} does effectively sensitize Gd^{3+} when excited in the VUV.

The dynamics provide a great insight into the mechanism for the CRET. Plotted in Fig. 5.12, are the dynamics of the $^6P_{7/2}$ emission of Gd^{3+} in the samples with different Gd^{3+} concentrations at a constant 1% concentration of Nd^{3+}. The data are plotted as a log − log plot to allow the presentation of data over a wide range in both time and intensity. The data for each concentration were obtained by combining the results obtained with different time scales and different input impedances on the digital oscilloscope in order to cover the large time scales while still providing adequate resolution at early times. All samples with x >0.5 show nearly identical behavior. The dynamics for these high Gd^{3+} concentrations show (1) a very fast (<20 ns) rise in population, (2) a fast but slower additional rise during the first 10 μs, and (3) then a nearly exponential decay with decay time of about 100 μs. The population buildup is much faster than would be expected from non-radiative decay from the high-lying levels of Gd^{3+} based on multi-phonon emission. We attribute it to CRET processes with Nd^{3+}. For x >0.5 energy transfer to Gd^{3+} occurs rapidly as evidenced by the absence of $4f^25d$ emission from Nd^{3+}. As described above, spectral overlap favors transfer to the states of Gd^{3+} resonant with the $4f^25d$ states of Nd^{3+} followed by multi-phonon relaxation to the metastable ^6G_J levels. Based on previous work in x = 1 samples, the fast rise involves a CRET labeled A in Fig. 5.2, while the slower component of the rise in $^6P_{7/2}$ population results from feeding from ^6I according to a sequential energy transfer involving CRET processes B and C in Fig. 5.2. As shown by Wegh *et al.*, process B actually has the larger Gd^{3+} transition dipole reduced matrix elements.

For the mixed crystal system $Gd_xY_{1-x}LiF_4$: Nd, the dynamics for the samples with x <0.5 are quite different as also seen in Fig. 5.12. For the x = 0.1 sample, the $^6P_{7/2}$ population exhibits two distinct regimes. In the first temporal regime, one sees that, as for the samples with high concentrations, there exist a (1) fast (<30 ns) and (2) slower (~2 μs) rise, followed by (3) a decay (~10 μs). The dynamics in this first regime occur considerably faster than that of the high Gd^{3+} content samples. In the second temporal regime the $^6P_{7/2}$ population slowly builds up (~1 ms) again before decaying (~10 ms). The decay rate in this second regime is very close to that observed for a sample with 2% Gd^{3+} and no Nd^{3+}. This striking and unusual behavior points to the existence of two very different classes of Gd^{3+}–Nd^{3+} arrangements. Those responsible for the dynamics exhibited in the first time regime probably involve Nd^{3+} ions with at least one Gd^{3+} ion in a NN position to which it couples strongly. For x = 0.1, this represents about 38% of the Nd^{3+} ions. The ions responsible for the dynamics in the second temporal regime must be Gd^{3+} ions which couple very weakly with the Nd^{3+} ions since their decay from the $^6P_{7/2}$ level is nearly identical to that of isolated Gd^{3+} ions. Their population buildup would then result from relaxation from the higher lying states of Gd^{3+}. It is likely that they are excited by a direct excitation of Gd^{3+} to the states of the $4f^7$ configuration at the 157 nm laser excitation wavelength. Note that the peak emission intensity is only about 5% that of the first group of ions as a result of their much weaker parity forbidden absorption.

The sample with x = 0.25 exhibits a dynamical behavior similar to that of the x = 0.1 sample except that a minimum in the emission rate is not observed. This can be understood by the fact that the increased Gd^{3+} content makes direct excitation 2.5 times more probable, representing a higher fraction of the Gd^{3+}. Although the percentage of Nd^{3+} ions with at least one nearest neighbor Gd^{3+} ion also increases to about 70%, the dynamics of the first regime is slower, causing the two regimes to merge so that a minimum in the population is not observed. Nonetheless, two regimes are still clearly discernible.

5.5 Discussion

It is of interest to examine the mechanisms for the cross relaxation energy transfer (CRET) responsible for the quantum cutting. For closely spaced ion pairs, this may occur by dipole-dipole interactions or exchange interactions [4]. For more distant pairs, the exchange will become unimportant because of its rapid decrease with distance. As we discussed in Chapter 2, according to Förster-Dexter dipole-dipole energy transfer theory, the transfer rate, P_{DA}^{dd} can be written [11] as

$$P_{DA}^{dd} = 1.4\times10^{24} f_D f_A S \Delta E^{-2} R^{-6} \tag{5.1}$$

Here f_D and f_A, are the oscillator strengths of the transitions on Nd^{3+} and Gd^{3+}, ΔE is the transition energy of each ion (in eV), R is the distance between the two ions (in Angstroms), and, S is the spectral overlap (in cm^{-1}) of the downward and upward transitions. In Fig. 5.3, it was shown for CRET process A that there are many ${}^4I_{9/2} \rightarrow {}^4G_{5/2}$ transitions of Nd^{3+} that are nearly resonant with the ${}^6G_J \rightarrow {}^6P_J$ transitions of Gd^{3+}. The oscillator strength of each of these crystal field transitions of Nd^{3+} in $YLiF_4$ are typically about $\sim 5\times10^{-7}$ based on spectral analysis of some of the individual crystal field transitions at 20K. However, one can also estimate the oscillator strengths from experimental and calculated values integrated over all transitions in the manifolds by dividing by the number of final states which yields about the same average oscillator strength per crystal field transition [28]. A similar situation holds for process B which involves the ${}^6G_J \rightarrow {}^6I_J$ involves transitions of Gd^{3+} and the ${}^4I_{9/2} \rightarrow {}^4F_{5/2}$, ${}^2H_{9/2}$ or ${}^4F_{7/2}$ transitions of Nd^{3+}. These Nd^{3+} transitions also have oscillator strengths of about 5×10^{-7}.

The oscillator strengths of the transitions within the ${}^6G_{7/2} \rightarrow {}^6P_J$ or the ${}^6G_{7/2} \rightarrow {}^6I_J$ manifolds of Gd^{3+} have not been measured but their reduced matrix elements have been calculated. The reduced matrix elements for the ${}^6G_{7/2} \rightarrow {}^6I_J$ transitions are almost a factor of 10 greater than those of the ${}^6G_{7/2} \rightarrow {}^6P_J$ transitions, yielding the expectation that under similar resonance conditions, the oscillator strengths for process B should be one to two orders of magnitude greater than for process A. As described earlier, a factor of 5 was observed. The difference may be due to the quality of the energy resonance for the two processes. These oscillator strengths can be calculated based on the reduced matrix elements. The total oscillator strength to all transitions ${}^6G_{7/2} \rightarrow {}^6I$ is 2×10^{-6} and for ${}^6G_{7/2} \rightarrow {}^6P_{7/2}$ it is 1.5×10^{-8}. Since there are 78 final states in ${}^6I$, each crystal field transition, on average, has an oscillator strength of ~ 3×10^{-8}.

It is now possible to estimate the CRET transfer rates for dipole-dipole interactions in process A from Eq. (5.1). Using typical values of 3×10^{-7} for each transition of Nd^{3+} and 3×10^{-8} for each transition of Gd^{3+} and assuming a single perfect energy resonance with a linewidth at room temperature of 10 cm^{-1} (spectral overlap integral =0.1). One finds a rate of ~ 2×10^5 s^{-1} for a nearest neighbor pair separated by 3.73 Å. This rate falls to ~ 3×10^4 s^{-1} for a next nearest neighbor pair separated by 5.15 Å. To predict what should be observed one has to know whether the donor-donor transfer among the Gd^{3+} ions is occurring and whether it is faster than the donor-acceptor CRET rates. The results from the dynamics of process C involving a CRET from ${}^6I$ to ${}^6P$ suggest, based on the nearly exponential decay of ${}^6I$ and rise of the ${}^6P_{7/2}$ population, that the donor-donor transfer occurs much more rapidly than the observed CRET rate of ~ 6×10^5 s^{-1} in the 2% Nd sample. If one assumes that the same is true for process A where the CRET rates are $>2\times10^7$ s^{-1}, then the predicted rates should take into account the fact that, on average, the excited Gd^{3+} excitation spends a fraction, 4x, (x is the fractional concentration of Nd^{3+}) of its time as one of the four nearest neighbors of Nd^{3+}. Thus for 2% Nd the nearest neighbor rate should be multiplied by a factor of 0.08 yielding a result of ~ 1.6×10^4 s^{-1}. This rate is obtained for one resonance between the Gd^{3+} ${}^6G_{7/2}\rightarrow{}^6I$ and the ${}^4I_{9/2}\rightarrow{}^4F_{5/2}$, ${}^2H_{9/2}$ or ${}^4F_{7/2}$ transitions of Nd^{3+}. Even if one were to assume that all Nd^{3+} transitions were perfectly resonant with a transition on Gd^{3+}, which would be an extreme assumption, and if contributions from more distant pairs are added, the maximum predicted rate still would be less than 10^6 s^{-1}.

The assumption of rapid energy transfer among the Gd^{3+} donors is supported by studies of Gd^{3+}-Gd^{3+} interactions. Studies of band-to-band exciton transitions in $GdCl_3$, $Gd(OH)_3$, and $Tb(OH)_3$ have shown that exchange interactions among nearest neighbor ions can yield resonant energy transfer rates among nearest neighbors that are as large as 10^{10} to 10^{11} s^{-1} for resonant energy transfer among Gd^{3+} ions in their ${}^6P_{7/2}$ state or Tb^{3+} ions in their ${}^5D_4$ state [29]. These rates correspond to the condition of resonance with homogeneous linewidths at 1.5 K of about 0.1 cm^{-1}. At room temperature, where these linewidths are ~10 cm^{-1}, corresponding rates would be 10^8 to 10^9 s^{-1}. Even though the exchange interaction will probably be considerably smaller in fluorides, the expectation that donor-donor transfer rates for the ${}^6G$ states of Gd^{3+} should exceed 2×10^7 s^{-1} in $GdLiF_4$ seems quite reasonable.

In the limit of no energy transfer among the Gd^{3+} ions then the relaxation after the initial energy transfer from $Nd^{3+} \rightarrow Gd^{3+}$ would occur by interactions between a pair of nearest neighbors. This rate would have a maximum value of ~ 5×10^{6} s^{-1} if all transitions of the two ions were resonant. Even this extreme assumption falls well short of explaining the observed rate of $>2\times10^{7}$ s^{-1} and the absence of fast donor-donor transfer seems unlikely. Thus the above analysis of the experiments point strongly to the dominant role of exchange interactions in facilitating the CRET responsible for quantum cutting in $GdLiF_4$: Nd.

It would be interesting to model the full dynamics, taking into account the energy migration of the Gd^{3+} excitations in both the ${}^6G_{7/2}$ and ${}^6P_{7/2}$ states. Although this problem is a very interesting one, it is not the subject of this dissertation.

5.6 Conclusions

Efficient quantum splitting has been demonstrated for the Gd^{3+}-Nd^{3+} system in $GdLiF_4$: Nd 2%. A VUV photon is absorbed by the Nd^{3+} ions whereupon the energy is rapidly transferred to the high-lying excited states of the $4f^7$ configuration of Gd^{3+} in a time scale of nanoseconds. A rapid and effective cross relaxation energy transfer then occurs in two steps. In the first, a Gd^{3+} ion in its metastable ${}^6G$ state undergoes a transition to ${}^6I$ while a Nd^{3+} ions makes a transition ${}^4I_{9/2} \rightarrow {}^4F_{5/2}$, ${}^2H_{9/2}$ or ${}^4F_{7/2}$ at a rate $>2\times10^{7}$ s^{-1}. Multiphonon relaxation effectively brings the Nd^{3+} ions down to the ${}^4F_{3/2}$ state where they radiate the first photon. For the remaining excited Gd^{3+} ion, there occurs a second cross relaxation energy transfer in which Gd^{3+} undergoes a transition ${}^6I \rightarrow {}^6P$ and Nd^{3+} is excited from ${}^4I_{9/2} \rightarrow {}^4I_{13/2}$. The resulting ${}^6P_{7/2}$ excitation on Gd^{3+} transfers its energy to nearly resonant states of the $4f^3$ configuration of Nd^{3+} in a time scale of about 10-20 μs whereby subsequent relaxation brings the population down to ${}^4F_{3/2}$ of Nd^{3+} where the second photon is emitted. This second step appears to be less efficient than the first. The result is a quantum yield for the emission of IR photons which has its maximum of about 1±0.5, under 160 nm excitation. This is considerably below the theoretical value of 2. Nonetheless, this system exhibits the highest quantum yield for quantum cutting based on cross relaxation energy transfer and provides excellent insights into the quantum cutting process, especially with regard to an evaluation of the details of the dynamics and the mechanisms of quantum cutting. An analysis of the dynamics and the theoretical limits of the dipole-dipole contributions, leads to the conclusions that (1) there is rapid donor-donor energy migration among the Gd^{3+} ions and (2) that exchange plays the dominant role in the cross relaxation energy transfer responsible for the quantum cutting.

For mixed crystals of $Gd_xY_{1-x}LiF_4$ containing 2% Nd^{3+}, as x increases, under excitation at 160 nm to the strongly absorbing $4f^25d$ state of Nd^{3+}, the direct emission from the $4f^25d$ state of Nd^{3+} is reduced such that its intensity is in approximate proportion to the fraction of Nd^{3+} ions that have no Gd^{3+} ions in any of the four nearest neighbor positions. For $x \geq 0.75$, no $4f^25d$ emission is observed. In addition, Gd^{3+} $^6P_{7/2}$ emission is observed for all $x \geq 0.1$ indicating that rapid energy transfer from Nd^{3+} to Gd^{3+} occurs for at least some of the Nd^{3+} ions. The emission spectrum shows an increase in the relative intensity of the $^4F_{3/2}$ emission as x increases providing evidence for the presence of quantum cutting. The dynamics of the $^6P_{7/2}$ emission from Gd^{3+} can be understood by considering two different types of nearest neighbor arrangements. Gd^{3+} ions with no Nd^{3+} ions in any of the four nearest neighbor positions and those, which do have a nearest neighbor Nd^{3+} ion. Those Gd^{3+} ions which are members of closely coupled pairs receive energy from the initially excited Nd^{3+} ions with which they then undergo cross relaxation energy transfer leaving both Nd^{3+} and Gd^{3+} ions in their excited states. The excited Nd^{3+} then emits a photon, returning to its ground state whereupon the excited Gd^{3+} can transfer energy back to

Nd^{3+}, which emits a second photon. The very large difference in the CRET rates between the closely coupled ions and ions which are a part of more distant pairs suggests that the exchange interaction is the dominant mechanism for the CRET process and that this completely dominates the CRET of the concentrated x =1 $GdLiF_4$: Nd samples. The dipole–dipole energy transfer mechanism would not be capable of explaining such a strong distinction in the rates. The fact that the dynamics of the Gd^{3+} ions which are members of closely coupled pairs with Nd^{3+} is faster for the samples with lower Gd^{3+} concentrations suggests that energy migration among the Gd^{3+} ions plays an important role in the dynamics. In the systems with x = 0.1 and 0.25, after the initial transfer from Nd^{3+} to Gd^{3+}, the energy remains localized on the pair whereas in the more concentrated samples, the energy migrates rapidly among the Gd^{3+} ions, spending only a fraction of the time on a Gd^{3+} ion which is a nearest neighbor to Nd^{3+}.

Process	**Nd^{3+} conc.**	**Gd^{3+}**	**Nd^{3+}**	**Expt ET rate(s^{-1})**
CRET A	All	$^6G \rightarrow ^6P$	$^4I_{9/2} \rightarrow ^4G_{5/2}$	$>2\times10^7$
CRET B	All	$^6G \rightarrow ^6I$	$^4I_{9/2} \rightarrow ^4F_{5/2}, ^2H_{9/2}$	$>2\times10^7$
CRET C		$^6I \rightarrow ^6P$	$^4I_{9/2} \rightarrow ^4I_{13/2}$	
	1%			3.8×10^5
	2%			5.7×10^5
	3%			8.0×10^5
$Gd^{3+} \rightarrow Nd^{3+}$		$^6P_{7/2} \rightarrow ^8S_{7/2}$	$^4I_{9/2} \rightarrow ^2L_{17/2}$	
	1%			4.3×10^4
	2%			6.7×10^4
	3%			9.1×10^4

Table 1 Experimental energy transfer rates

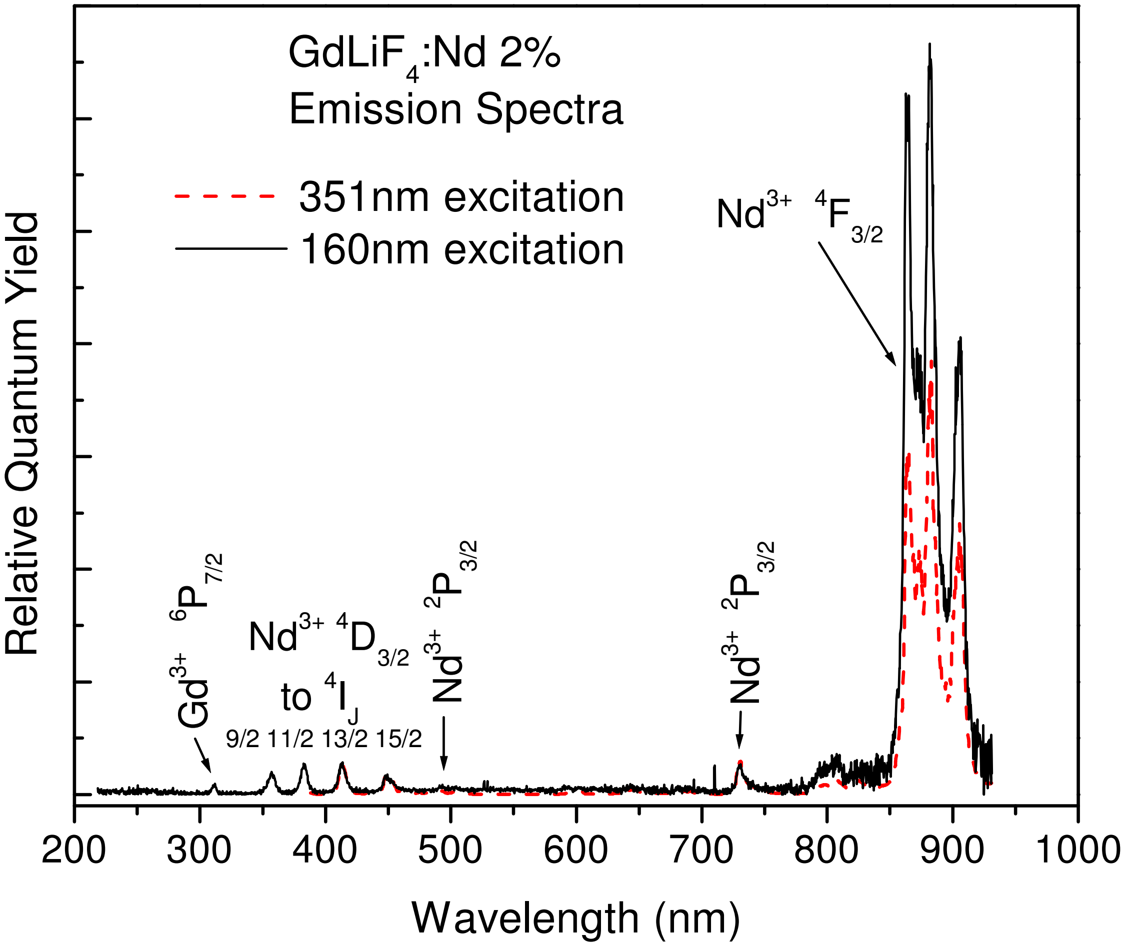

Fig. 5.1 Emission spectra of GdLiF$_4$:Nd 2% exciting at 160 nm and at 351 nm

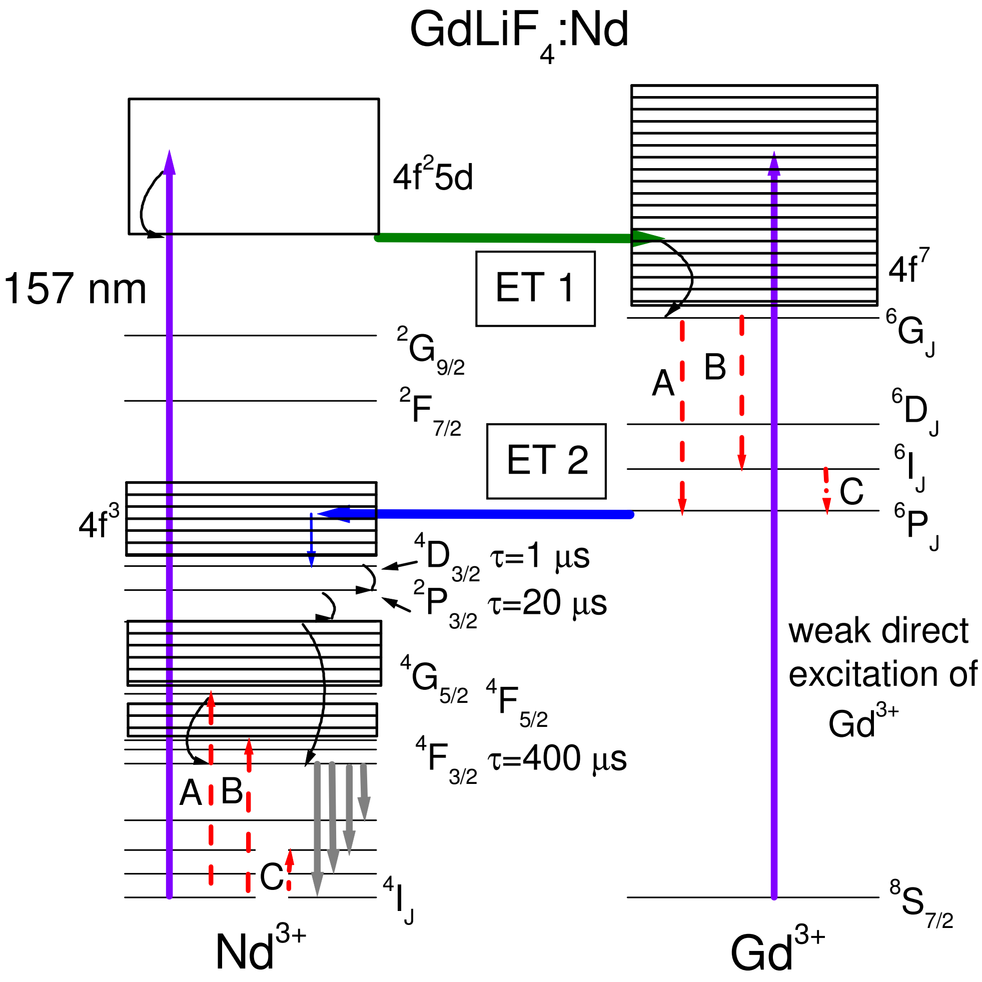

Fig. 5.2 Energy level diagrams of Nd^{3+} and Gd^{3+} in $GdLiF_4$:Nd

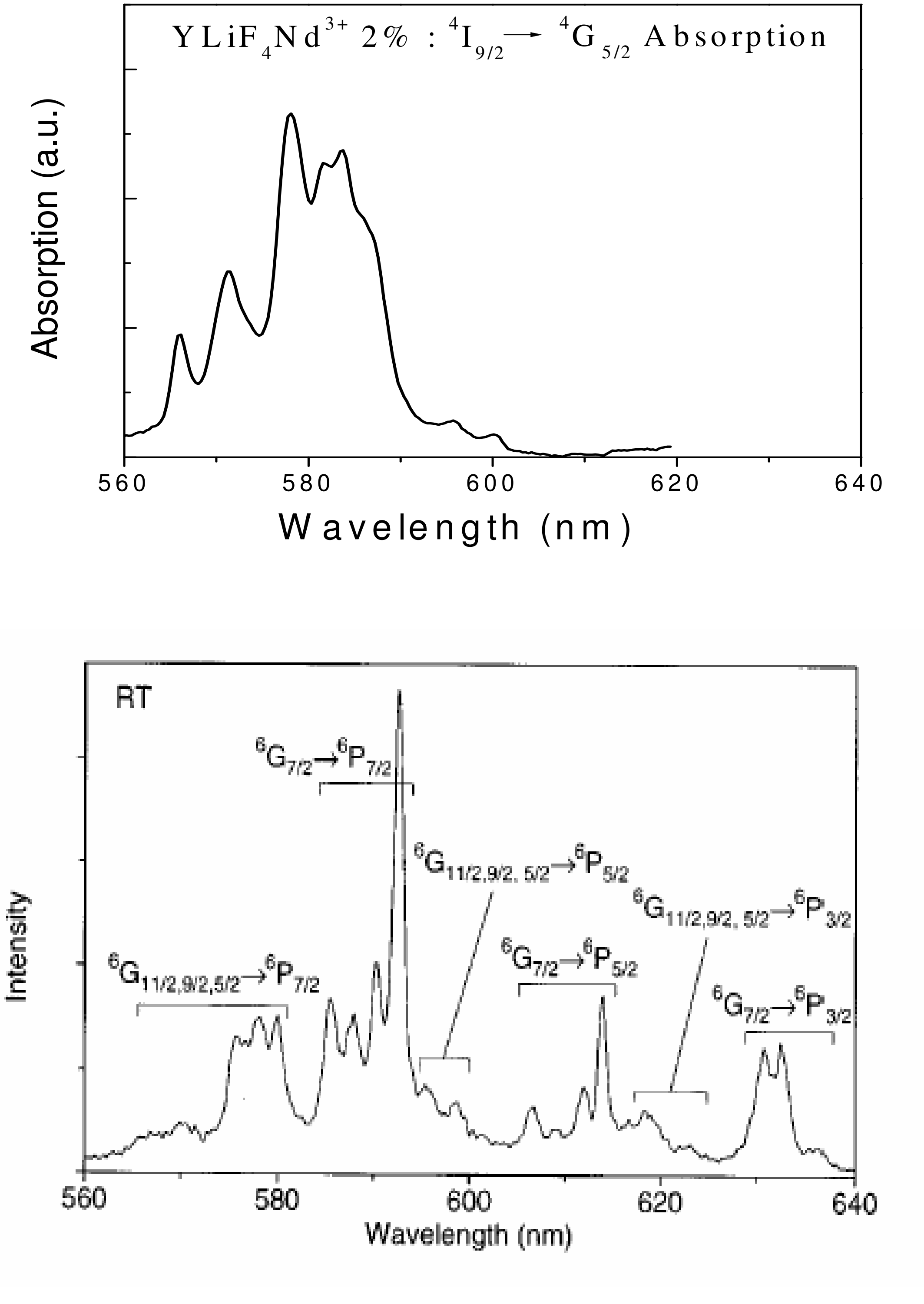

Fig. 5.3 Absorption spectrum of $YLiF_4$:Nd2% and emission spectrum of $YLiF_4$:Gd5%

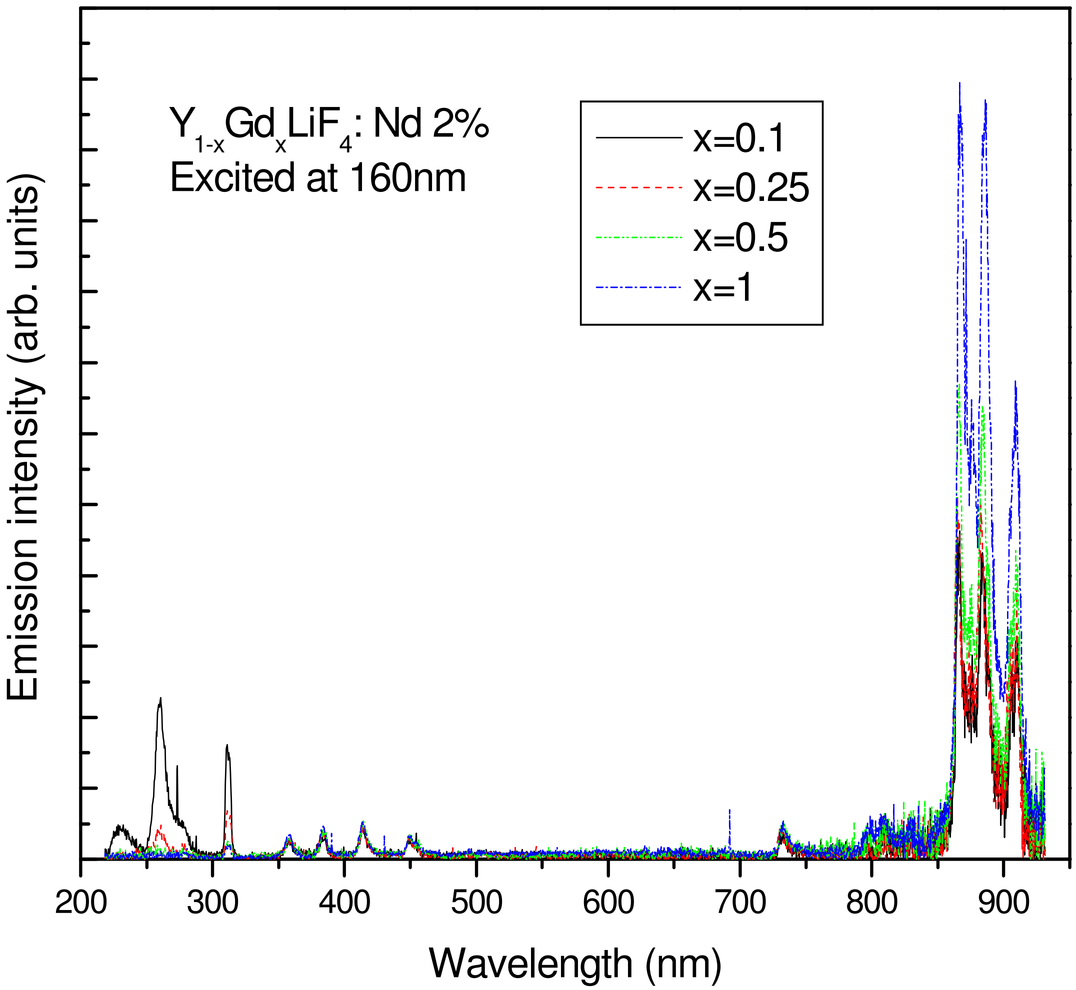

Fig. 5.4 Emission spectra excited at 160nm of four $Gd_xY_{1-x}LiF4$: Nd2% samples

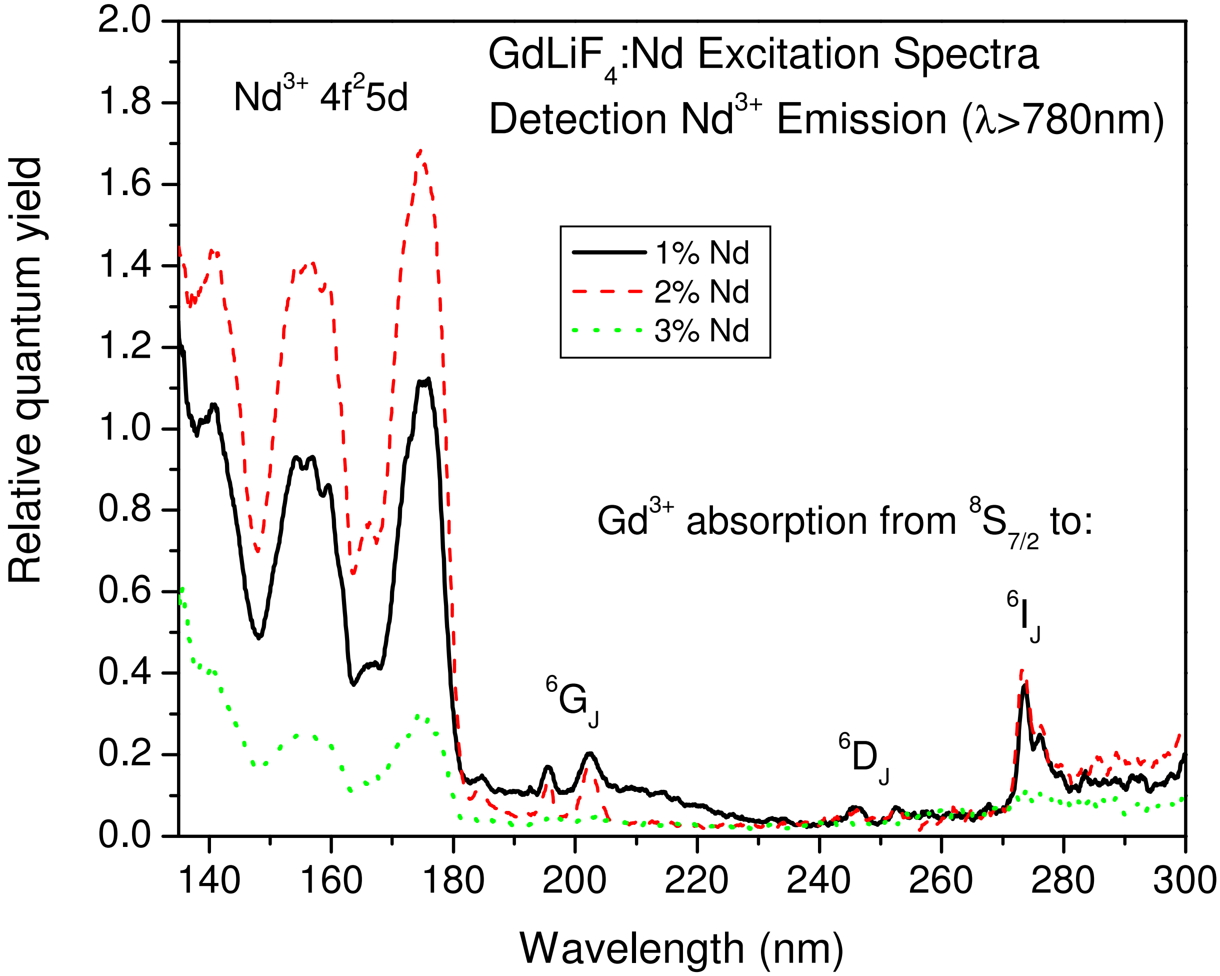

Fig. 5.5 Excitation spectrum of GdLiF$_4$ containing 1, 2 and 3%

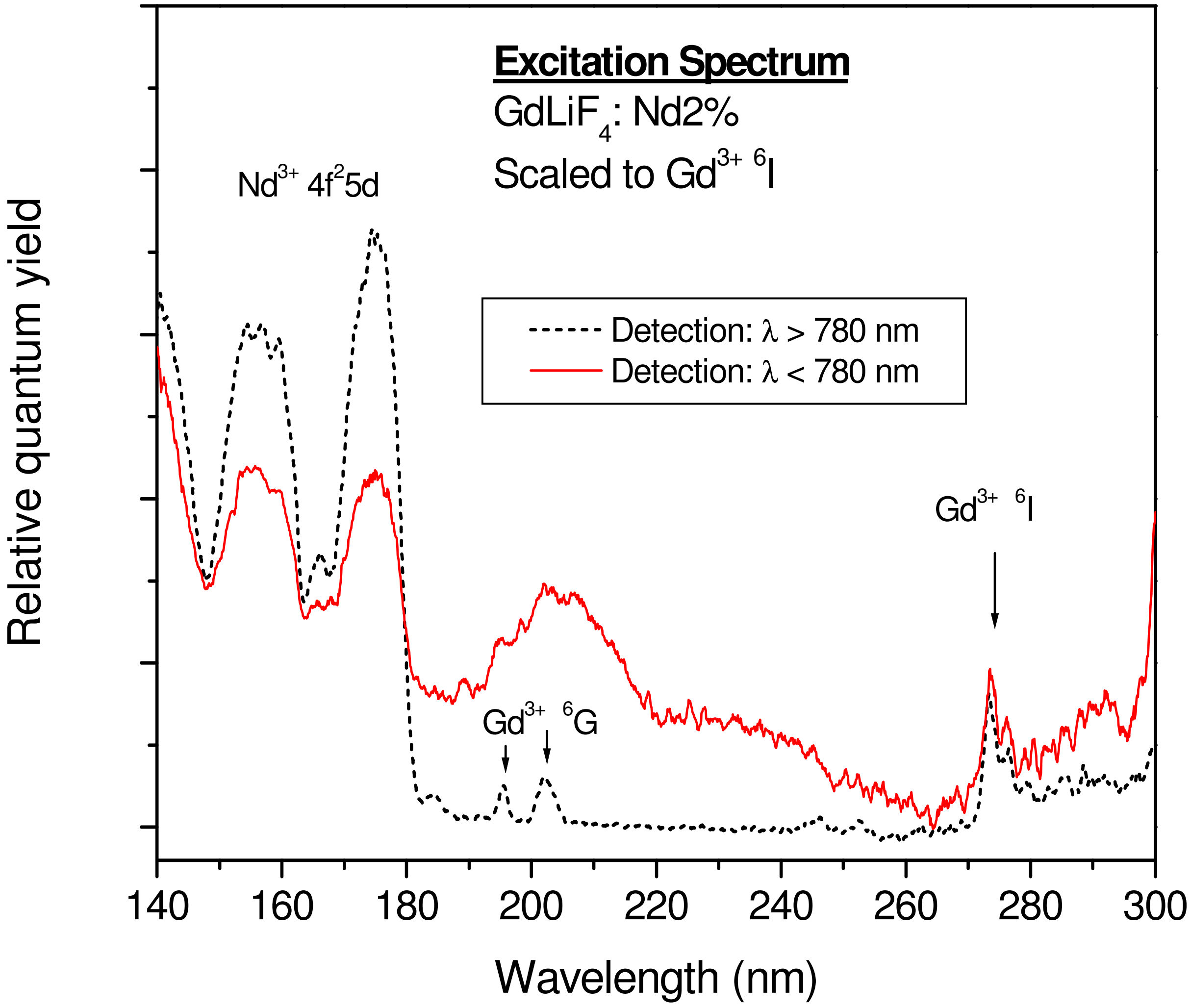

Fig. 5.6 Comparison of the excitation spectra of $GdLiF_4$:Nd2%

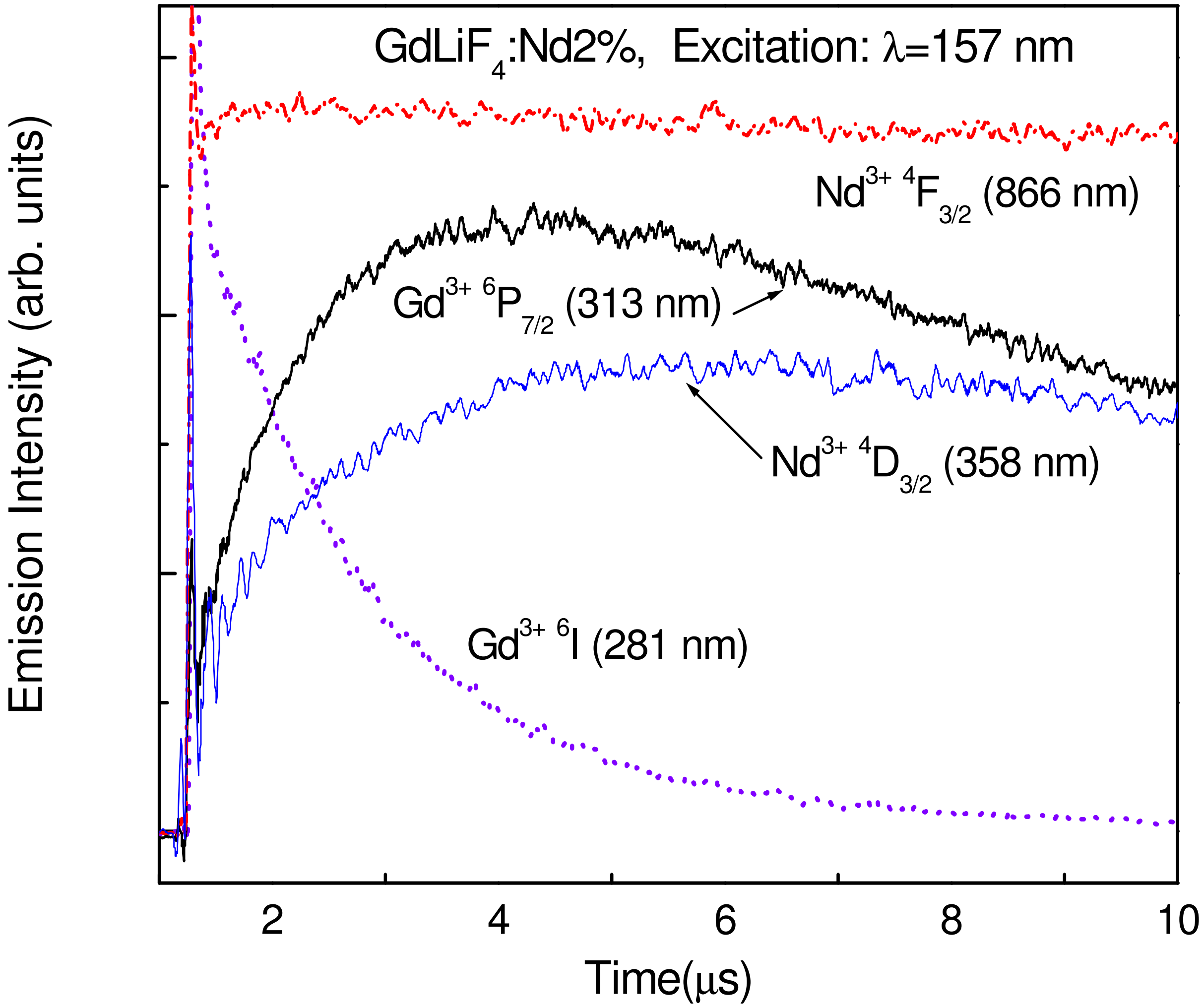

Fig. 5.7 Time evolution of the ^6I (281 nm) and $^6P_{7/2}$ (313 nm) emission intensities of Gd^{3+} and the $^4D_{3/2}$ and $^4F_{3/2}$ emission intensities of Nd^{3+}

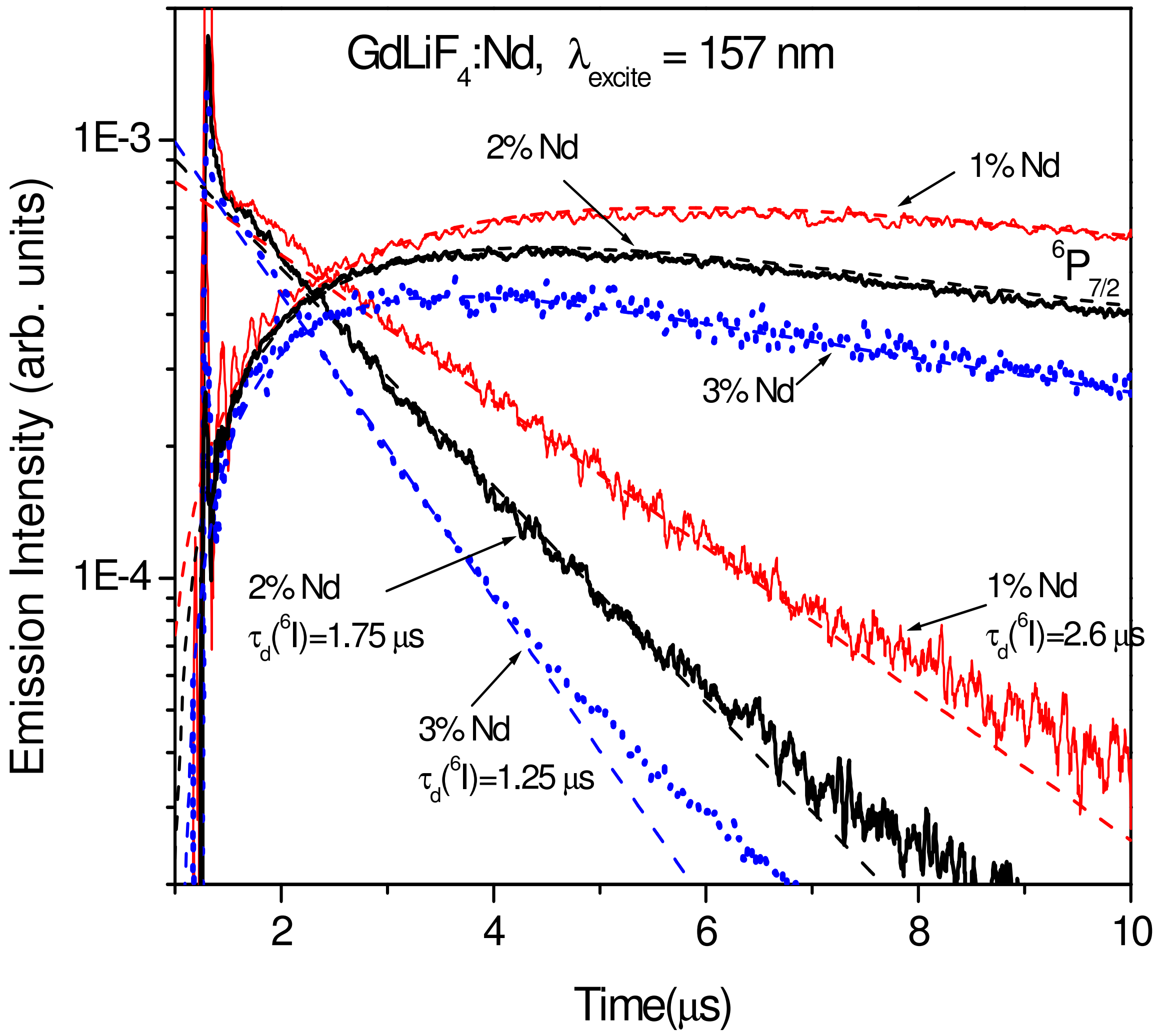

Fig. 5.8 Time evolution of the ^6I (281 nm) and $^6P_{7/2}$ (313 nm) emission intensities of Gd^{3+} under 157 nm pulsed excitation in GdLiF$_4$:Nd for 1, 2, and 3% Nd concentrations.

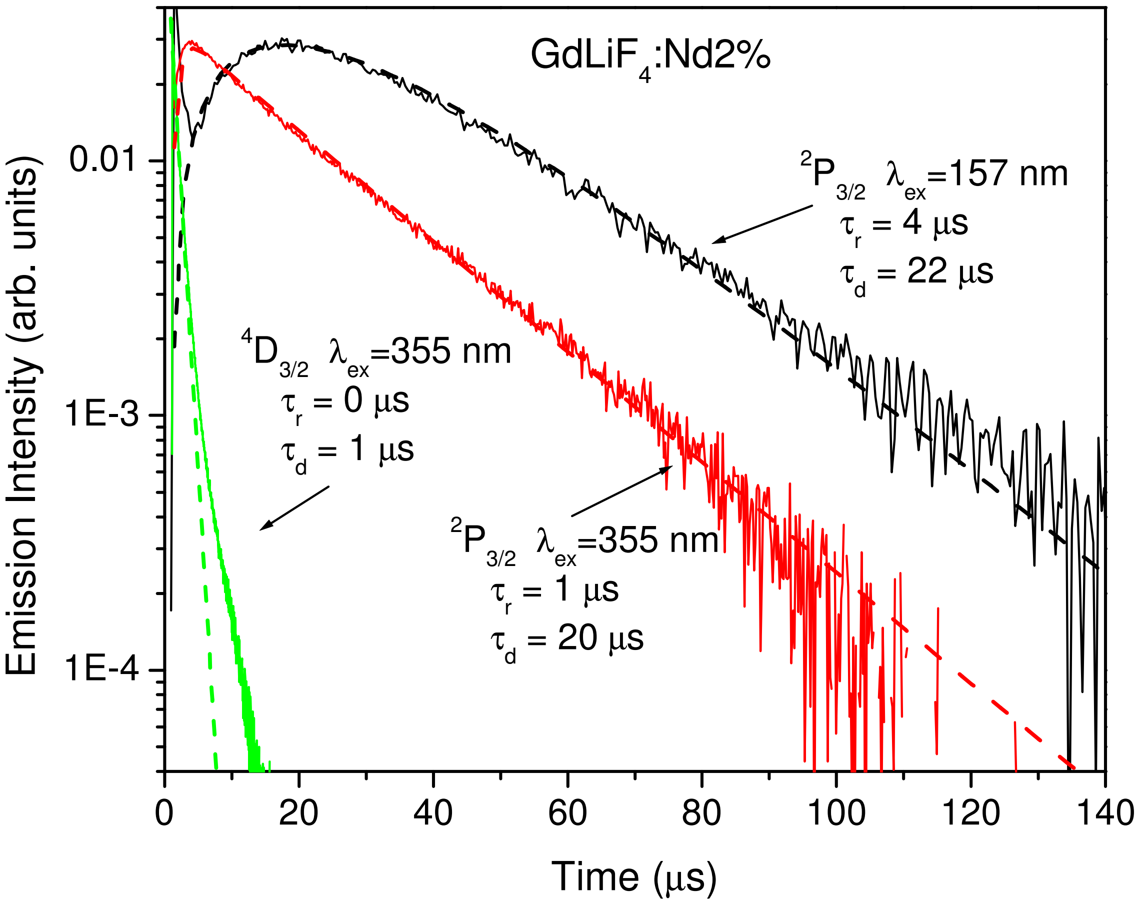

Fig. 5.9 Time evolution of the $^4D_{3/2}$ and $^2P_{3/2}$ emission of Nd^{3+} in a sample of GdLiF$_4$:Nd2% under 355 nm excitation and the $^4D_{3/2}$ emission

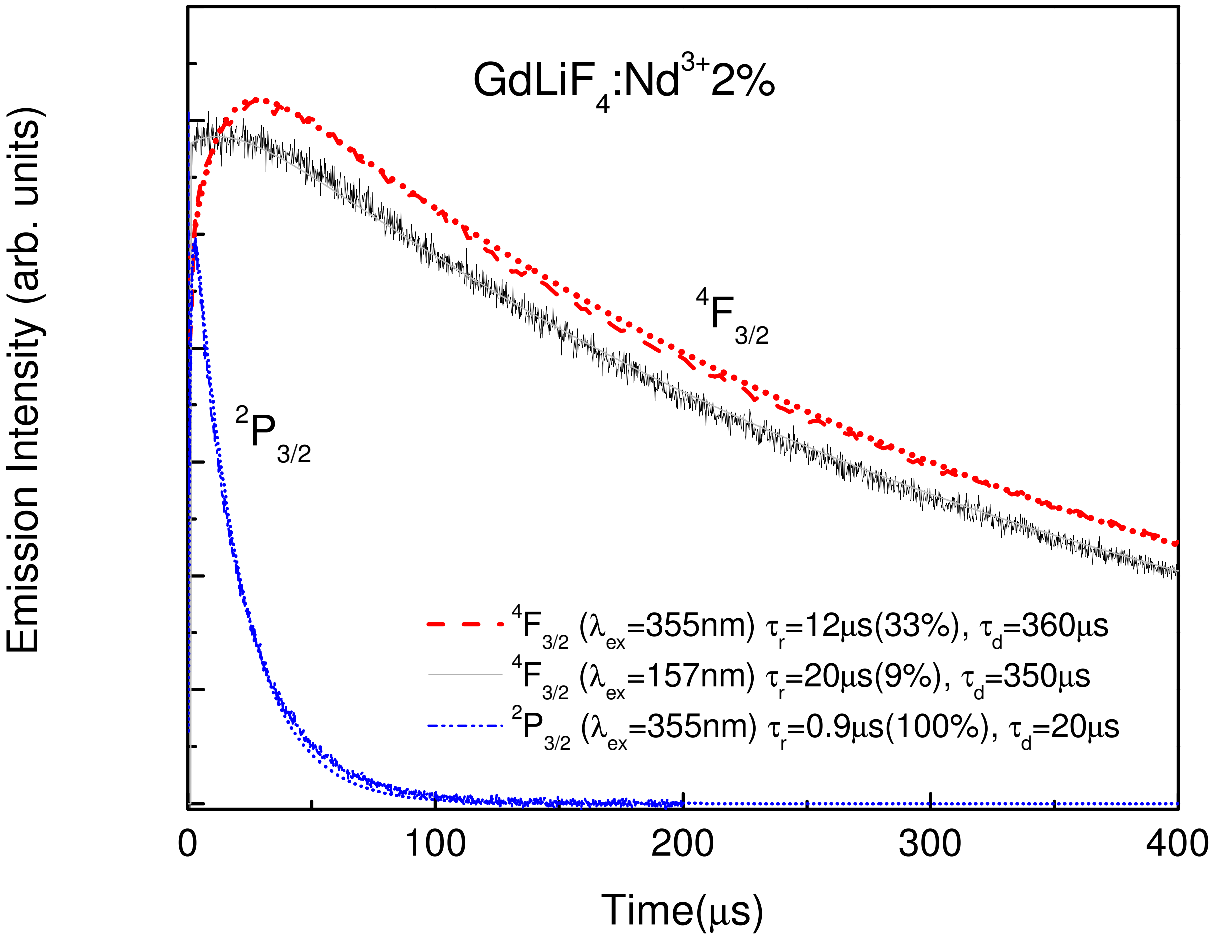

Fig. 5.10 Time evolution of the $^2P_{3/2}$ and $^4F_{3/2}$ emission in a GdLiF$_4$:Nd2% sample under 355 nm and 157 nm excitation

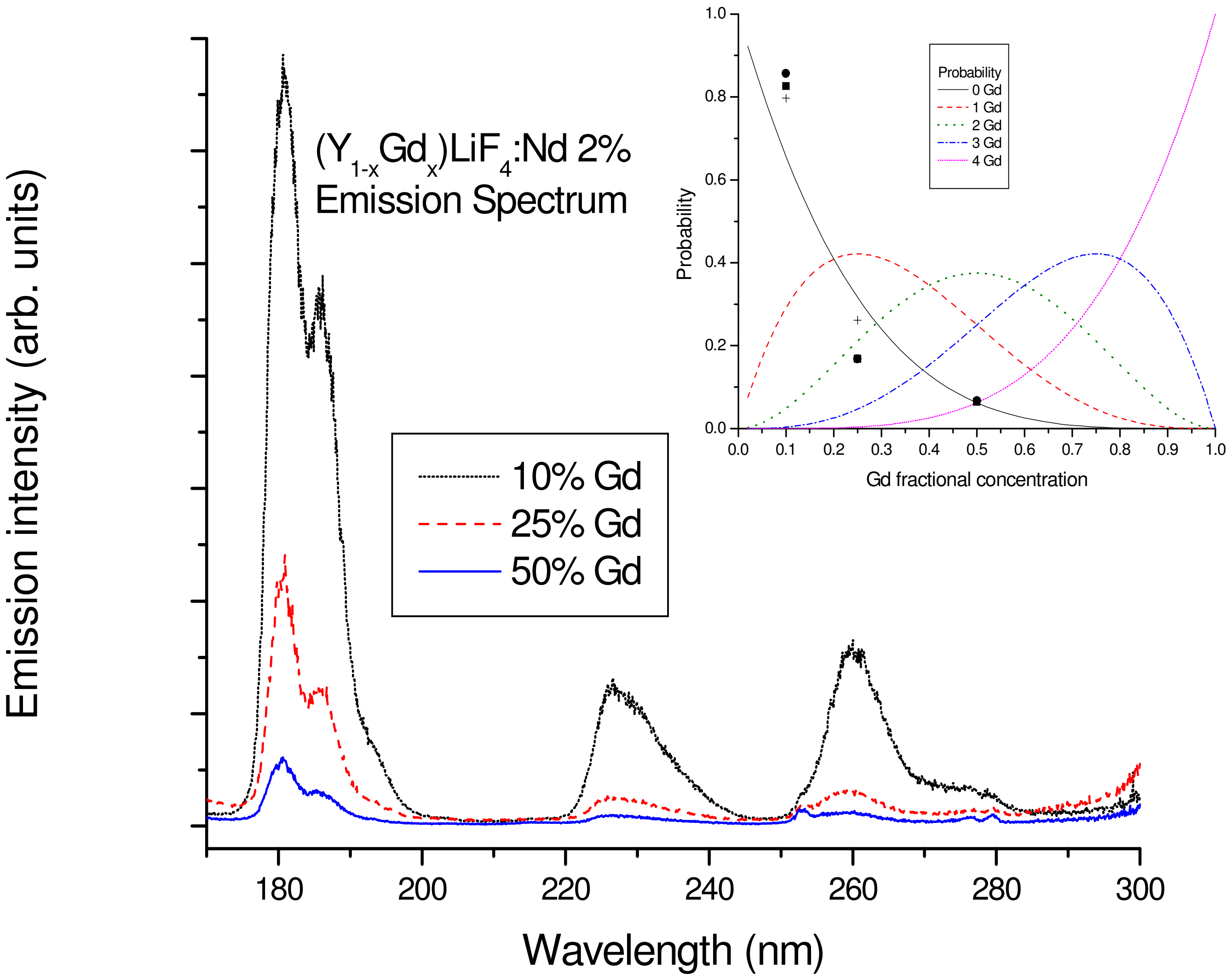

Fig. 5.11 Emission spectrum of Gd$_x$Y$_{1-x}$LiF$_4$: Nd at 157 nm.

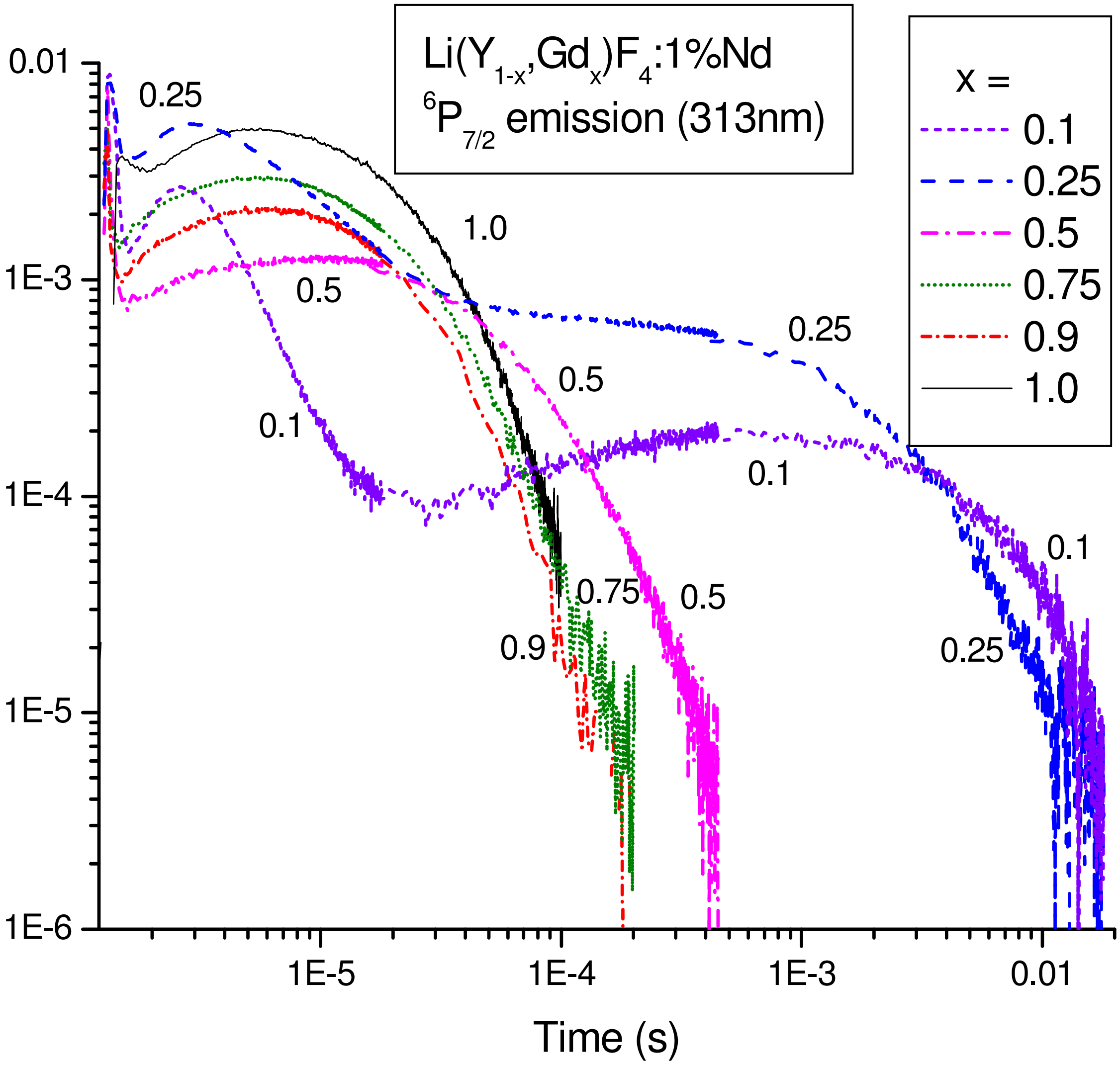

Fig. 5.12 Time-resolved emission at 313nm from the $^6P_{7/2}$ state of Gd^{3+}

CHAPTER 6

Sensitization of Gd^{3+} with the self-trapped exciton in $ScPO_4$: Gd^{3+}

6.1 Introduction

Photon cascade emission (PCE) has been demonstrated for the Gd^{3+} ion in $GdLiF_4$ [30], $GdBaB_9O_{16}$ [31], and $ScPO_4$ [32]. In this case, Gd^{3+} radiates in a sequential two step process; the first transition is $^6G \rightarrow {}^6P$ in the red followed by a $^6P \rightarrow {}^8S$ transition in the UV. However a second ion can be introduced so that an energy transfer occurs from the ^6P state of Gd^{3+} to this second ion which can emit a visible photon. Thus Gd^{3+} offers a number of opportunities for the development of quantum cutting phosphors. However, the practical use of PCE for Gd^{3+} has been limited by the inability to efficiently excite the ^6G state of Gd^{3+} since transitions to this state from its ground state are parity forbidden ($4f^7 \rightarrow 4f^7$) and the $4f^65d$ state lies at too high an energy to be accessible with a Xenon discharge. Attempts have been made by sensitizing Gd^{3+} with other rare earth ions which have 5d states such that they can be excited by the Xenon discharge, but none of these have provided the required efficiencies [33, 34].

An exciton, in essence, is an electron and hole moving with a correlated motion as an electron-hole pair. When an exciton is optically created, it is initially delocalized over the crystal due to the translational symmetry. However, in the deformable lattice, the exciton is trapped by its own lattice deformation if the exciton-lattice interaction is sufficiently strong. This phenomenon is called self-trapping [35]. The luminescence of the self-trapped exciton is intrinsic since it occurs even in the perfect crystal. Self-trapped excitons (STE) in wide-gap oxide crystals have been studied for at least thirty years. Although a methodological approach has been successfully developed for the STE in alkali halides (AH) and alkali earth fluorides, there is no universal opinion about the mechanism of excited state formation and the models of STE in oxides [36].

Efficient energy transfer from the host excitations (STE) excited by the VUV radiation to Ce^{3+} was observed in $ScBO_3$ [37]. The observation of energy transfer from host (STE) to rare earth ions in Pr^{3+}-doped $CdSiO_3$, a long-lasting afterglow phosphor, is also reported [38].

It has been shown that the self-trapped exciton (STE) can be used to sensitize the ^6G states of Gd^{3+} but the quantum efficiency was only about 100% under 160 nm excitation, not the desired 200% [30]. The problem lies in part to the fact that 75% of the energy flows to the lower lying ^6D and ^6I states of Gd^{3+} which cannot produce visible quantum cutting. Here we examine in detail the $STE \rightarrow Gd^{3+}$ (^6G) energy transfer process, especially the dynamics and its temperature dependence, so as to better understand this process in order that we might evaluate it and optimize it for sensitizing the ^6G state of Gd^{3+}. More generally, these results should be of relevance to the use of the STE as a sensitizing agent.

6.2 Temperature dependence of the emission

$ScPO_4$ has a self-trapped exciton (STE) emission which peaks at 220 nm, one of the shortest known STE emissions. Only some fluorides and a few oxides such as Al_2O_3 show self-trapped exciton (STE) emission at shorter wavelengths [39]. The emission spectrum of an undoped and a 1% Gd^{3+}-doped $ScPO_4$ sample at 300 K is shown in Fig. 6.1. The Gd^{3+} transitions which appear in Fig. 6.1 are identified on the energy level diagram in Fig. 6.2. Also shown schematically in Fig. 6.2 are the initial *e-h* pair and the relaxed self-trapped exciton (STE) state. After creation of the *e-h* pair by the absorption of the VUV photon in an above band gap transition, an exciton is formed which becomes self-trapped as a self-trapped exciton (STE). When Gd^{3+} is introduced, the self-trapped exciton (STE) emission is almost totally quenched with the appearance of ^6G states emission from Gd^{3+}, along with emission from the ^6P state. This replacement of the self-trapped exciton (STE) emission with ^6G emission of Gd^{3+} strongly suggests a $STE \rightarrow Gd^{3+}$ energy transfer involving the ^6G states. The spin-allowed Gd^{3+} transitions from ^6G are much stronger than the spin forbidden transitions. However, the much higher transition energy of the spin forbidden transition to the ground state at 204 nm partially compensates for its spin-forbidden character as the radiative rates are proportional to cube of the transition frequency. As a result it retains considerable intensity.

When the sample containing 1% Gd^{3+} is cooled to 77 K, the self-trapped exciton (STE) emission, which had almost vanished due to the Gd^{3+} doping at 297 K, increases in intensity and is again clearly observed. This is shown in Fig. 6.3 which compares the 77 K and 297 K spectra. Along with an increase in the self-trapped exciton (STE) emission in going from 297 K to 77 K, the Gd^{3+} ^6G emission intensity decreases. These facts suggest a decrease in the efficiency of the $STE \rightarrow Gd^{3+}$ energy transfer as the temperature is reduced. Presumably this implies an energy transfer rate which increases with temperature.

The temperature dependence of the luminescence is shown in detail in Fig. 6.4 for both the undoped and 1% Gd^{3+} samples. Even the undoped sample exhibits a self-trapped exciton (STE) intensity that decreases with an increase in temperature. This likely results from a partial energy transfer to “killer centers” due to the presence of defects or impurities to which energy may be transferred but which do not radiate. For the 1% Gd^{3+} sample the temperature dependence of the self-trapped exciton (STE) emission is much stronger, nearly totally quenching the self-trapped exciton (STE) emission at room temperature. It appears that the energy transfer to the Gd^{3+} ions dominates over energy transfer to the “killer centers” in the Gd^{3+}-doped material.

6.3 Time dependence of emission dynamics

At room temperature the lifetime of the STE emission shortens from 75 ns in the undoped sample to 8 ns in the sample containing 1% Gd^{3+}. This observation is consistent with a strong energy transfer from the STE to Gd^{3+}. We also measured a STE decay time of 130 ns at 300 K in a single crystal of $ScPO_4$. The longer lifetime in the single crystal tells us that in our powders (and perhaps also the crystal) this is not the radiative lifetime, a fact that is not surprising in the presence of energy transfer to “killer centers”. We now examine the temperature dependence of the dynamics to help identify the energy transfer processes and to determine their mechanisms.

The time dependence as a function of temperature of the STE emission at 220 nm in both the doped (left) and undoped (right) samples is shown in Fig. 6.5 under pulsed excitation at 157 nm. For the undoped sample, there is a striking increase in the lifetime as the temperature is reduced, reaching 2.5 μs at 77 K. One also notices a decrease of the initial intensity of the STE at the lowest two measured temperatures. This means either that the radiative rate of the STE exciton noticeably decreases below about 150 K or that the efficiency for the creation of the STE decreases at the lower temperatures. We think that the latter is unlikely and that the reduced initial intensity results from a reduction of the radiative rate for reasons that will be discussed below. A similar reduction in initial intensity is seen for the 1% Gd^{3+} sample. In this sample, the temperature dependence is much more dramatic. At 77 K, the STE lifetime is nearly identical in the two samples. This suggests that at 77 K the $STE \rightarrow Gd^{3+}$ energy transfer no longer competes with the radiative rate and has thus become unimportant in determining the STE luminescence dynamics. The lifetime is therefore purely a measure of the radiative rate and is the same in both samples. However, it will be shown that this radiative lifetime is itself still temperature dependent. This can be explained by assuming two STE states with two different radiative rates, whose relative populations are of course temperature dependent.

6.4 Model of the luminescence dynamics

In order to explain the temperature dependence of both the intensity and decay rate of the STE we propose the following model schematically outlined in Fig. 6.6. We assume two STE states, STE 1 and STE 2 with very different radiative rates. Their populations are N_1 and N_2, respectively. These might arise from the high spin and low spin STEs arising from the two possible relative spin orientations for the exciton electron-hole pair, as observed in the alkali halides [40]. In this model, the triplet lies lowest with a radiative rate of $\tau(1)_{RAD}^{-1}$ while the singlet, lying at an energy Δ higher in energy, has a much larger radiative rate $\tau(2)_{RAD}^{-1}$. Alternatively the STE may have many excited states as seen in $PbWO_4$ where the splitting between the lowest two STE excited states is 1044 cm^{-1} [41]. For a 1% Gd concentration it is statistically unlikely that the STE will be created close to a Gd. Therefore, at low temperature, when the STE is localized, the energy transfer rate to Gd^{3+} is sufficiently reduced such that it is relatively unimportant in controlling the emission dynamics. As the temperature is raised, the STE becomes mobile and a thermally assisted energy transfer process is activated with an activation energy of ΔE_{ET}, increasing the probability that the STE and Gd^{3+} will be proximate for a portion of the time. Although the energy transfer consists of two steps, the energy migration of the STE to the vicinity of the Gd^{3+} followed by energy transfer to the Gd^{3+}, each with their own activation energy [42], we assume that one of these is much faster so that the other is the rate-limiting process at all experimentally observed temperatures. The above statement also applies to the energy transfer to the killer centers. We note that self-quenching of the STE emission is a possible alternative to quenching by killer centers. While it is not possible to eliminate this possibility, the fact that the data can be fitted with a single activation energy for both the STE$\rightarrow$Gd^{3+} energy transfer and the quenching process in the undoped materials suggests that it is the exciton mobility that dominates the dynamics at higher temperatures, not the self-quenching. Furthermore, in order to keep the model relatively simple, we also assume the same activation energy and energy transfer rate from both STE states. These assumptions turn out to be adequate to explain the experimental results.

In such a model, the STE decay rate can be expressed as

$$\tau_{STE}{}^{-1} = \tau_{RAD}{}^{-1} + \tau_{ET}{}^{-1} = N_1\tau(1)_{RAD}{}^{-1} + N_2\tau(2)_{RAD}{}^{-1} + W_{ET}\exp(-\Delta E_{ET}/kT) \tag{6.1}$$

where $N_2/N_1 = \exp(-\Delta/kT)$. $\tau_{ET}{}^{-1}$ includes energy transfer to both Gd^{3+} and killer centers and any other intrinsic STE quenching processes. Here, W_{ET} is the frequency factor for the energy transfer. The integrated STE intensity will be proportional to the product of the radiative rate and the lifetime according to

$$I_{STE} \propto \tau_{RAD}{}^{-1}\tau_{STE} \tag{6.2}$$

In Fig. 6.7, we compare the results of the model to the experimental data for the STE decay rate. In Fig. 6.8, we compare the results of the model to the experimental data for the normalized STE intensity. The open circles and squares refer to the experimentally determined decay rates of the undoped and 1% Gd-doped samples, respectively. The open circles and squares also refer to the observed normalized STE intensity of the undoped and 1% Gd-doped samples, respectively in Fig. 6.8. Also shown on Fig. 6.7 with the symbol Δ is the buildup rate of the ^{6}P Gd^{3+} emission. It is close to the decay rate of the STE at all but the lowest temperatures. The rate equations for the model were solved as the parameters in the model were varied so as to provide a best fit to both the temperature dependence of the STE decay rate and intensity. The best fits, shown by the solid and dashed lines in Fig. 6.7 and Fig. 6.8, describe the main features of the temperature dependence. The resulting parameters are shown on Fig. 6.6. Note the W_{ET} is about an order of magnitude higher in the Gd-doped samples indicating that the energy transfer rate to Gd is about ten times greater than the rate to the "killer centers" assuming the same activation energy for energy transfer to both centers. The two STE states are split by about 280 cm^{-1} and the radiative rate of the singlet STE state is about two orders of magnitude greater than that of the triplet. The thermal activation energy for energy migration is about the energy of one optical phonon in this lattice.

6.5 Conclusions

Sensitization of the ^{6}G states of Gd^{3+} by energy transfer from the self-trapped exciton has been demonstrated and its dynamics has been determined. As shown previously, the efficiency of energy transfer to the ^{6}G states is only about 30%, limiting the usefulness of this material as a quantum cutting phosphor. At room temperature the energy transfer to Gd^{3+} ions is highly efficient competing effectively with both radiative decay of the STE and energy transfer to killer centers. A rate equation model describes the dynamics quite well. The model assumes two STE exciton states split by 280 cm^{-1}, whose radiative rates differ by about two orders of magnitude. A comparison of the model with the experimentally measured temperature dependence of both the dynamics and emission intensity allows for a detailed study of the thermally activated energy transfer and a determination of the activation energy as 970 cm^{-1}.

To use STE sensitization of the ^{6}G states of Gd^{3+} for quantum cutting, it will be necessary to identify materials whose STE emission occurs at even shorter wavelengths than is the case for $ScPO_4$ so that a larger fraction of the energy transfer occurs to the ^{6}G states or even higher-lying states of Gd^{3+}. Results of this study, however, do demonstrate that the sensitization with the STE is a very effective means of obtaining good coupling of the VUV excitation to Gd^{3+}.

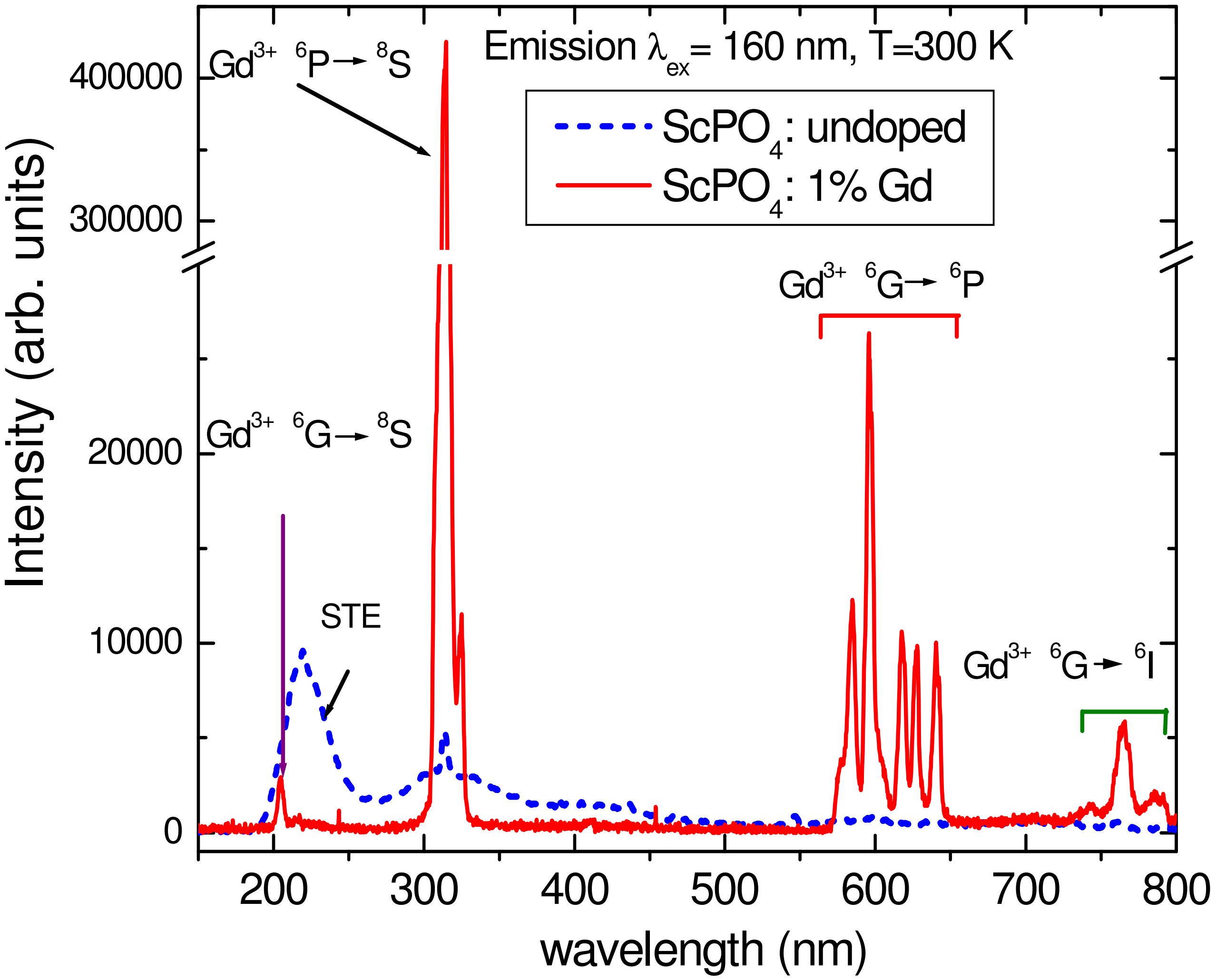

Fig. 6.1 Emission spectra of undoped and 1% Gd-doped $ScPO_4$ at T=300 K.

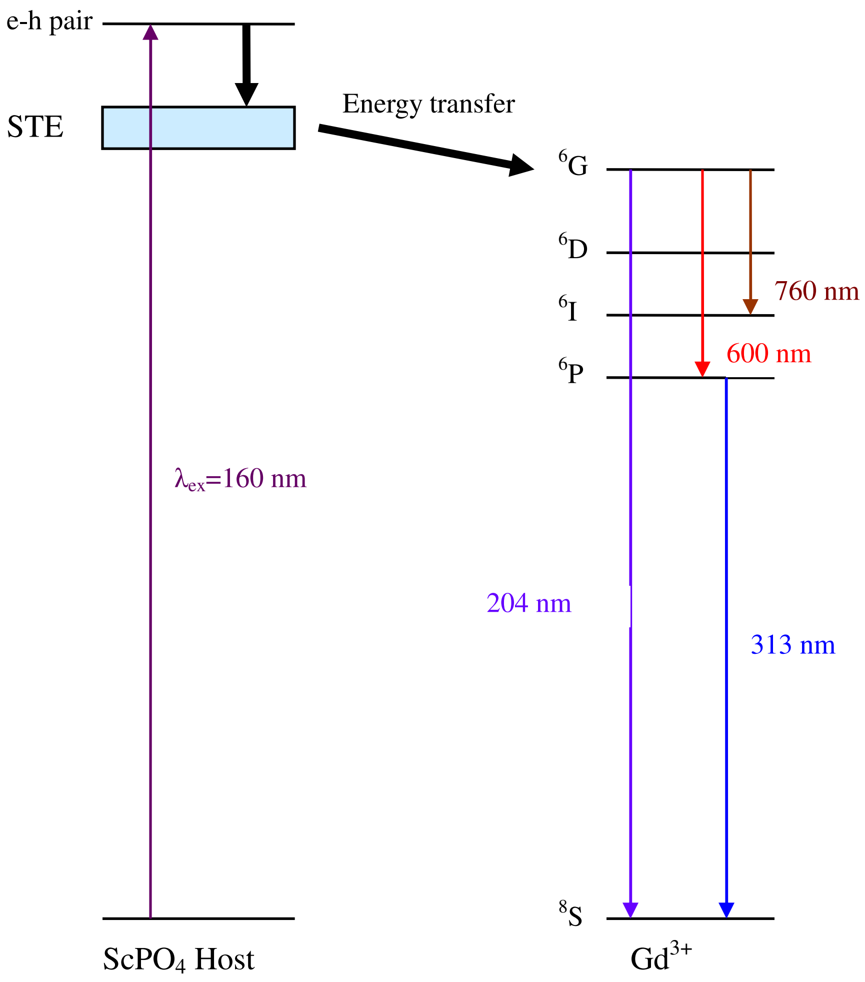

Fig. 6.2 Schematic showing the creation of the initial e-h pair, the relaxation to form the STE, and the subsequent energy flow to the excited states of Gd^{3+}.

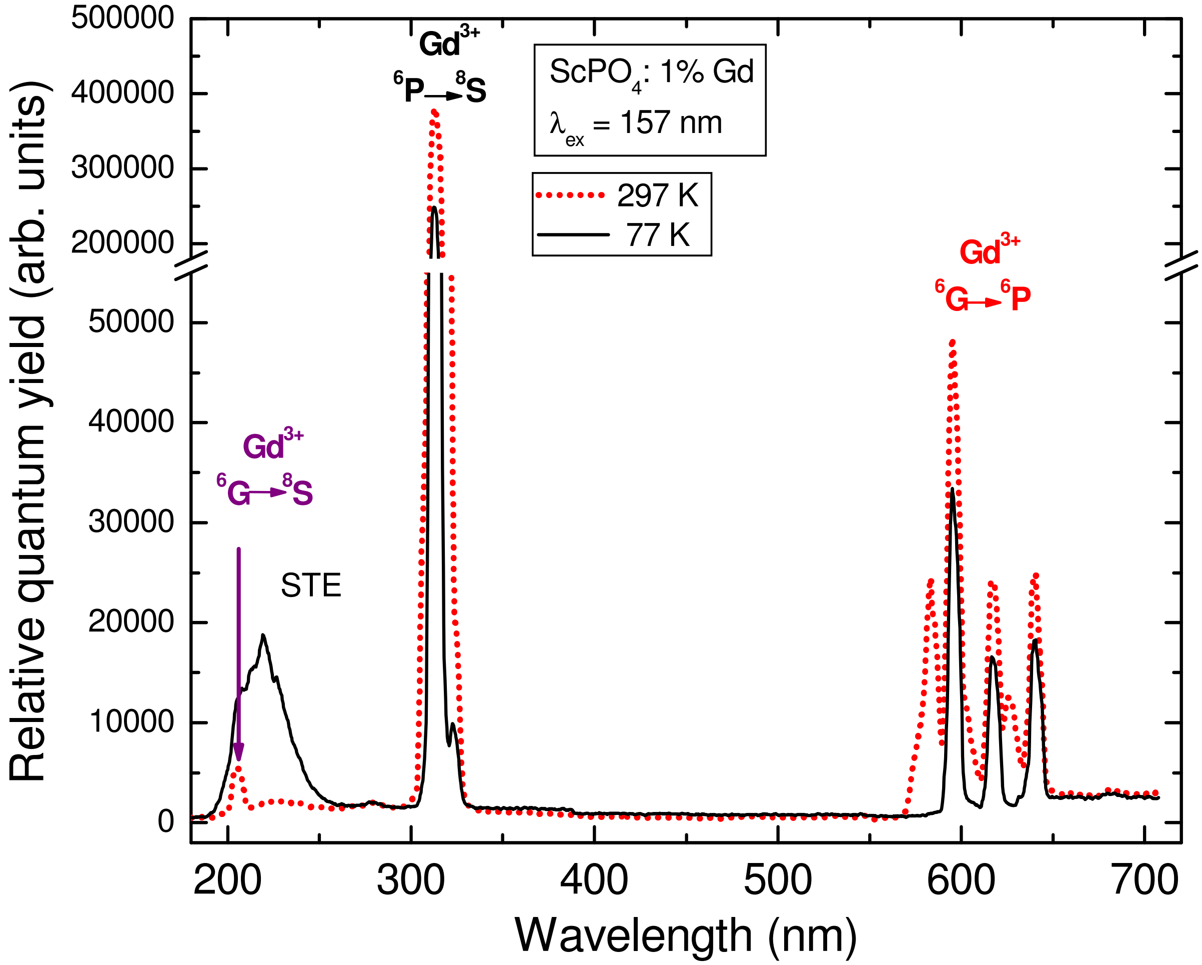

Fig. 6.3 Emission spectra excited of 1% Gd-doped ScPO$_4$ at T=77 and 300 K

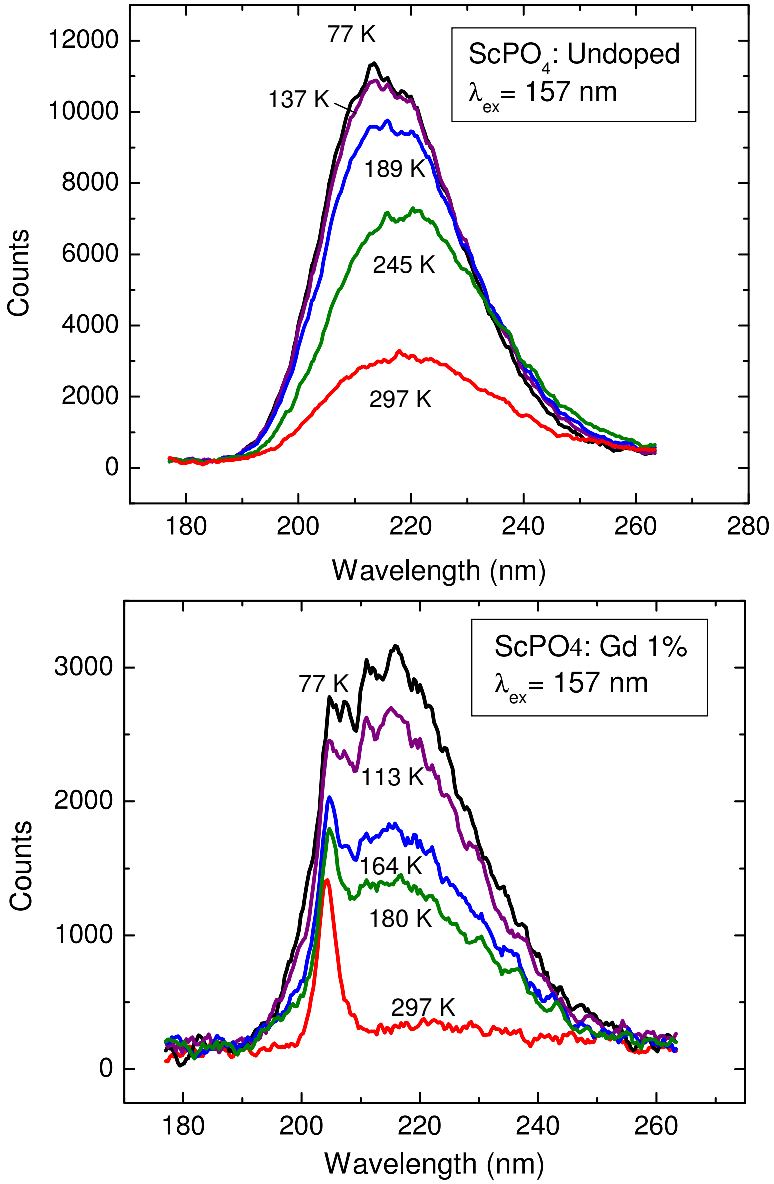

Fig. 6.4 VUV emission spectra of undoped and 1% Gd-doped $ScPO_4$ as a function of temperature.

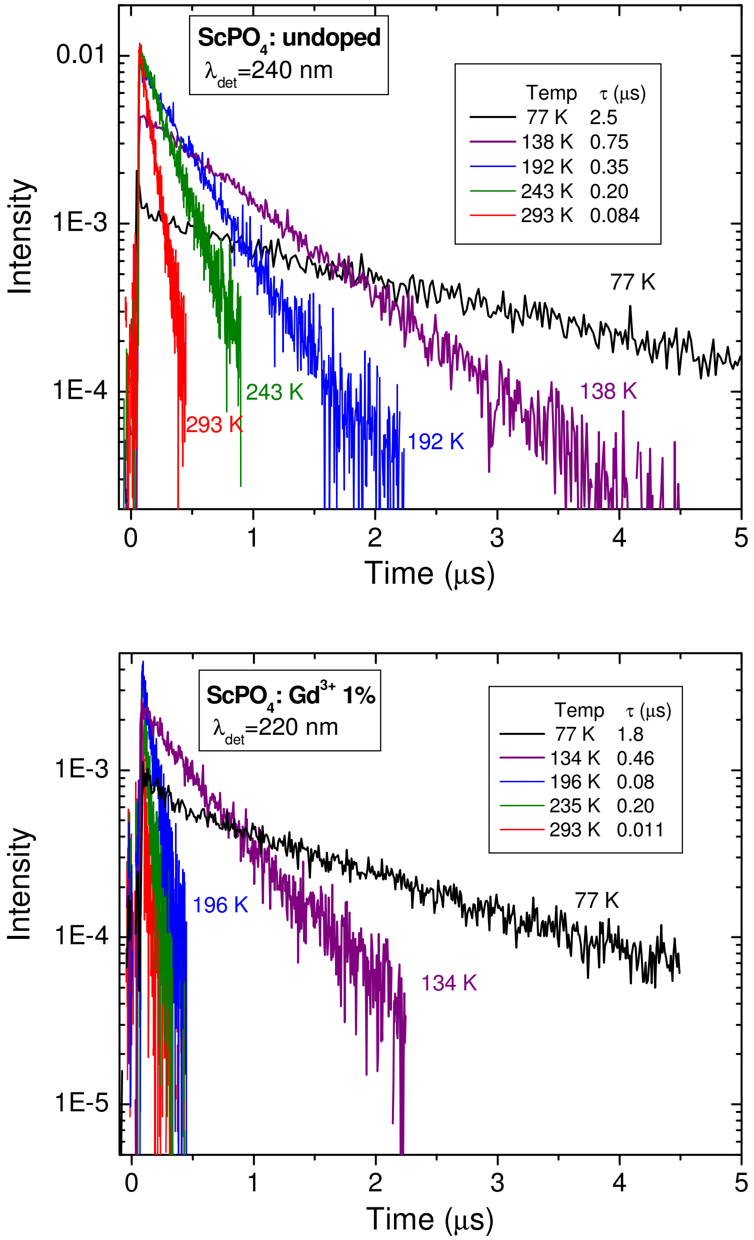

Fig. 6.5 Time dependence of the emission, excited at 157 nm, of undoped (upper) and 1% Gd-doped ScPO$_4$ as a function of temperature.

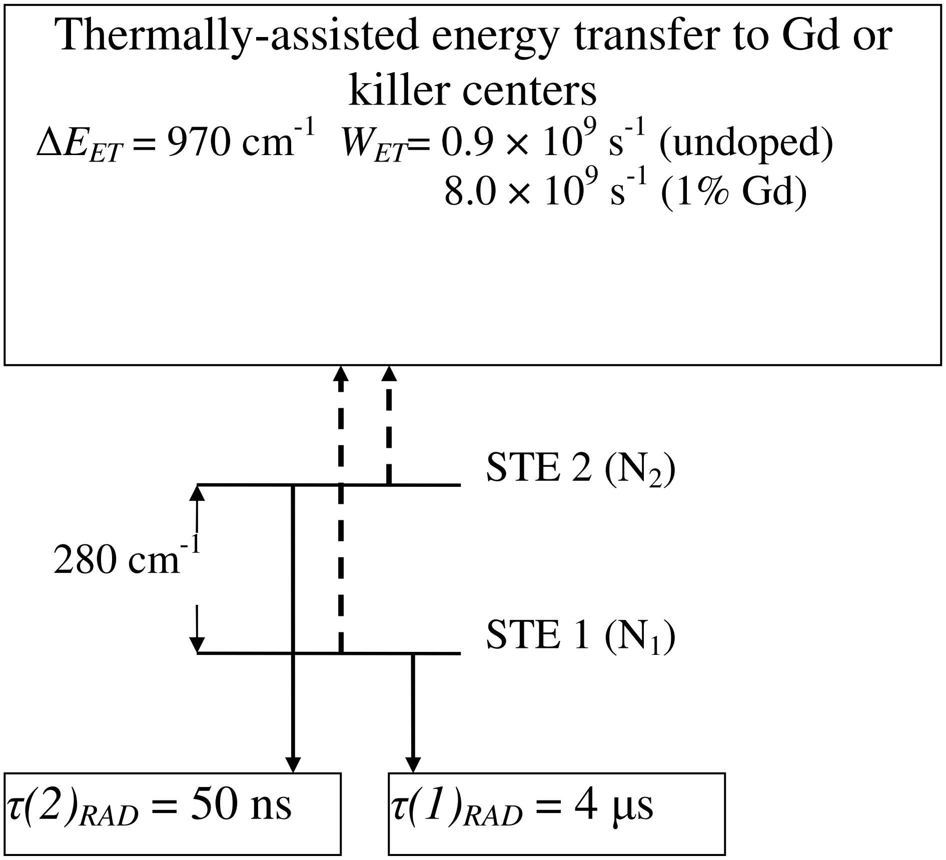

Fig. 6.6 Schematic indicating the model used to fit the temperature dependence of the rates and normalized integrated emission intensities of undoped and 1% Gd-doped $ScPO_4$.

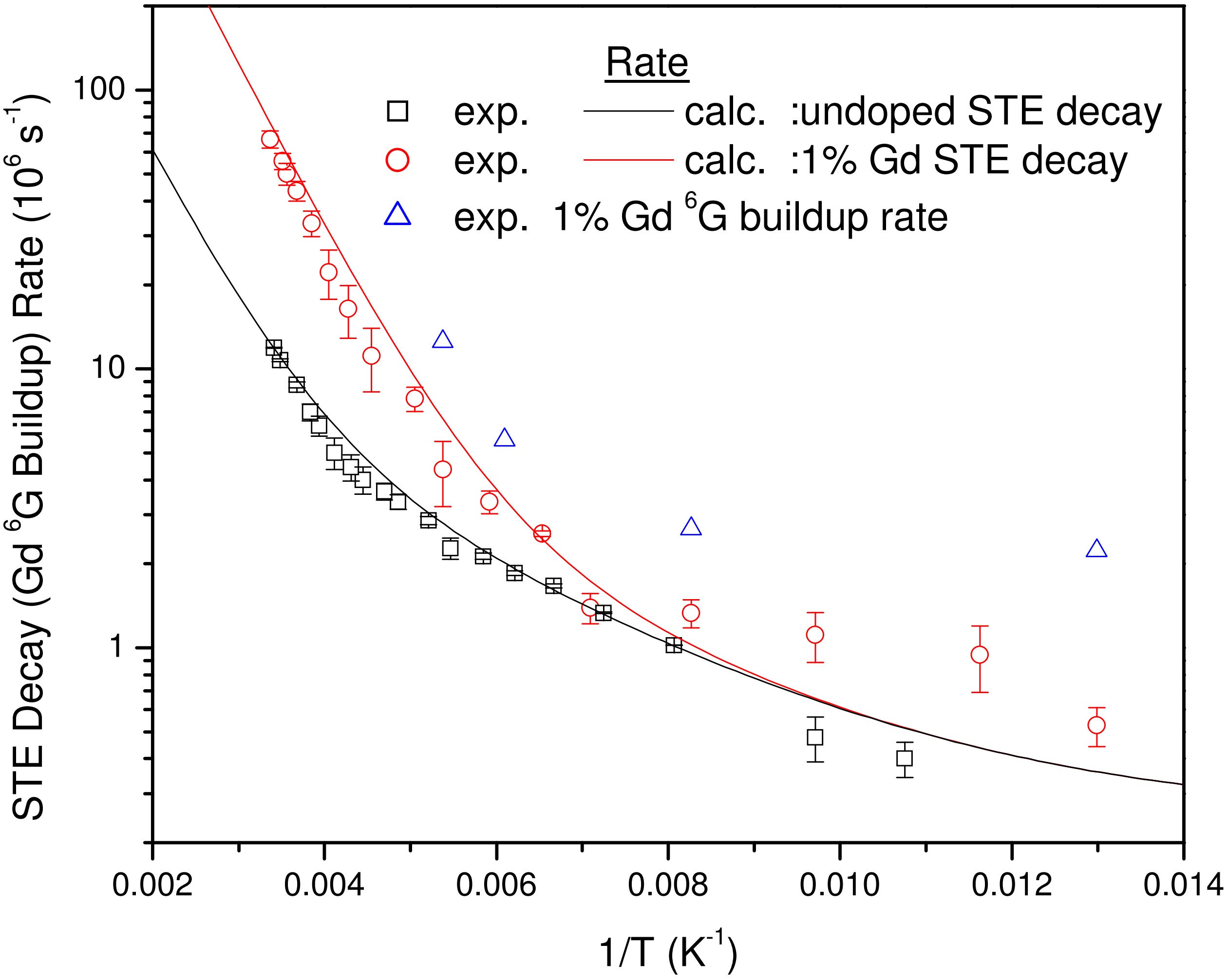

Fig. 6.7 Comparison of the data to the best fits of the model shown in Fig. 6.6 for the rates as a function of temperature for the undoped and 1% Gd-doped $ScPO_4$.

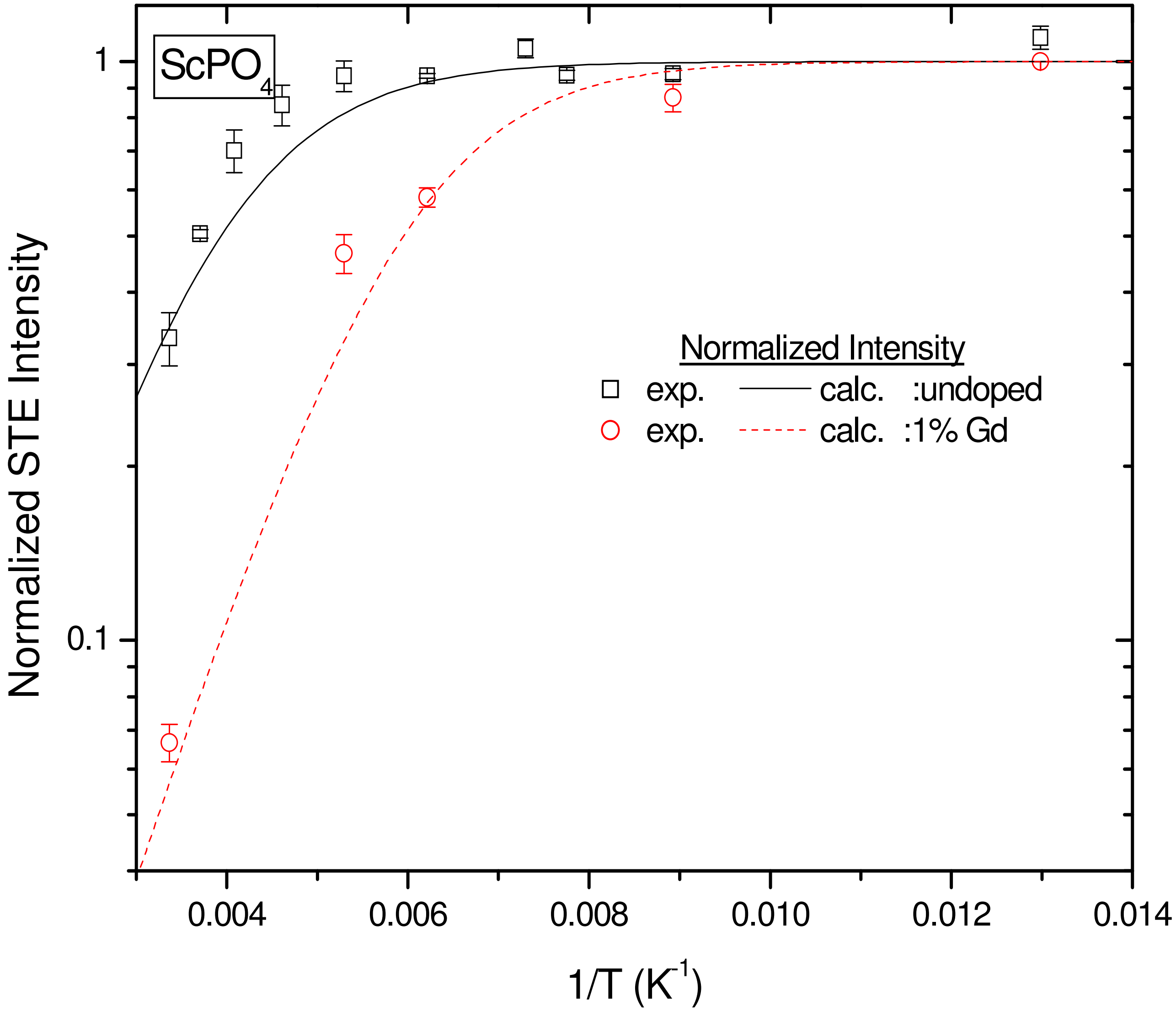

Fig. 6.8 Comparison of the data to the best fits of the model shown in Fig. 6.6 for the normalized STE intensity

CHAPTER 7

Sensitization of Gd^{3+} with the self-trapped exciton in $GdZrF_7$: Eu^{3+}

7.1 Introduction

There has been little work done on the luminescence of the monoclinic $GdZrF_7$ since its structural information was provided by Poulain in 1972 [43]. E. van der Kolk *et al.* did a VUV excitation study of Pr^{3+} doped $LaZrF_7$ which is isostructural with $GdZrF_7$ [44]. They demonstrated photon cascade emission (PCE) of Pr^{3+} and energy transfer from the STE to Pr^{3+}. In their paper the reported excitation and emission characteristics of Pr^{3+} doped in $LaZrF_7$ at ≈293 and at ≈10 K are described. In $LaZrF_7$ broad band emission around 360 nm was observed. The corresponding excitation bands are located in the VUV and overlap with the 4f5d states of Pr^{3+}. Differences observed in the 293 K excitation spectra of the $^1S_0$ emission and $^3P_0$ emission for band-to-band excitation and also for excitation at higher energies in $LaZrF_7$ were attributed to the creation of STEs followed by thermally stimulated diffusion to Pr^{3+}. However energy is transferred mainly to the $^3P_0$ state of Pr^{3+} and not to the $^1S_0$ state. $STE \rightarrow Pr^{3+}$ energy transfer is inefficient at 10 K and STE emission is observed instead.

Because quantum cutting is observed in Pr^{3+} doped $LaZrF_7$, we try to substitute another rare earth for La. In this chapter we study $GdZrF_7$ and Eu^{3+} doped $GdZrF_7$. The Gd-Eu pair has been discussed in previous chapters and our concern is the sensitization of Gd. We hope to see that energy will be transferred from the STE to Gd. Because the emission of the host is around 400 nm, it is impossible to use the STE to sensitize the ^6G states of Gd. Here we study in detail the $STE \rightarrow Gd^{3+}$ (^6P) and $Gd^{3+} \rightarrow Eu^{3+}$ energy transfer processes, especially the dynamics and its temperature dependence in both undoped and Eu^{3+} doped $GdZrF_7$ to determine the feeding and loss mechanisms.

7.2 Emission Spectrum

The emission spectrum of an undoped and a 1% Eu^{3+}-doped $GdZrF_7$ sample at 300 K is shown in Fig. 7.1. Both of these two samples have a broad STE emission which peaks at 420 nm. For the undoped sample, one can see broad emission band likely arising from a STE and sharp Gd^{3+} ^6P emission. For the 1% Eu^{3+}-doped sample, the low intensity of the Gd^{3+} ^6P emission suggests the efficient energy transfer from Gd^{3+} to Eu^{3+} ($^6P \rightarrow {}^5D_3 \rightarrow {}^5D_2 \rightarrow {}^5D_1 \rightarrow {}^5D_0$) but there appears to be very little direct transfer from the STE to Eu^{3+}.

We cooled the undoped $GdZrF_7$ to 77 K to study temperature dependence of the emission. The spectrum is shown in Fig. 7.2. One can see that the integrated intensity of the STE decreases with increase in temperature. Meanwhile, the Gd^{3+} ^6P emission increases as the STE emission decreases. So we can say there is a temperature-dependent STE→Gd energy transfer in this sample. When we normalized the emission of the STE at different temperature to the emission at 77 K, one can see the STE emission broadens with an increase in T. The overlap of the STE emission with the Gd^{3+} ^6P absorption increases with T. This is shown in Fig. 7.3.

7.3 Excitation spectrum

The excitation spectrum of Eu^{3+}-doped $GdZrF_7$ is shown in Fig. 7.4. From the emission spectrum one can see that this sample has visible emission occurring both from the STE and from Eu^{3+}. In order to obtain the absolute quantum yield (QY), we used two reference materials, sodium salicylate (NaSal) and Y_2O_3: Eu. When we used NaSal as reference, we used a Corning 5-56 filter to measure the excitation spectrum of $GdZrF_7$: Eu. We used a Schott WG495 filter for the excitation spectrum relative to Y_2O_3: Eu. Then we corrected these excitation spectra for filter transmission and PMT response as described in Sec. 3.3.2. One can see that the quantum yield of this sample is about unity. It is similar to the result of E. van der Kolk *et al.* [44]. E. van der Kolk *et al.* found that the $^3P_0$ emission of Pr^{3+} had an internal quantum efficiency close to unity.

7.4 Temperature dependence of emission dynamics

At room temperature the lifetime of the STE emission of the undoped sample is almost the same as the sample containing 1% Eu^{3+}. This observation is consistent with very little direct transfer from the STE to Eu^{3+}. It is shown in Fig. 7.5.

The time dependence, under pulsed excitation at 157 nm, as a function of temperature of the STE emission at 420 nm in undoped sample is shown in Fig. 7.6. For the undoped sample, there is a striking increase in the lifetime as the temperature falls, reaching 45 μs at 77 K and the decay is nearly exponential. The time dependence as a function of temperature of the ^6P emission of Gd^{3+} at 313 nm in undoped sample is shown in Fig. 7.7. It is shown that the ^6P Gd^{3+} population buildup has two components. The fast component rise time is temperature independent and nearly constant (τ_{rise}=0.35 μs). The slow component is identical to that of the STE decay and is temperature dependent. One also can see that the Gd^{3+} ^6P emission intensity decreases when the temperature decreases. It suggests a reduced energy transfer from the STE at lower temperatures. The time dependence of the Gd^{3+} ^6P emission of undoped $GdZrF_7$ at 77 K is shown in Fig. 7.8. We find that there is a broad background with a fast decay that lies underneath the ^6P Gd^{3+} emission. We measured the time dependence spectrum at 313 nm (^6P emission) and also measured the time dependence spectra at 305 and 320 nm (either side of Gd ^6Pemission at 313 nm) respectively. Then we averaged the data of 305 and 320 nm. When we subtracted this broad background from the total emission, the ^6P rises from zero at $t = 0$. This broad background also has a slower component whose decay agrees with that of the main STE emission band. The study of two components of the broad background is shown in Fig. 7.9. The fast component has a decay of 0.35 μs and is found to be independent of temperature which is shown in Fig. 7.10. The slow component of the decay is the same as that of the main STE emission. This suggests the presence of two types of centers, the fast one having its luminescence at shorter wavelengths than that of the slower (STE). This is the reason for center 2 in the model discussed below which receives 7% of the excitation energy and transfers it to Gd quickly. In Fig. 7.11, it is shown that the $Gd^{3+} \rightarrow Eu^{3+}$ energy transfer rate increases with an increase in the Eu^{3+} concentration.

7.5 Model for the Dynamics of the Populations

In order to fit the temperature dependence of both the STE and Gd^{3+} ^6P decay with regard to both the relative intensities and decay rates, we propose the following model schematically outlined in Fig. 7.12. In this model, we assume the STE receives 93% and the center 2 (defect) receives 7% of the excitation energy. The STE transfers energy to Gd in the ^6P state with a rate of $W_{ET}^{STE}(T)$. Meanwhile, the STE relaxes by e-h recombination at a radiative rate of $W_R^{STE}(T)$. The center 2 also feeds Gd in the ^6P state with a rate of W_{ET}^{C2} (3×10^6 s^{-1}). After the excitation of the ^6P state of Gd, $Gd^{3+} \rightarrow Eu^{3+}$ energy transfer occurs by cross relaxation. In the meantime, Gd^{3+} relaxes to its ground state with a radiative rate W_R^{Gd} (2.7×10^2 s^{-1}). The temperature dependence of the STE radiatative ($W_R^{STE}(T)$) and the energy transfer rate to Gd^{3+} ($W_{ET}^{STE}(T)$) are varied to fit the time dependence of both the STE and Gd^{3+} ^6P emission.

In this model, the rate equations can be expressed as

$$\frac{dN_1}{dt} = -\left(W_{ET}{}^{STE} + W_R{}^{STE}\right)N_1$$

$$\frac{dN_2}{dt} = -\left(W_{DG} + W_{DR}\right)N_2$$

$$\frac{dN_3}{dt} = W_{DG}N_2 + \left(W_{ET}{}^{STE}N_1 - W_R{}^{GD}N_3\right)$$

W_{DG} is the energy transfer rate from center 2 to Gd shown as $W_{ET}{}^{C2}$ in Fig. 7.12. W_{DR} is the radiative decay of center 2 which is set equal to zero. N_1 is the relative population of the STE which is set equal to 0.93 at $t = 0$. N_2 is the relative population of center 2 which is set equal to 0.07 at $t = 0$. N_3 is the relative population of Gd in the ^6P state, initially zero. The rate equations for the model were solved as the parameters in the model were fixed except $W_R{}^{STE}(T)$ and $W_{ET}{}^{STE}(T)$ so as to provide a best fit to both the time dependence and relative intensities. The results are shown in Fig. 7.13. The temperature dependence of the best-fit rates are shown in Fig. 7.14. From this figure, one can see the energy transfer rate to Gd increases rapidly with temperature and the STE radiative rate increases more slowly with an increase in T. STE decay rate is the summation of $W_R{}^{STE}(T)$ and $W_{ET}{}^{STE}(T)$.

7.6 Mechanism for the STE$\rightarrow$Gd^{3+} Energy Transfer

Since the Gd^{3+} is present at 100% concentration, it seems unlikely that mobility of the STE is important in the dynamics of the STE$\rightarrow$Gd^{3+} energy transfer. The STE$\rightarrow$Gd^{3+} energy transfer probably results from the weak overlap of the high energy tail of the STE emission and the ^6P Gd^{3+} absorption. The mechanism can be either the dipole-dipole or exchange interaction. The temperature dependence of the STE$\rightarrow$Gd^{3+} energy transfer rate results from the increased overlap as the STE broadens with temperature. The surprisingly low energy transfer rate at this 100% concentration probably arises from the very poor overlap of the STE emission and Gd^{3+} absorption. Despite the relatively slow energy transfer rates, it still effectively competes with the slow radiative rates to produce significant energy transfer to Gd^{3+}. The negligible STE to Eu energy transfer also suggests that the STE is not mobile. At the low concentrations, it is statistically unlikely that the STE and Eu are nearby so that in the absence of mobility, there is little transfer of energy.

7.6 Conclusions

Sensitization of the ^6P state of Gd^{3+} by energy transfer from the self-trapped exciton has been demonstrated and its dynamics has been determined. The STE$\rightarrow$$Gd^{3+}$ energy transfer occurs by dipole-dipole or exchange interactions due to the overlap of the high energy tail of the STE emission and Gd^{3+} ^6P absorption. The temperature dependence of the STE→Gd energy transfer rate results from the increased overlap as the STE broadens with temperature. The surprisingly low energy transfer rate at this 100% concentration probably arises from the very poor overlap of the STE emission and Gd^{3+} absorption. Despite the relatively slow energy transfer rates, it still effectively competes with the slow radiative rates to produce significant energy transfer to Gd^{3+}.

For the Eu^{3+}-doped $GdZrF_7$, Gd^{3+} transfers energy very effectively to Eu^{3+} and the rate is proportional to the Eu^{3+} acceptor concentration. Energy transfer processes involve STE$\rightarrow$$Gd^{3+}$ (^6P)$\rightarrow$$Eu^{3+}$ ($^5D_3\rightarrow{}^5D_2\rightarrow{}^5D_1\rightarrow{}^5D_0$). We also find this sample has a quantum yield approaching 1 and it is nearly white phosphor because of blue STE and red Eu^{3+} ^5D_J. We have calculated the chromaticity coordinates of the color of the light sources x and y. We got x = 0.37 and y = 0.28. These coordinates stand for white light in the CIE Chromaticity diagram.

Results of this study, however, do demonstrate that the sensitization with the STE is a very effective means of coupling energy into Gd^{3+}.

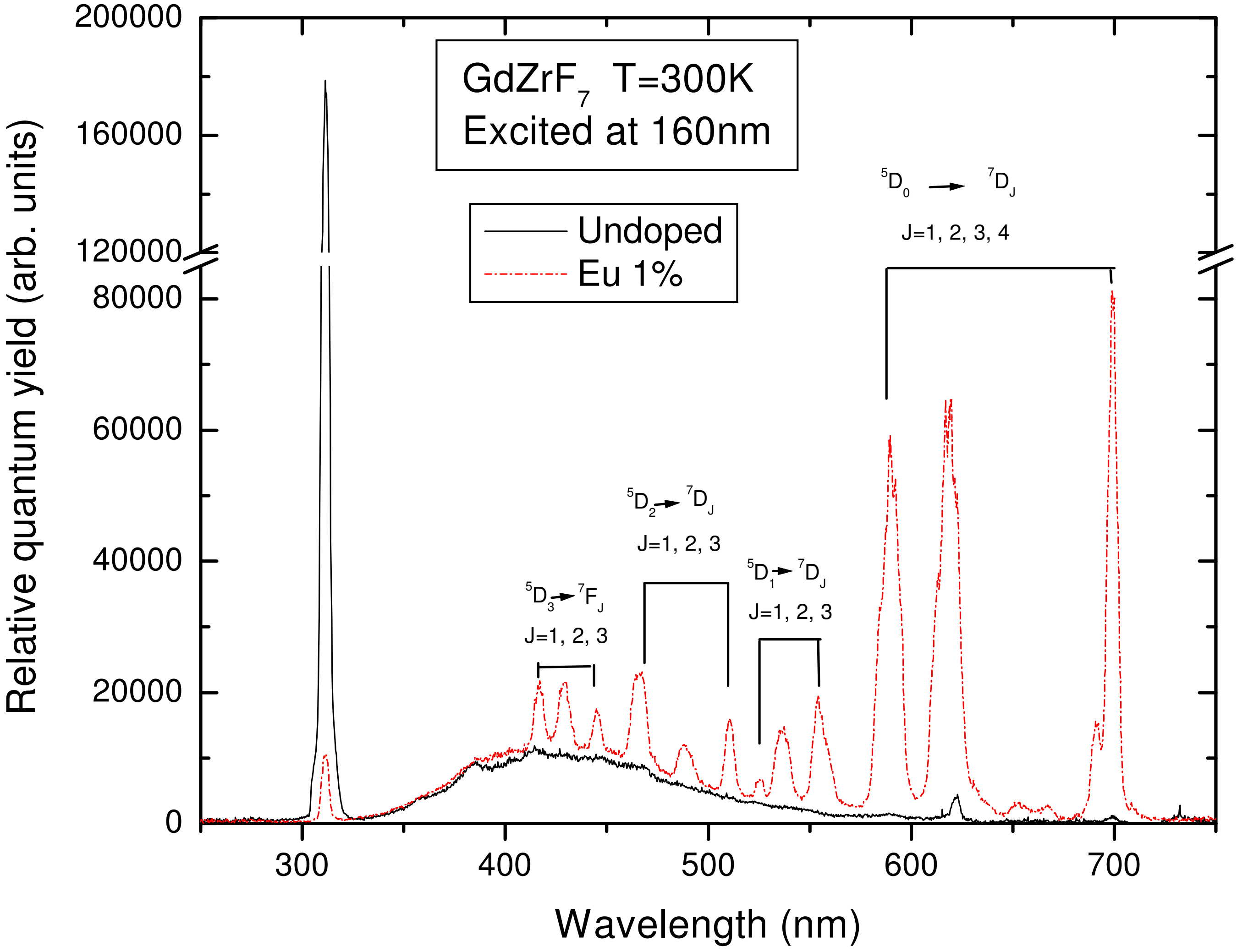

Fig. 7.1 Emission Spectra of Undoped and 1% Eu^{3+}-doped $GdZrF_7$

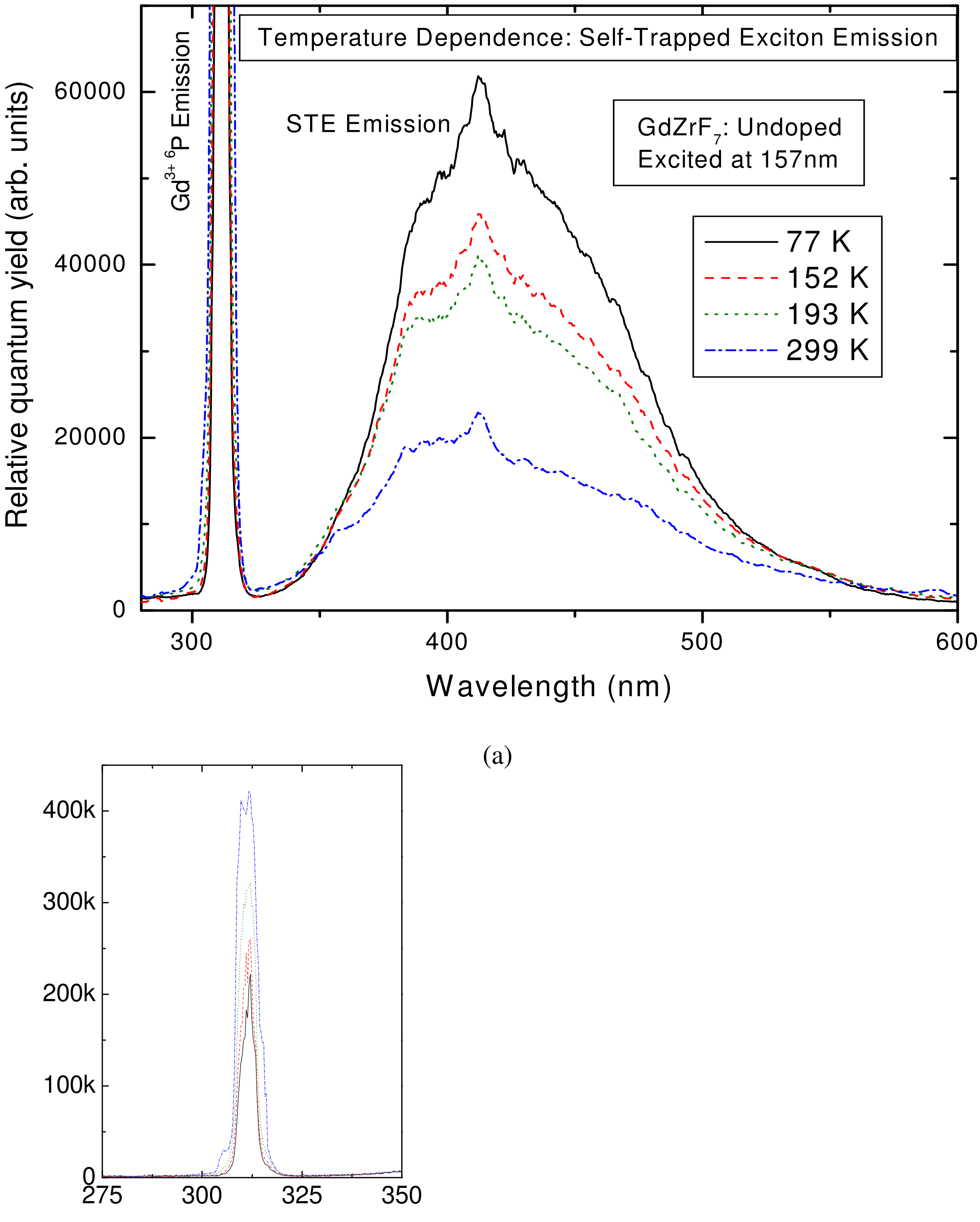

(a)

(b)

Fig. 7.2 Temperature dependence of (a) self-trapped emission spectrum of undoped GdZrF$_7$ and (b) ^{6}P emission of Gd^{3+}

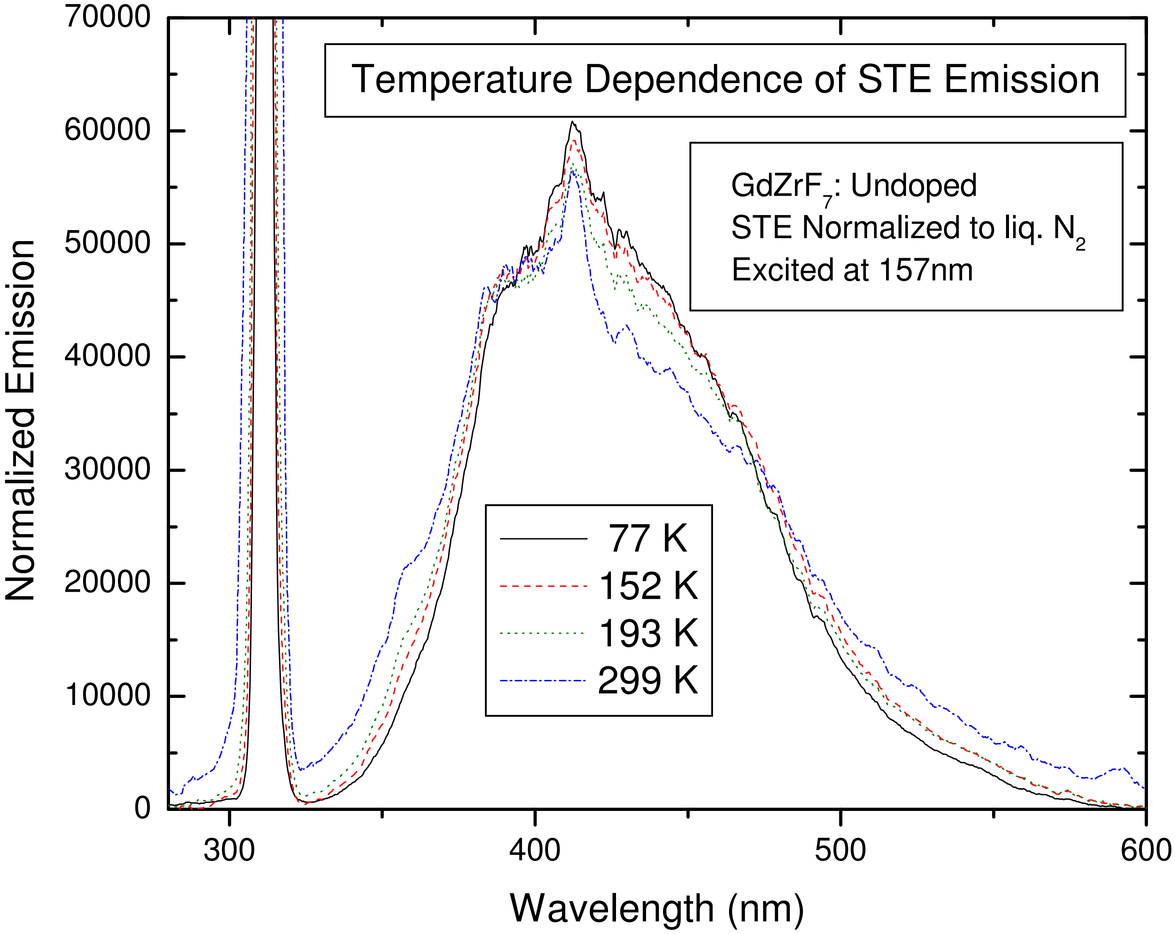

Fig. 7.3 Normalized STE emission spectrum of undoped $GdZrF_7$

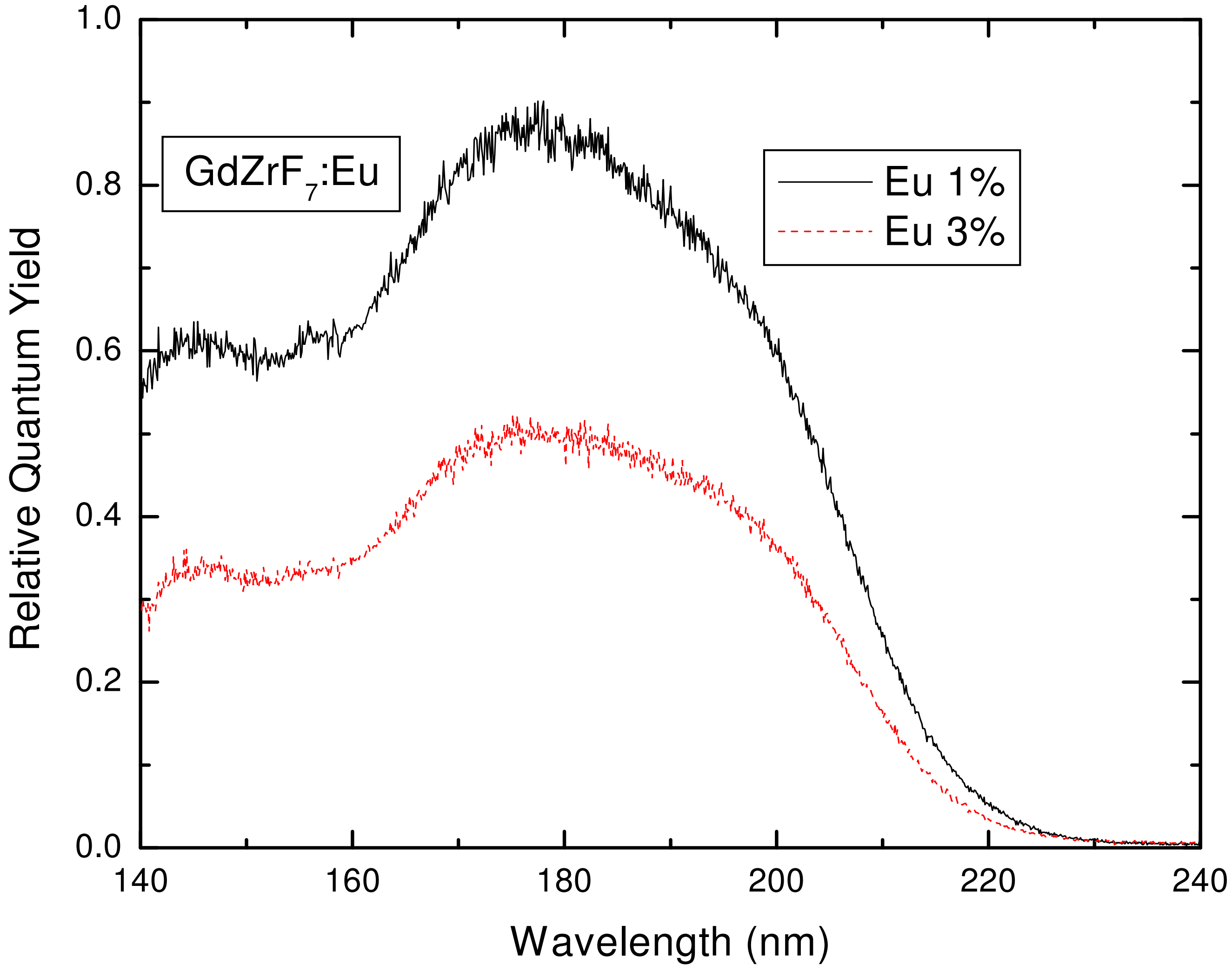

Fig. 7.4 Excitation Spectra of Eu-doped $GdZrF_7$

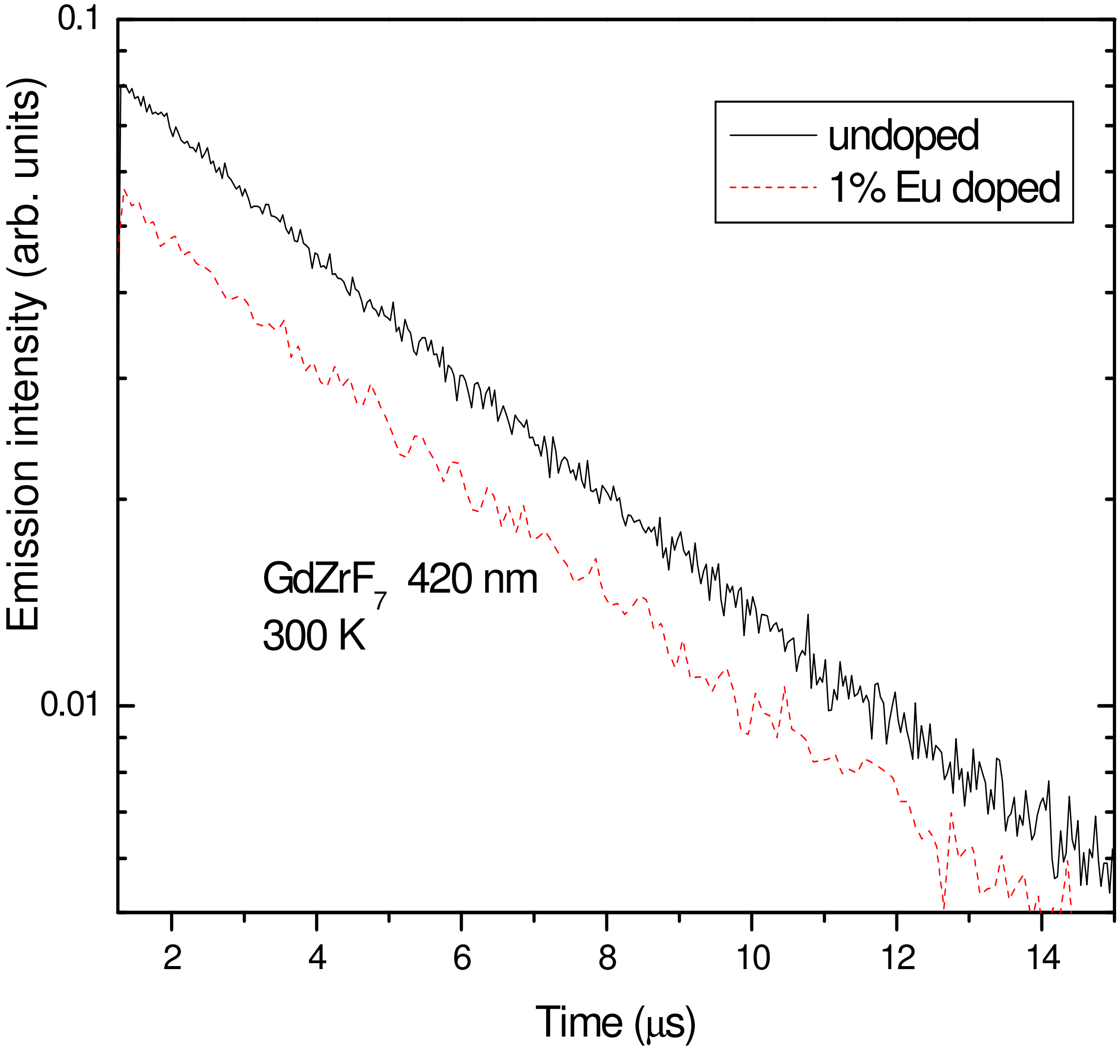

Fig. 7.5 Time dependence of the emission of undoped and Eu-doped $GdZrF_7$.

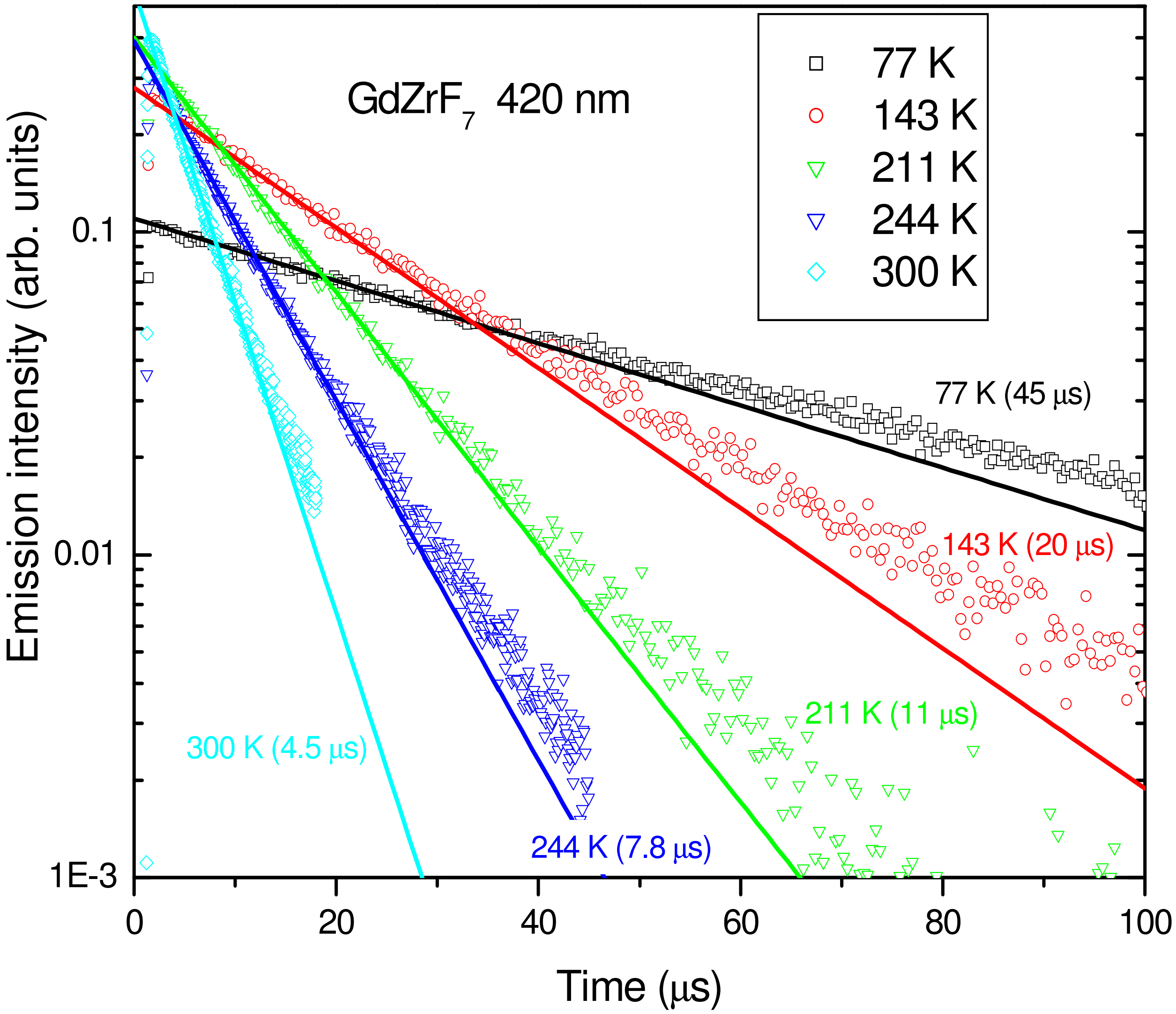

Fig. 7.6 Time dependence of the STE emission of undoped GdZrF$_7$ as a function of temperature.

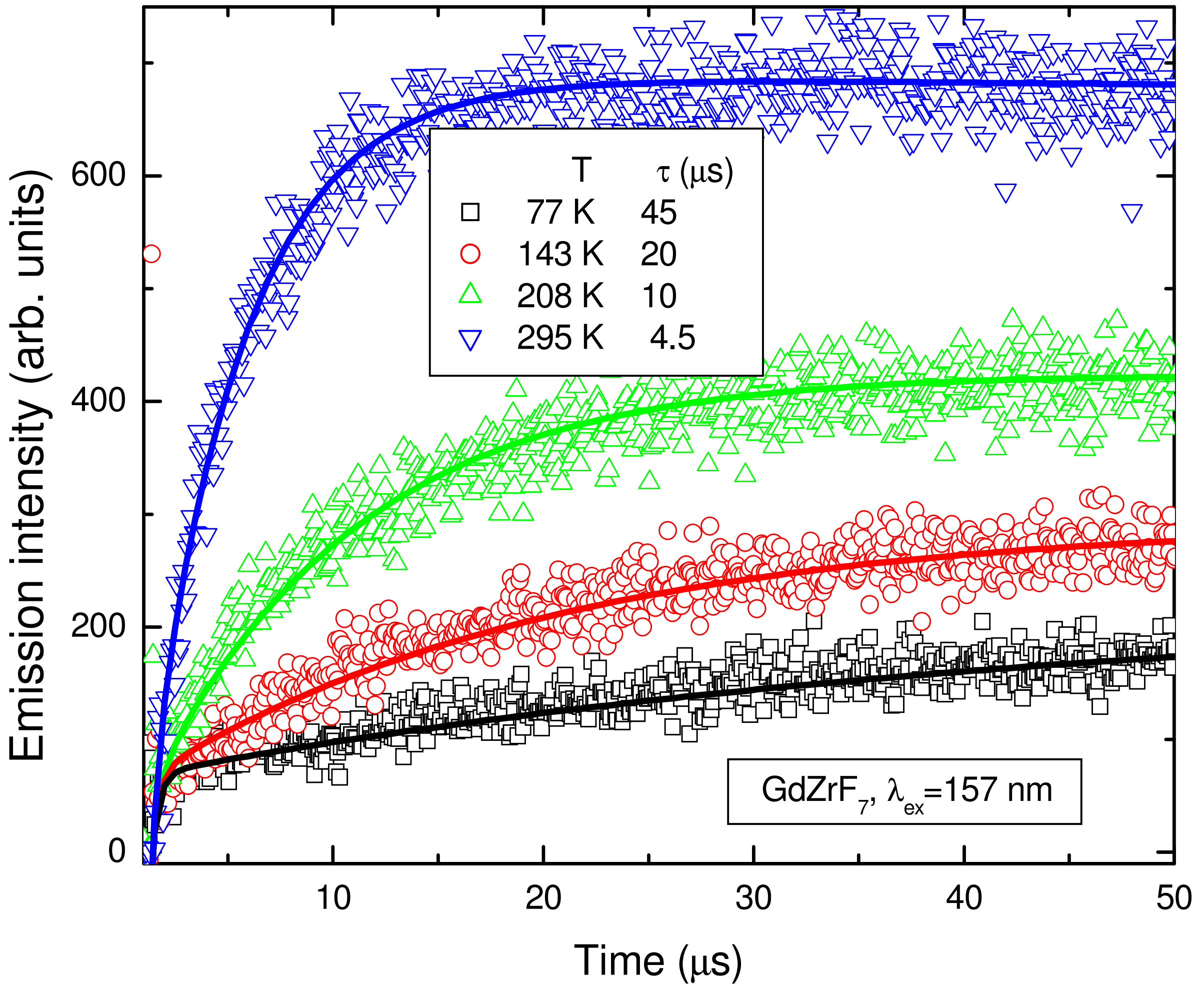

Fig. 7.7 Time dependence of the ^{6}P Gd^{3+} emission of undoped GdZrF$_7$ as a function of temperature.

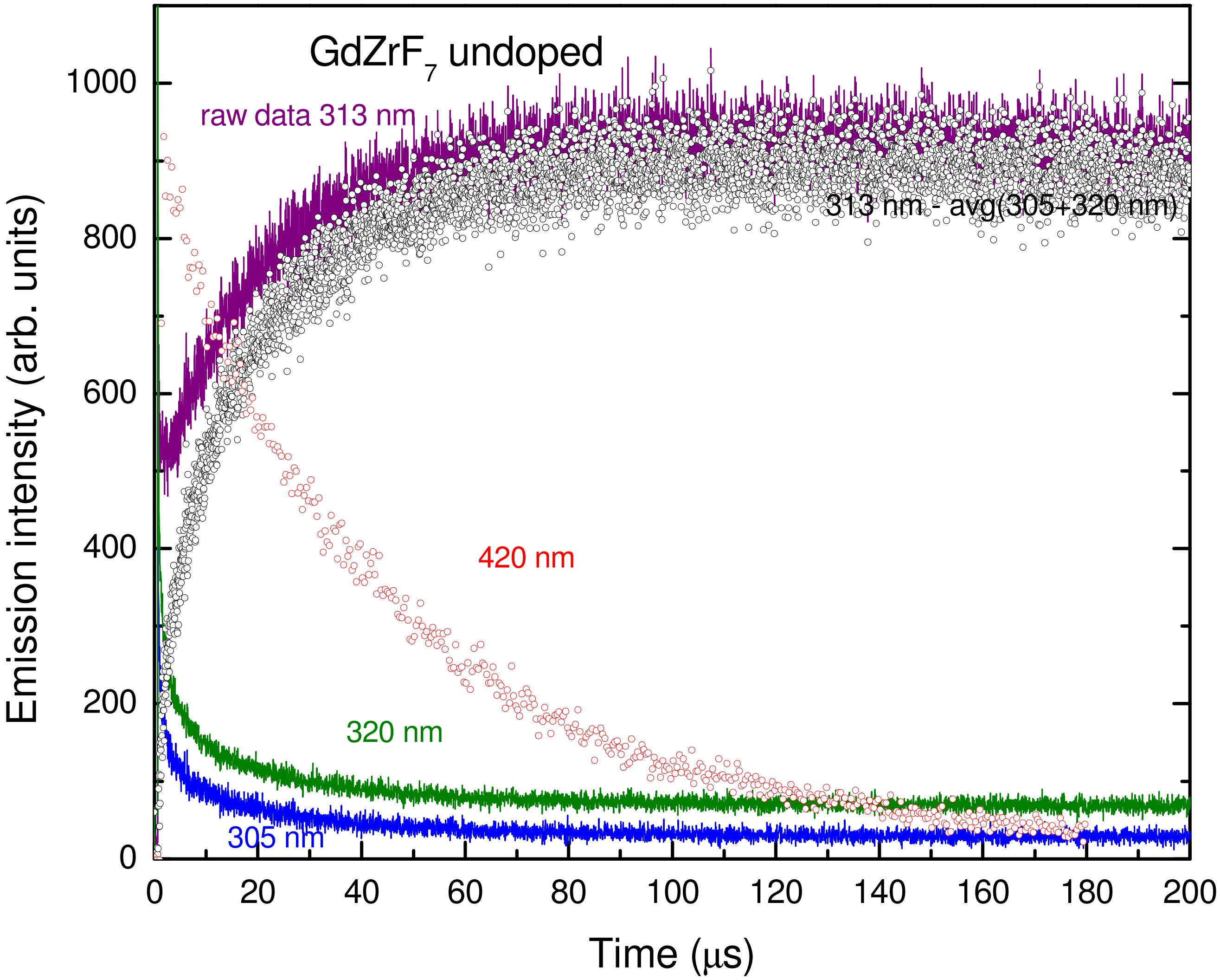

Fig. 7.8 Time dependence Gd^{3+} ^{6}P emission of undoped GdZrF$_7$ at liquid nitrogen temperature

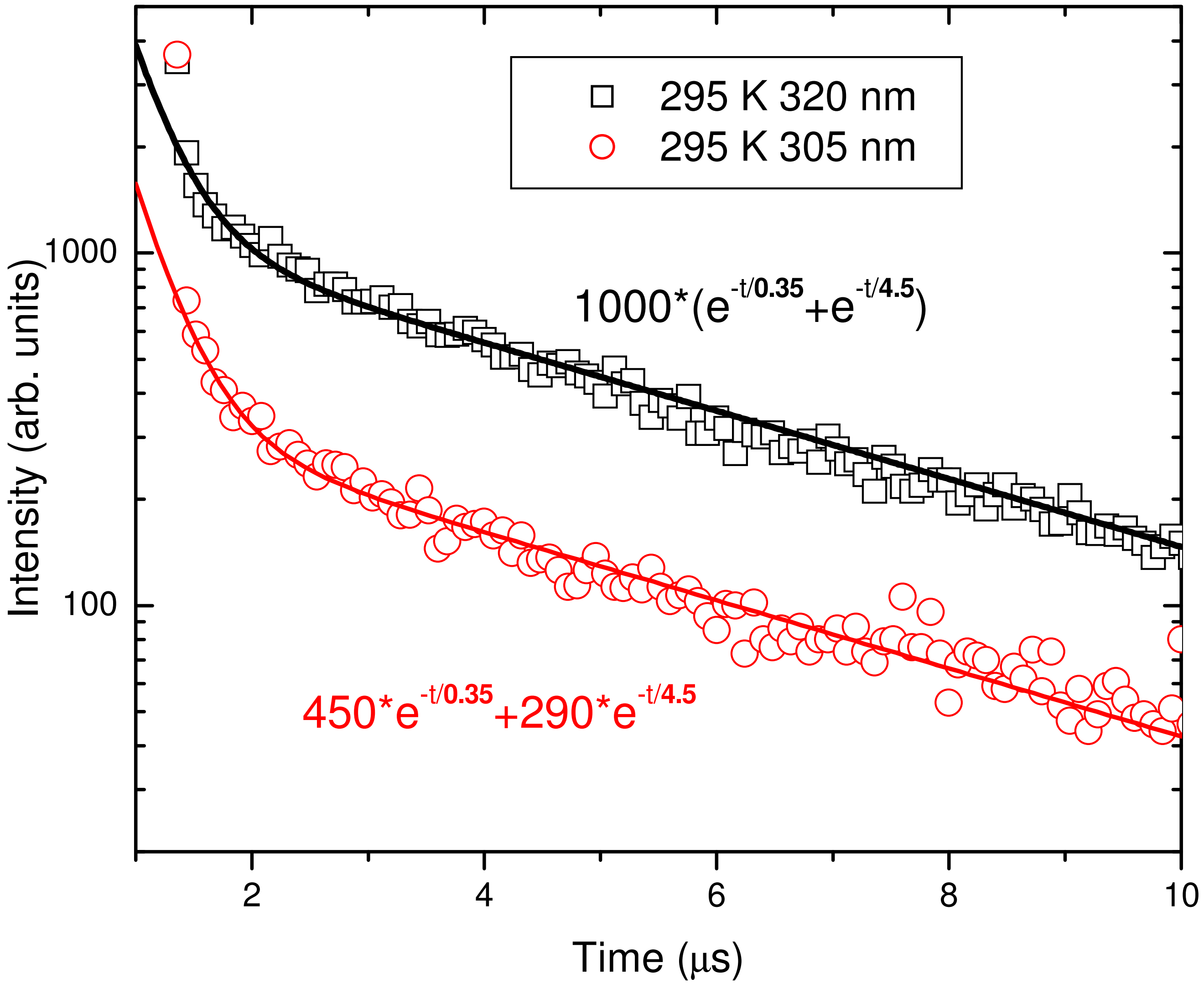

Fig. 7.9 Study of two components of the Broad Background

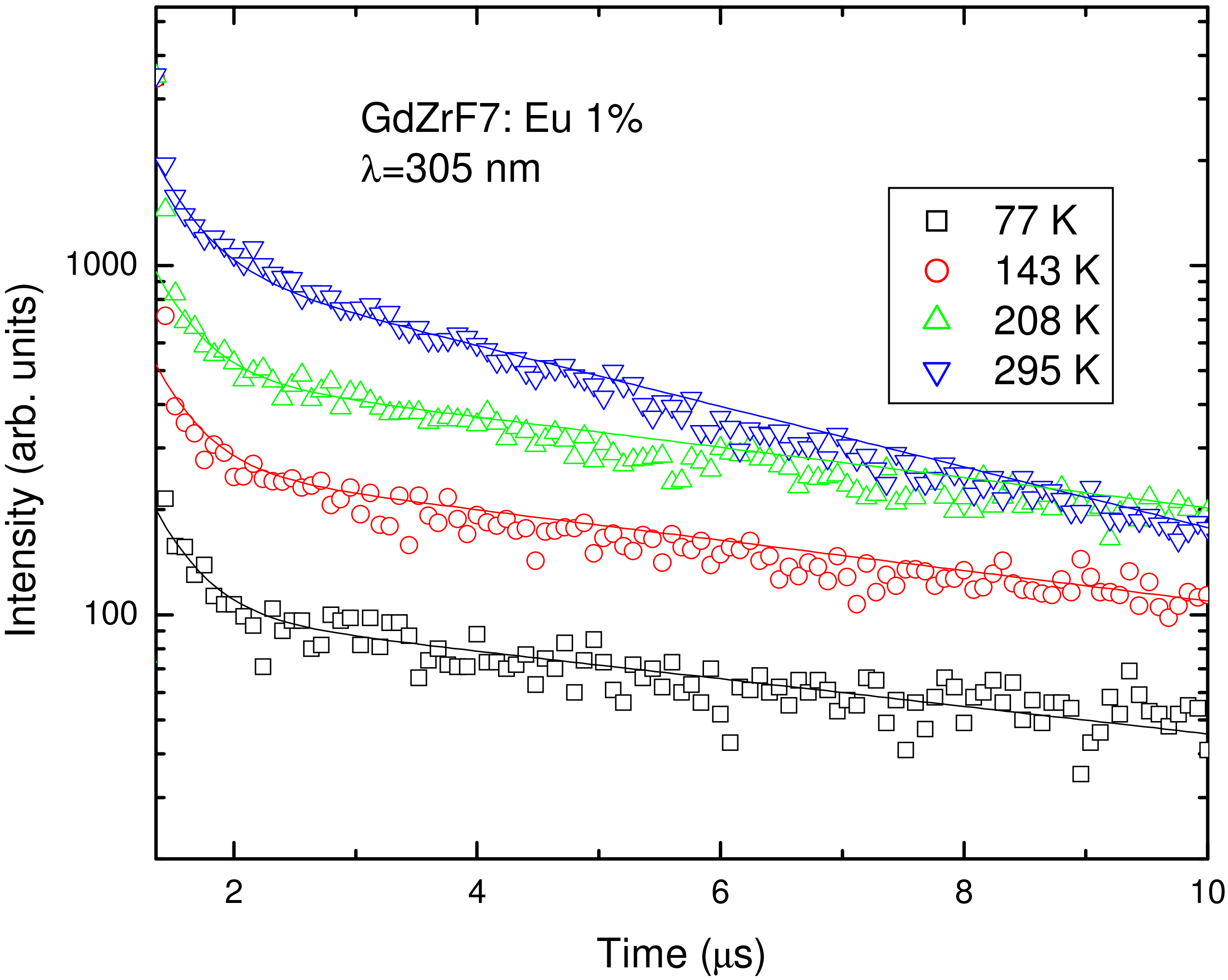

Fig. 7.10 The fast component of the Broad Background is independent of temperature.

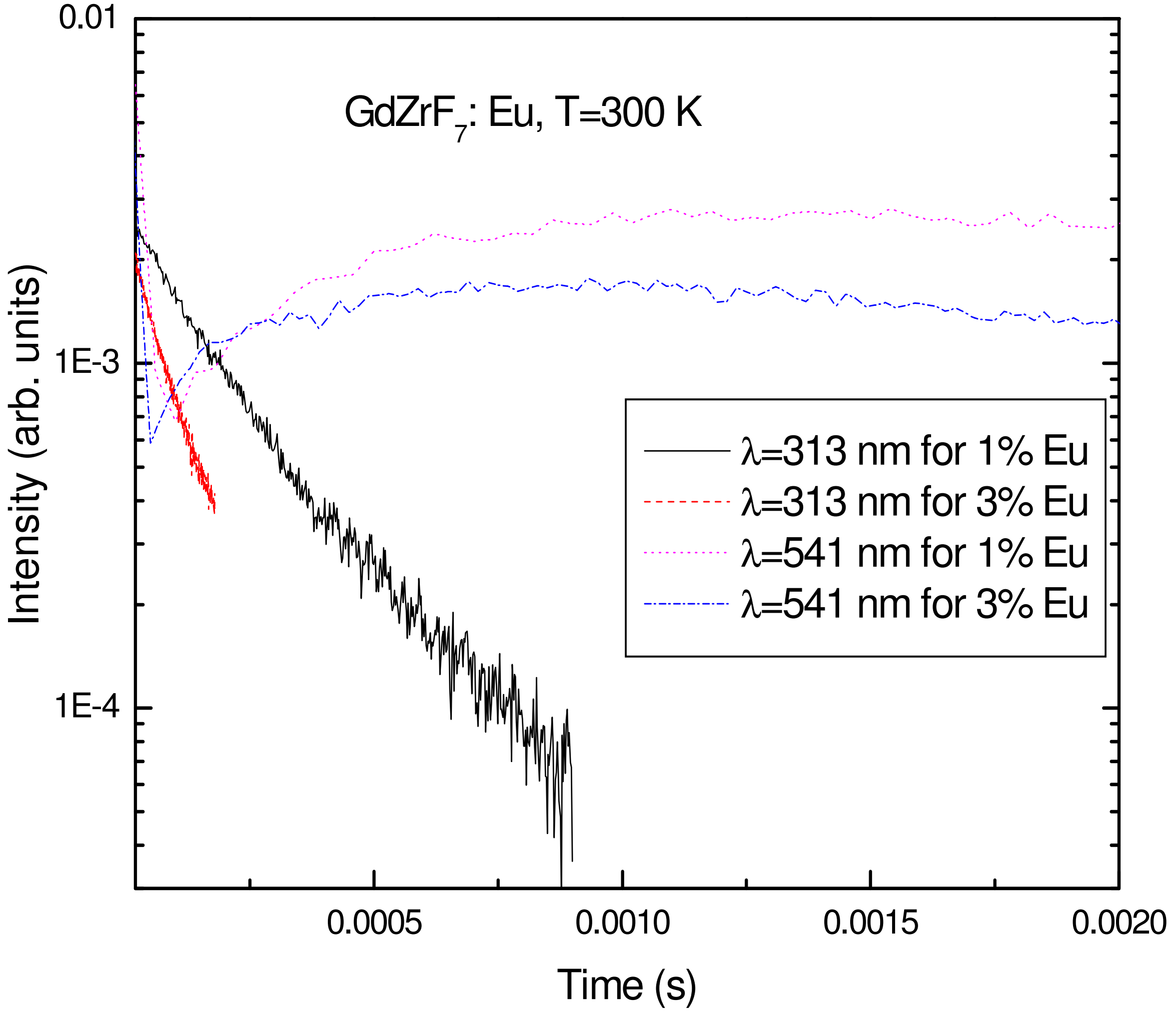

Fig. 7.11 Gd^{3+}→Eu^{3+} energy transfer rate increases in proportion to the Eu^{3+} concentration.

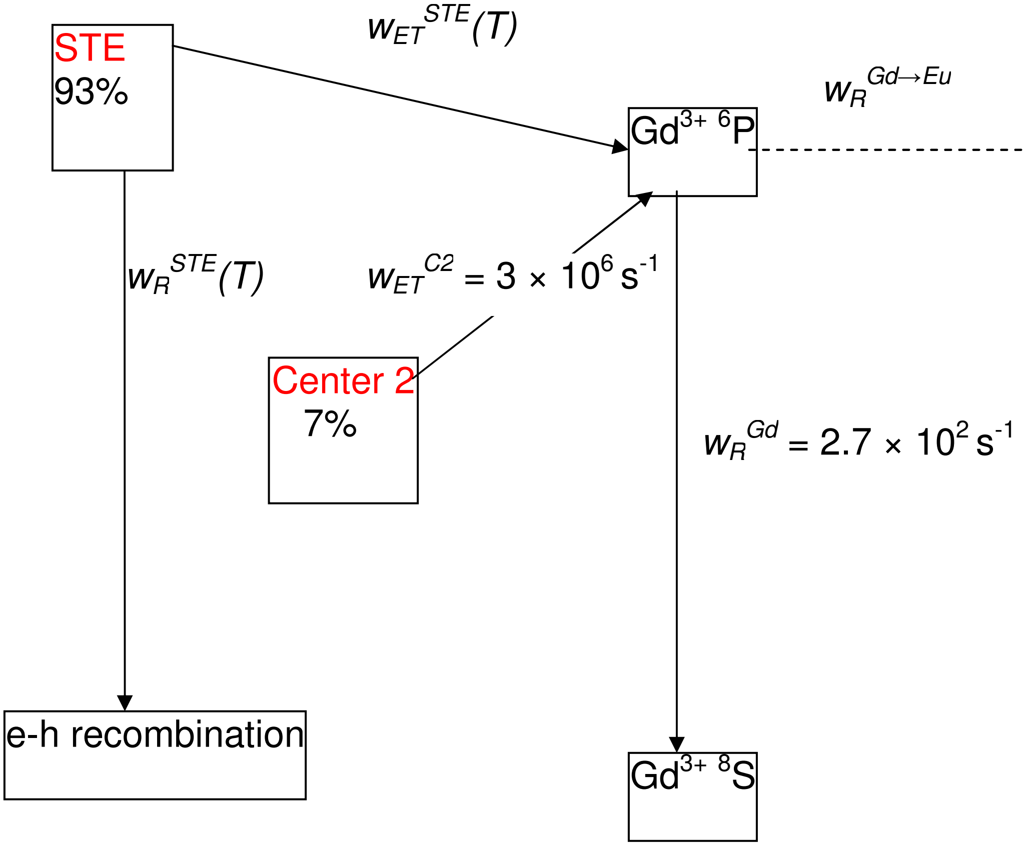

Fig. 7.12 Model for the Dynamics of the Populations

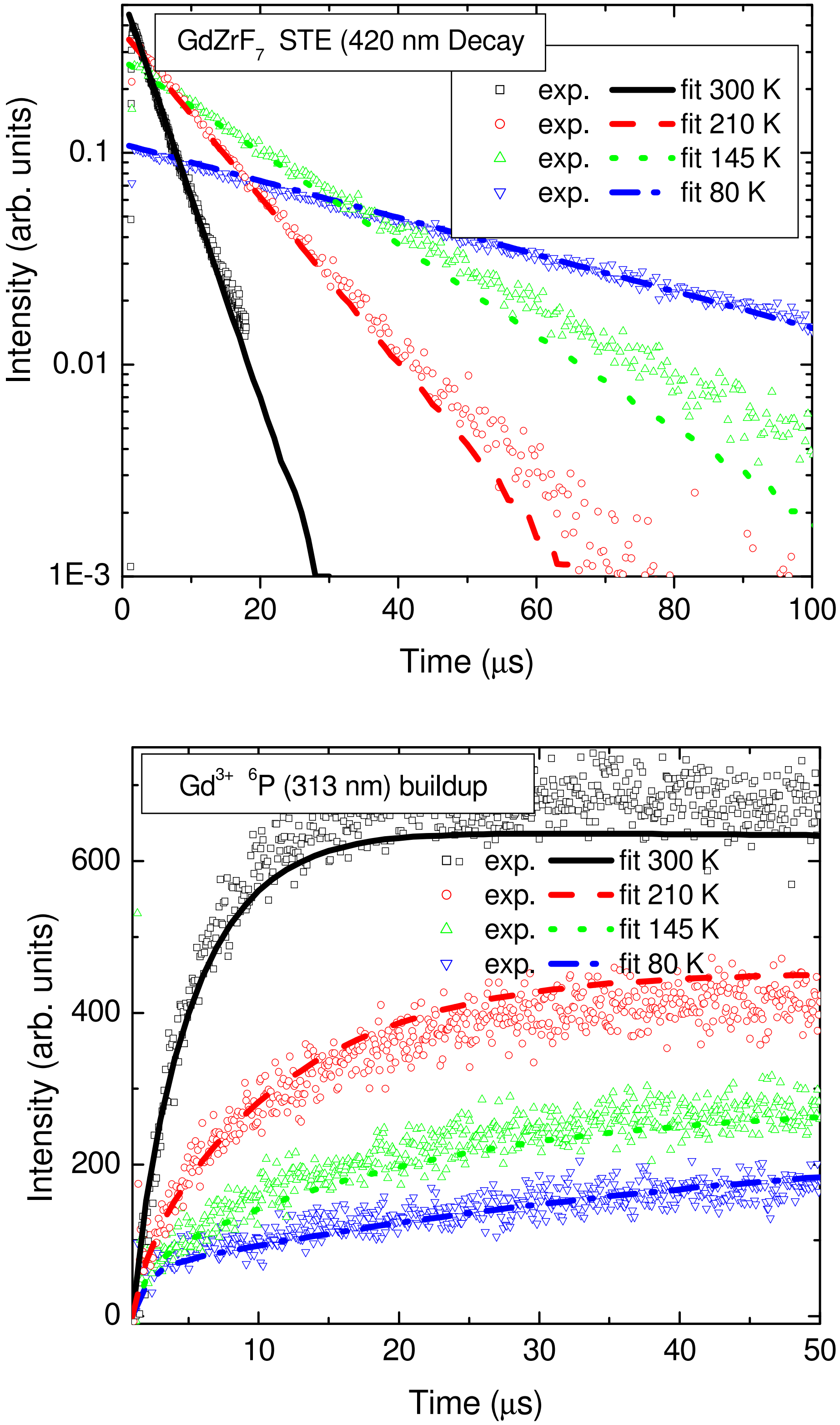

Fig. 7.13 Fit to time dependence and relative Intensities with all parameters fixed except W_R^{STE} and W_{ET}^{STE}

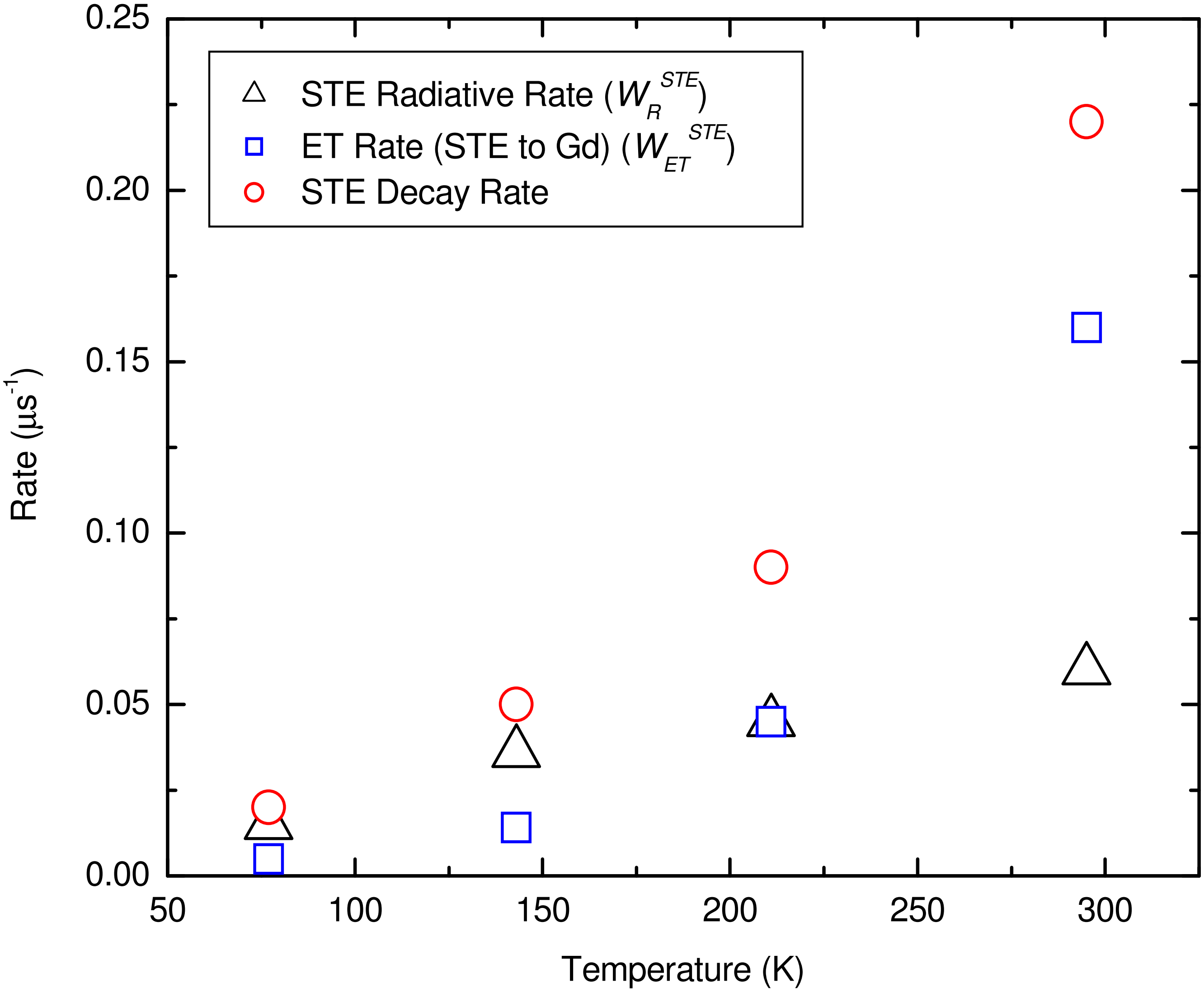

Fig. 7.14 Temperature Dependence of the Best-fit Rates

CHAPTER 8

CONCLUSIONS

In this dissertation, we studied several methods of sensitizing Gd^{3+} for obtaining quantum cutting and for developing a VUV excited white phosphor. In order to sensitize Gd^{3+}, we used the $5d \rightarrow 4f$ transition of Pr^{3+} and Nd^{3+} as well as hosts whose STE of acts as donor to transfer energy to Gd^{3+} for the application of PCE.

When we used the $5d \rightarrow 4f$ transition of Pr^{3+}, Pr^{3+} rapidly and effectively sensitizes Gd^{3+} in GdF_3: Pr, Eu. Theoretically, when the ^6G level of Gd^{3+} is excited, efficient quantum cutting should occur. However, the $5d \rightarrow 4f$ emission of Pr^{3+} does not match the absorption of Gd^{3+} from ground state to ^6G states well. So the energy transfer predominantly feeds ^6I rather than ^6G of Gd^{3+}. This severely limits the possibility of quantum cutting. As a result, GdF_3: Pr, Eu is not a good quantum cutting phosphor. It is still necessary to find a host for Pr^{3+} such that its $5d \rightarrow 4f$ emission is sufficiently high in energy so as to provide a good match to the absorption of Gd^{3+} from ground state to the ^6G states well.

We also used the $5d \rightarrow 4f$ transition of Nd^{3+} to sensitize Gd^{3+}. A VUV photon is absorbed by the Nd^{3+} ions whereupon the energy is rapidly transferred to the high-lying excited states of the $4f^7$ configuration of Gd^{3+} in a time scale of nanoseconds. Unfortunately, a very efficient quantum cutting occurs for the Gd^{3+}-Nd^{3+} system in $GdLiF_4$: Nd 2% that produces infrared photons. An analysis of the dynamics and the theoretical limits of the dipole-dipole contributions, leads to the conclusions that (1) there is rapid donor-donor energy migration among the Gd^{3+} ions and (2) that exchange plays the dominant role in the cross relaxation energy transfer responsible for the quantum cutting. However, this material will not be a commercially viable quantum cutting phosphor since the photons are in the infrared and because of the large energy loss even if two photons were produced per input photon. Nonetheless it does provide important insights into the dynamics and mechanisms of the quantum cutting process.

We conclude from the studies of these two materials, that the 5d→4f transition of a trivalent rare earth ion is an effective method to sensitize Gd^{3+}. It is still necessary to find a system in which the energy gets to the ^6G states of Gd^{3+} such that quantum cutting with a co-doping of Eu^{3+} or some other lanthanide can be utilized for quantum cutting.

Sensitization of the ^6G states of Gd^{3+} by energy transfer from the self-trapped exciton (STE) has been demonstrated in Gd^{3+}-doped $ScPO_4$. But the efficiency of energy transfer to the ^6G states which is only about 30% limits the usefulness of this material as a quantum cutting phosphor. At room temperature the energy transfer to Gd^{3+} ions is highly efficient competing effectively with both radiative decay of the STE and energy transfer to killer centers.

To use STE sensitization of the ^6G states of Gd^{3+} for quantum cutting, it will be necessary to identify materials whose STE emission occurs at even shorter wavelengths than is the case for $ScPO_4$ so that a larger fraction of the energy transfer occurs to the ^6G states or even higher-lying states of Gd^{3+}. Results of this study, however, do demonstrate that the sensitization with the STE is a very effective means of obtaining good coupling of the VUV excitation to Gd^{3+}.

For Eu^{3+}-doped $GdZrF_7$, the STE emission occurs around 420 nm. Therefore the energy transfer can not occur to the ^6G states or even higher-lying states of Gd^{3+}. In this case, the STE→Gd^{3+} energy transfer occurs by dipole-dipole or exchange interactions due to the overlap of the high energy tail of the STE emission and Gd^{3+} ^6P absorption. Its rate increases strongly with temperature. Gd^{3+} transfers energy very effectively to Eu^{3+} and the rate is proportional to the Eu^{3+} acceptor concentration. We find Eu^{3+}-doped $GdZrF_7$ has a quantum yield approaching 1 and it is nearly white phosphor because of the combination of the blue STE emission and the predominantly red emission of Eu^{3+} from the $^5D_0$ state. Additional Eu^{3+} emission from the higher ^5D_J (J>0) states also contribute at shorter visible wavelengths helping to generate a nearly white output.

We have demonstrated that the 5d→4f transition of trivalent rare earth ions and the self-trapped exciton (STE) are capable of effectively sensitizing Gd^{3+}. We still need to find a trivalent rare earth ion whose 5d→4f transition is capable of transfering energy predominantly to the ^6G states of Gd^{3+} in order to successfully take advantage of the proven Gd^{3+}-Eu^{3+} quantum cutting couple for developing a VUV-excited phosphor whose quantum yield approaches a value of 2. If one can find a material whose STE emission occurs at even shorter wavelengths than the STE of $ScPO_4$ it may also be possible to use the STE to sensitize Gd^{3+} for a quantum cutting phosphor. Development of such phosphors would offer the prospect for great benefits to society by providing the scientific basis for realization of a new, highly efficient and environmentally benign lighting technology.

REFERENCES

[1] C. R. Ronda. J., Alloys Compounds 225, 534 (1995).

[2] A. M. srivastava and C. R. Ronda, the Electrochemical Society ***Interface*** Summer, 48 (2003).

[3] R.T. Wegh, H. Donker, K.D. Oskam, A Meijerink, J. Lumin. 82, 93 (1999).

[4] D. L. Dexter, Phys. Rev. 108 (3), 630 (1957).

[5] T. Justel, H. Nikol, and C. R. Ronda, *Angew. Chem. Int. Ed.,* 37, 3084 (1998).

[6] J. A. Caird, A. J. Ramponi and P. R. Staver, J. Opt. Soc. Am. B 8, 1391 (1991).

[7] Th. Förster, Ann. Physik 2, 55 (1948)

[8] D. L. Dexter, J. Chem. Phys. 21, 836 (1953)

[9] S. H. Lin, W. Z. Xiao and W. Dietz, Phys. Rev. E 47, 3698–3706 (1993).

[10] B. C. Carlson and G. S. Rushbrooker: Proc. Cambridge Phil. Soc. 46 (1950) 625

[11] T. Kushida, J. Phys. Soc. Japan, 34, 1318 (1973).

[12] R. T. Wegh, A Meijerink, Acta Phys. Polon. A 90, 333 (1996).

[13] Bernard Moine , Gregory Bizarri, Bernard Varrel, Jean-Yves Rivoire, Optical Materials 29 (2007) 1148 – 1152

[14] R. T. Wegh, H. Donker, K. D. Oskam and A. Meijerink, Science **283**, 663 (1999).

[15] B. Liu *et al.*, Journal of Luminescence **101**, 155 (2003).

[16] H. Kondo, T. Hirai, and S. Hashimoto, Journal of Luminescence **108**, 59 (2004).

[17] N. Kodama and Y. Watanabe, Applied Physics Letters **84**, 4141 (2004).

[18] P. Dorenbos, J. Lumin. 91 (2000) 155.

[19] C. Feldmann, T. Justel, C. R. Ronda, and D. U. Wiechert, J. Lumin. **92**, 245 (2001).

[20] P.S. Peijzel, W.J.M. Schrama, A. Meijerink, Mol. Phys. S 102 (2004) 1285.

[21] P.W. Dooley, J. Thogersen, J.D. Gill, H.K. Haugen, R.L. Brooks, Opt. Commun. 183 (2000) 451.

[22] R. T. Wegh, H. Donker, A. Meijerink, R. J. Lamminmaki, and J. Holsa, Phys. Rev. B **56**, 13841 (1997).

[23] C. Gorller-Walrand, L. Fluyt, P. Porcher, A. A. S. Da Gama, G. F. de Sa, W. T. Carnall, and G. L. Goodman, J. Less-Common Met.

[24] A. L. Harmer, A. Linz, and D. R. Gabbe, J. Phys. Chem. Solids **30**, 1483 (1969).

[25] J. R. Ryan and R. Beach, J. Opt. Soc. Am. B **9**, 1883 (1992).

[26] X. X. Zhang, A. B. Villaverde, M. Bass, B. H. T. Chai, H. Weidner, R. I. Ramotar, and R. E. Peale, J. Appl. Phys. **74**, 790 (1993).

[27] A.F.H. Librantz, L. Gomes, L.V. G Tarelho, I.M. Ranieri, J. Appl. Phys. 95 (2004) 1681.

[28] O. Guillot-Noel, B. Bellamy, B. Viana, and D. Gourier, Phys. Rev. B **60**, 1668 (1999).

[29] R. L. Cone and R. S. Meltzer, Phys. Rev. Lett. **30**, 859 (1973) and R. L. Cone and R. S. Meltzer, J. Chem. Phys. **62**, 3573 (1975).

[30] R. T. Wegh, H. Donker, A. Meijerink, R. J. Lamminmaki, and J. Holsa, Phys. Rev. B **56**, 13841 (1997).

[31] Z. Yang, H. H. Lin, M. Z. Su, Y. Tao, and W. Wang, J. Alloys Compd. **308**, 94 (2000).

[32] S. P. Feofilov, Y. Zhou, H. J. Seo, J. Y. Jeong, D. A. Keszler, and R. S. Meltzer, Phys. Rev. B **74**, 085101 (2006).

[33] R. T. Wegh, E. V. D. van Loef, and A. Meijerink, J. Lumin. **90**, 111 (2000).

[34] W. Jia, Y. Zhou, S. P. Feofilov, R. S. Meltzer, J. Y. Jeong, and D. Keszler, Phys. Rev. B **72**, 075114 (2005).

[35] Ken-ichi Noba and Yosuke Kayanuma, J. Phys. Soc. Jpn. **67** (1998) pp. 3388-3391

[36] V. Ivanova , M. Kirm, V. Pustovarov, A. Kruzhalov, Radiation Measurements 42 (2007) 742 – 745

[37] S.P. Feofilov, Y. Zhou, J.Y. Jeong, D.A. Keszler, R.S. Meltzer, Journal of Luminescence 125 (2007) 80 – 84

[38] Jinyong Kuang, Yingliang Liu, Chemical Physics Letters 424 (2006) 58 – 62

[39] B. R. Namozov, V. A. Vetrov, S. M. Muradov, and R. I. Zakharchenya, Physics of Solid State, Vol. 44 No. 8. 2002

[40] R. T. Williams and K. S. Song, J. Phys. Chem. Solids **51**, 679 (1990) and references therein.

[41] M. Itoh and T. Sakurai, Phys. Status Solidi B **242**, R52 (2005)

[42] G. Bizarri and P. Dorenbos, Phys. Rev. B **75**, 184302 (2007)

[43] Michel Poulain, Marcel Poulain et Jacques Lucas, Mat. Res. Bull. 7, 319-326 (1972)

[44] E. Van der Kolk, P.Dorenbos, C.W.E. van Eijk, Optics Communications. 197, 317-326. (2001)

APPENDIX

1. Calibration of the PMT

We used a series of interference filters and the FEL Standard Lamp to calibrate the spectral response of the PMT. The intensity of emission is defined as

$$S = \lambda Q(\lambda)\int T(\lambda)I(\lambda)d\lambda$$

Here $Q(\lambda)$ is the quantum response of the PMT. $T(\lambda)$ is the transmission of the filter and $I(\lambda)$ is the output of the lamp. We put these filters before the lamp and measured the emission with the PMT. So we got

$$S_1 = \lambda_1 Q(\lambda_1)\int T_1(\lambda)I(\lambda)d\lambda$$

$$S_2 = \lambda_2 Q(\lambda_2)\int T_2(\lambda)I(\lambda)d\lambda$$

The spectral response is expressed as

$$P(\lambda) = \frac{Q(\lambda_2)}{Q(\lambda_1)} = \frac{\lambda_1}{\lambda_2}\frac{S_2}{S_1}\frac{\int T_1(\lambda)I(\lambda)d\lambda}{\int T_2(\lambda)I(\lambda)d\lambda}$$

2. Correction of the excitation spectrum

(1) Correcting of the effect of scattered and background radiation

The Oriel 77341 PMT tube is sensitive to light in the spectral range 180 to 870nm. Considering that UV beam is reflected from the window covering the sample, we should use optical filters to keep the light from going into the PMT. However, some optical filters emit in the visible under UV excitation. Its emission level will remain the same under identical experimental conditions, while the emission intensity of samples themselves may vary from sample to sample. Therefore the interference of the filter emission can be recognized. To reduce the interference from the optics, smaller or larger incident angles other than 45° of the VUV beam to the sample surface can be used. As a result, the reflected VUV beam from the sample surface will not directly hit the optics so that the emission level from the optics will be reduced.

Background light comes from the monochromator which filters the excitation source. The intensity slightly depends on wavelength, that is, the position of the grating. It is light at wavelengths other than that of the setting of the monochromator. This results from stray light that is scattered from non-smooth mirrors and zeroth or higher order diffractions of the grating. It is difficult to remove the background light since the traveling direction of the background light is similar to the pumping light. It can be reduced by using smaller or larger incident angles than 45^o of the pump beam in order to reduce the background interference.

(2) Correcting for the presence of multiple emission wavelengths where the quantum efficiency of the PMT has different values

We used the correction factor weighted average of $P(\lambda)T(\lambda)$ weighted by the emission spectrum of the sample and of the sodium salicylate.

$$C_{sample} = \frac{\int E_{sample}(\lambda)d\lambda}{\int E_{ref}(\lambda)d\lambda} \frac{\int E_{ref}(\lambda)T(\lambda)P(\lambda)d\lambda}{\int E_{sample}(\lambda)T(\lambda)P(\lambda)d\lambda}$$

Here $E(\lambda)$ is the emission spectrum obtained by the CCD.

(3) For the consequence of the emission spectrum changing as a function of excitation wavelength, we assume the emission spectrum is independent of the excitation wavelength.